Experimental Study of Single Phase Turbulent Pipe Flow with Variable Obstructions.

Experimental Study of Single Phase Turbulent Pipe Flow with Variable Obstructions.

By

Edilson Nogueira Jacinto, B. Sc.

A Thesis
Submitted to the Department of Engineering Physics and the School of Graduate Studies in partial fulfillment of the requirements for the degree of Master of Applied Science

McMaster University

MASTER OF APPLIED SCIENCE (2014)
MCMASTER UNIVERSITY
PHYSICS ENGINEERING
HAMILTON, ONTARIO

TITLE: Experimental Study of Single Phase Turbulent Pipe Flow with Variable Obstructions.

AUTHOR: Edilson Nogueira Jacinto

SUPERVISOR: David Novog

Number of Pages: xv, 112

Abstract

A considerable amount of effort is expended to better characterize and avoid the critical heat flux (CHF) phenomena in nuclear reactor systems. Most fuel assemblies used in power reactors possess small structures to maintain them in place as well as maintain the physical integrity of the assembly and element to element clearances. These structures act as local flow obstructions that modify the turbulent flow characteristics and in general improve the heat transfer. In CANDU reactors, a series of bearing pads are used to maintain clearances between the fuel and the pressure tube while spacer pads maintain element to element clearances. This thesis experimentally investigates the impact of bearing pads on the downstream flow and turbulence characteristics under room temperature and pressure conditions.

The test section is fabricated from a 30 cm long and 2.54 X 2.54 cm squared transparent cast acrylic piece. Machined through the center is a cylindrical flow channel with inner diameter of approximately 11 cm. CANDU fuel bundle bearing pad simulators have been designed and constructed at McMaster University to allow for the study of the local flow characteristics downstream of these obstructions. Measurements are taken with unobstructed flow and a variety of obstruction heights to examine the turbulence features generated. Each bearing pad is removable and is secured in place using high strength magnets. The test section connects to an existing room temperature fluid loop capable of delivering accurate flows up to a Reynolds number of 100000.

In order to validate the test section and measurement methods, a series of experiments were performed without obstructions. These measured velocity and turbulence data were compared to literature values to ensure similarity. After this validation study, experiments were carried out

using room temperature water as fluid at three different turbulent Reynolds numbers of 30700, 61400 and 99000 with and without obstructions, using Laser Doppler Velocimetry. Results in the streamwise direction were as expected, with velocity perturbations that in general decreased with increasing Reynolds number. Some evidence of local recirculation in the wake of the obstruction was also measured. In the azimuthal direction, velocity and turbulence measurements were largely isotropic downstream of the obstruction for low Reynolds numbers and small obstructions. At higher Reynolds number and/or larger obstructions, the components in the azimuthal direction were systematic and exhibited coherent like structures (i.e., rotating flow or swirl). Of particular importance was the decay of turbulence with downstream length which was significant in cases where no coherent structures were present. With coherent structures, the turbulence levels remained high for much further distances. The source of the structures at high Reynolds number is not clear as all physical geometries were verified to ensure no systematic biases were present.

Acknowledgments

The work for this thesis was carried out in a lab in the Nuclear Research Building at McMaster University. The author would like to express his gratitude towards his supervisor, Dr. David Novog of the Department of Engineering Physics, for his critical and constant support through the course of this experimental work. His gratitude goes to Clealand Berwick at the machine shop for his support in the manufacturing the test section and all cast acrylic components. His gratitude also goes to his colleagues Dr. Ken Leung, James Strack and Alexander Schneider for their support, constructive comments and suggestions to complete the experiments for this thesis, and to all his colleagues in the nuclear engineering department.

Mostly, he'd like to thank his family, his mother (Juliana Nogueira), father (Rosario Jacinto), siblings (Liures, Aziz, Eltizer, Paula, Emmanuel, Lisdalia, Clinton, Juliano and Carmen) for their consistent support and encouragement throughout this adventure.

Finally to his friends near and far, who make hard things easier and dull moments funnier: Jason, Salma, Shaun, Raul, Haekel, Quinzinho and Idalio.

Table of Contents

List of Tables

List of Figures

Nomenclature

Acronym

2D LDV	2 dimensional Laser Doppler Velocimetry
BWR	Boiling Water Reactor
CANDU	CANada Deuterium Uranium Reactor
CFD	Computational Fluid Dynamics
CHF	Critical Heat Flux
DNS	Direct Numerical Simulation
FFT	Fast Fourier Transform
IBM	Immersed Boundary Layer
LDV	Laser Doppler Velocimetry
MATIS-H	Measurement and Analysis of Turbulence In Sub-channels-Horizontal
obs	obstruction
PDO	Post-Dryout
PMD	Photo Detector Module
PMT	Photomultiplier Tube
PWR	Pressurized-Water Reactor
RMS	Root-Mean-Square
RSM	Reynolds Stress Model
RTD	Resistive Temperature Device
TR-PIV	Time Resolved Particle Image Velocimetry
URANS	Unsteady Reynolds Averaged Navier-Stokes

Roman

D	-	Diameter, [m]
D_b	-	Beam spacing, [mm]
d_e	-	Beam diameter at the focal waist, [mm]

D*e*	-	Beam diameter, [mm]
d_f	-	Fringe spacing, [μm]
d_m	-	X-dimension of the measurement volume, [mm]
f_D	-	Doppler frequency, [Hz]
H	-	Height, [m]
h_m	-	Z-dimension of the measurement volume, [mm]
L	-	Length, [m]
ℓ_m	-	Y-dimension of the measurement volume, [mm]
$\dot{m}$	-	Mass flow rate, [kg/s]
N	-	Number of samples
P	-	Pressure, [kpa]
R	-	Radius D/2, [m]
Re	-	Reynolds Number
S_o	-	Direct displacement, [mm]
T	-	Temperature, [°C]
T*u*	-	Turbulence intensity
U	-	Streamwise mean velocity, [m/s]
U_b	-	Bulk velocity, [m/s]
U_{rms}	-	Root-mean-squared velocity fluctuation at streamwise direction
u_z	-	Particle velocity, [m/s]
V	-	Azimuthal mean velocity, [m/s]
V_D	-	Measurement volume, [mm^3]
V_{rms}	-	Root-mean-squared velocity fluctuation at azimuthal direction
X	-	Apparent position of laser beam, [mm]
x, y, z	-	Coordinates
Y	-	Displacement of laser beam in y-direction, [mm]
Z	-	Displacement of laser beam in z-direction, [mm

Greek

Δ	-	Rate of change
θ	-	Incidence angle
κ	-	Beam half angle
λ	-	Wavelength, [nm]
μ	-	Dynamic viscosity, [kg/m/s]
μ_τ	-	Friction velocity, [m/s]
ν	-	Kinetic viscosity, [m^2/s]
ρ	-	Fluid density, [kg/m^3]
σ	-	Standard deviation

Subscripts

Ca	-	Cast acrylic

1. Introduction

A nuclear power plant is an advanced, complex and well balanced engineering facility. Each component of the facility is studied, designed and constructed to achieve maximum performance, safety and integration with the remaining components. In the short history of nuclear power, many types of reactors have been proposed for power production. They have different characteristics such as core design, cooling mechanism, fuel elements and assembly; but they all follow the same heat transfer philosophy: transport the heat generated in the fuel, to the fuel sheath surface, and then to the surrounding coolant by convection. The coolant carries the heat to the ultimate heat sink which is responsible for removing the thermal energy generated in the fuel.

Heat transfer is perhaps the most important characteristic of a nuclear reactor since overheating of the fuel is one safety concern that could lead to radioactive releases to the environment. Under normal operating conditions, the heat produced in the fuel is balanced by the heat removed to the coolant, maintaining stable sheath and fuel temperatures. Under accident conditions an imbalance between the heat produced and heat removed may occur causing the fuel temperatures to increase. An important safety goal established for most accidents is to guarantee that the fuel and fuel sheath remain intact and do not melt. Therefore the convective heat transfer coefficient has been investigated for decades within the nuclear industry at different conditions, power levels and geometries. An important phenomena during accidents which must be predicted is the Critical Heat Flux (CHF). When a fuel element reaches its CHF, convection heat transfer decreases by one or two orders of magnitude which in turn cause temperature excursions leading to potential damage to the sheath. CHF predictions are largely based on empirical correlations built into safety

analysis computer codes, and is highly influenced by local conditions, in particular local values of turbulence.

1.1 - Background and research motivation

In flows at low velocities the fluid inside the boundary layer proceeds along the flow lines and thus is considered laminar flow. In this region any possible generated local turbulence is damped by viscous forces such that the flow remains laminar. But with sufficient length or velocity where viscous damping cannot maintain laminar flow, the flow may transition to the turbulent regime, which is characterized by time-variance in direction and magnitude at any point. With turbulent flows, eddies of all scales form and in general the transport of heat from the surface is enhanced (Figure 1.1).

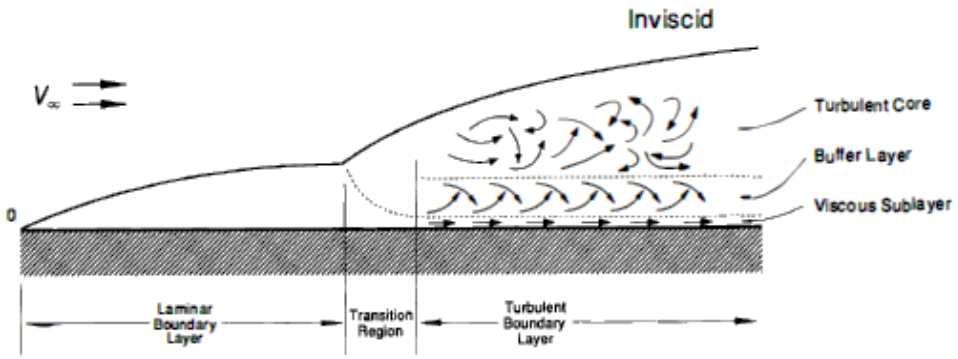

Figure 1.1 - Boundary layer velocity distribution [27]

Eddies substantially increase the transfer rate of energy laterally from the surface therefore turbulent flow is often preferred in most heat transfer equipment. Because of the inherent chaotic nature of turbulence, it is difficult to predict based on first principles and thus many approximate models or empirical formulations must be employed. For smooth cylindrical pipes, turbulence

occurs at Reynolds numbers on the order of 4000, although it may vary between 1000 and 10000 depending on the geometry.

$$Re = \frac{\rho \upsilon D}{\mu} \tag{1.1}$$

Turbulence production is a function of geometry, fluid properties-velocity and velocity gradients and varies non-linearly as a function of lateral distance from the wall. Turbulence generated in regions near the wall is advected downstream while in the lateral direction turbulence may be transported to regions where viscous dissipation reduces its magnitude i.e., in viscous sublayer). If an obstruction is introduced into pipe flow, the local velocity and velocity gradients near the obstruction increase generating additional turbulence, which is transported downstream. Thus in general the effect of obstructions on heat transfer persists downstream of the blockage and is affected by dissipation of the turbulence downstream.

Nuclear fuel assemblies or bundles are designed with features to maintain their physical integrity and intended placement within the reactor core. For *The Pressurized-Water Reactors* (PWR) the typical fuel assembly contains a square grid type spacer with spring clips. The spring clips of the spacer contact and support the sealed stainless steel or Zircaloy 4 m long fuel rods. Each fuel rod contains 2-5% enriched UO_2 made from black ceramic material with a high melting point of 2800^{o}C. The UO_2 is in the form of small cylindrical pellets, about 1 cm in diameters and 2 cm in length (Figure 1.2).

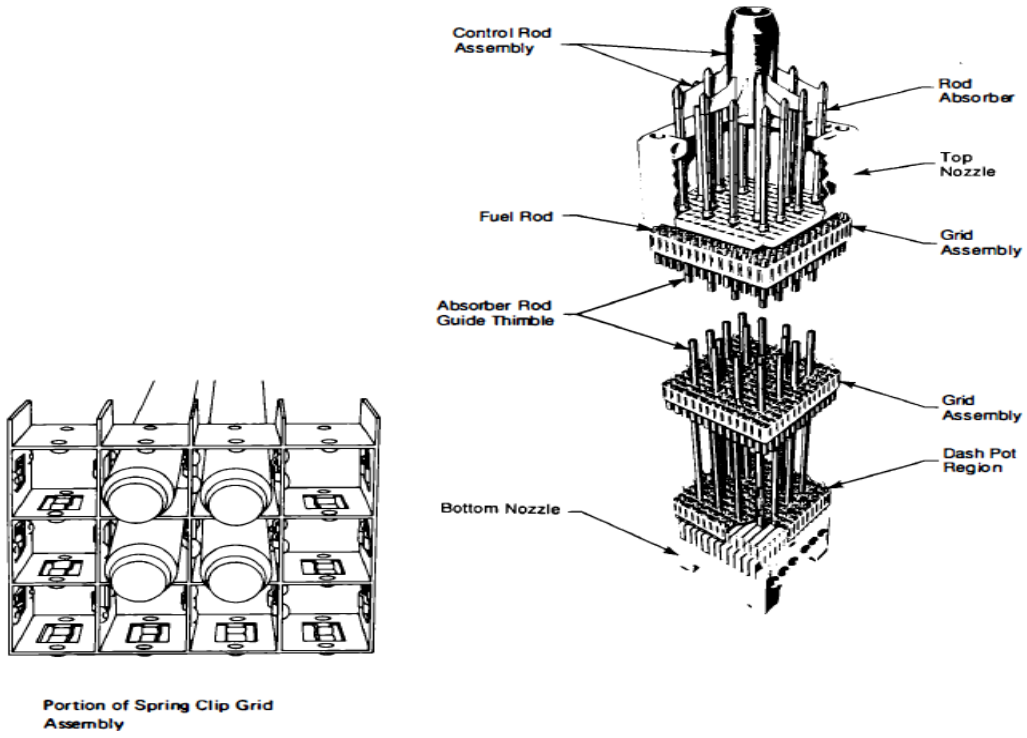

Figure 1.2 - Typical PWR fuel assembly [27]

For the *CAN*ada *D*euterium *U*ranium (CANDU) reactor, the fuel bundle is arranged in concentric rings, with an outer diameter of 10.2 cm and 49.5 cm long. Each of the concentric rings holds numerous cylindrical fuel elements. A total of 37 Zircaloy clad fuel elements with natural Uranium UO_2 pellets (1.22 cm in diameter and 1.64 cm in length) are used in each bundle. The bundle is equipped with circular Zircaloy plates at both ends that maintain structural integrity and element spacing. Interior to the bundle the elements are held by inter-element spacer and bearing pads located on the surface of the fuel sheaths to prevent direct contact of the fuel rods with the pressure tube walls and allow space for coolant flow through the bundles (Figure 1.). Each bearing pad or spacer represents a geometrical obstruction to the flow in the fuel bundle and generates higher local velocity gradients leading to higher turbulence levels. In addition the obstructions create pressure gradients laterally within the bundle which also helps to promote

mixing between sub-channel volumes. Both of these effects tend to enhance CHF relative to unobstructed flow pathways.

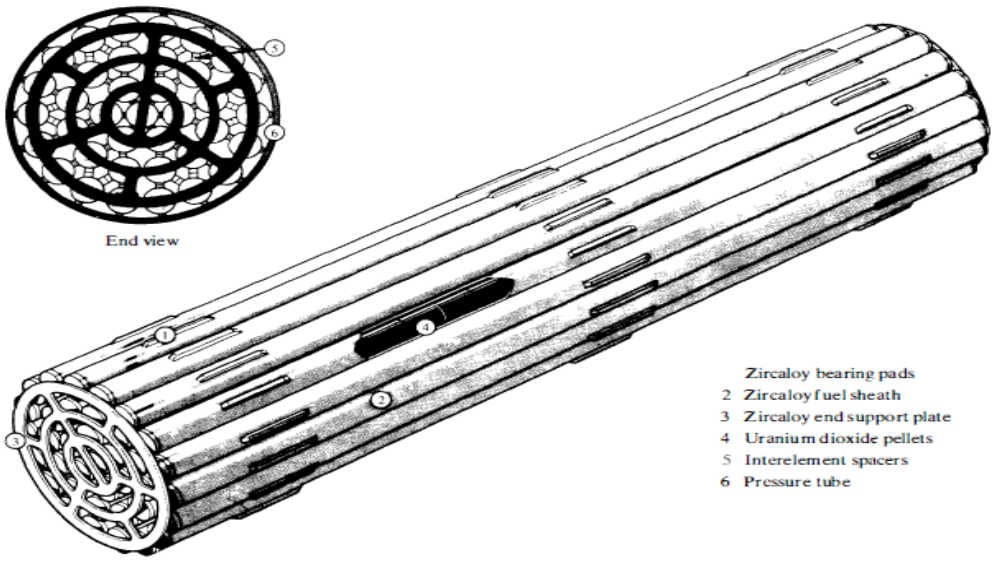

Figure 1.3 - CANDU element fuel bundle [26]

This thesis examines the local velocity and turbulence levels near flow obstructions. In order to isolate the effects from other complicated features within a fuel bundle, the experiments are performed under single phase conditions and using a simplified flow geometry. The local velocity and turbulence values are measured for a variety of asymmetric flow obstruction using Laser Doppler Velocimetry (LDV). Understanding the impact of these types of obstructions provides a foundation for improving our understanding of their larger role on the enhancement of CHF in a complex fuel assembly. These benefits would be applied not only to the nuclear industry, but to other engineering fields where heat exchange and CHF are of interest.

1.2 - Thesis structure

This thesis is composed of five chapters. Chapter 2 will briefly review literature related studies, including the impact of turbulence on CHF/PDO heat transfer, experimental and simulation based investigations of local turbulence. Chapter 3 will describe the experimental facility and equipment used for the experiments as well as the methodology implemented to analyze the collected data. Chapter 4 will present the results of the performed experiments and the analysis of the collected data. Finally, Chapter 5 will summarize the results of the present experiment for the study of turbulent single-phase pipe flow with variable obstructions. There are also 2 appendices with corrections for LDV measurements and sources of error and experimental uncertainty.

2. Literature Review

For more than five decades, the nuclear industry devoted many resources on the studying of thermal hydraulics and its impact on safety, which includes the study of the complex flows from the molecular scale through plant scale simulations. Codes employed include computational fluid dynamics (CFD), specific sub-channel analysis codes, and plant wide codes; all with vary degrees of assumptions and constitutive relationships. While the field of thermal hydraulics is vast, the focus of this thesis is on turbulence near flow obstructions and aims to provide new experimental data which can be used to better predict and understand the heat transfer and CHF augmentation which may occur. In this chapter a review of some key concepts and papers related to turbulence and its impact on CHF are presented.

2.1 - The Impact of Turbulence to CHF and Post-Dryout (PDO) heat transfer.

Critical heat flux (CHF) refers to the sudden decrease in a heat transfer coefficient on a surface under two-phase boiling conditions. Although a variety of CHF models have been proposed, no universally acceptable mechanism has been shown to predict CHF in all cases, since the phenomena involved are dependent on local flow conditions. In general most CHF models can be classified into 5 categories:

1. Bubble crowding - in this mechanism, nucleation activity is highly intense on the heated surface leading to very elevated nucleation site density. In such case, many bubbles may combine from several nucleation sites and form a local dry-patch.
2. Macro layer dryout - in this mechanism, several nucleation sites contribute to the formation of a larger bubble located a short distance away from the wall. Depending on

the size of this bubble and the local flow conditions, it may be carried away with the flow, or if it resides in close proximity to the wall long enough, the liquid trapped between this bubble and the heated surface may evaporate, causing the occurrence of film boiling under the bubble.

3. Micro layer evaporizaton - in this mechanism, a bubble grows and spreads out from a nucleation site on a surface with a very thin layer of liquid under the bubble. In this layer, Marangoni Flows (the mass transfer along an interface between two fluids due to surface tension gradient) replenish some liquid from the surrounding medium back towards the center of the nucleation site. Depending on the local conditions and heat flux, the thin liquid layer under the bubble may evaporate prior to the bubble departure, leading to a local dry-patch.
4. Liquid flow restriction - also referred to as jets and columns, this mechanism involves jets of vapor generated at the surface, which move laterally away from the heat transfer surface. If these jets carry enough velocity, they may limit the flow of liquid back towards the surface, resulting in surface dryout.
5. Liquid film dryout - in this phenomenon, the two-phase flow regime is annular liquid film, where the liquid flows along the heated surface as a thin liquid film and the core of the flow is predominantly vapor.

While the mechanisms leading to CHF are complex, it is widely believed that turbulence in the vicinity of CHF acts to disrupt dryout mechanisms and enhance liquid transport towards the heated surface. Also, in many applications the prediction of dryout is typically made using empirically derived correlations, with these either having explicit terms to modify CHF in the presence of an obstruction or implicitly containing such corrections. When a calculation of the

predicted local heat flux exceeds the CHF correlation, dryout is predicted and adjustments are made to the heat transfer coefficients within the code.

PDO heat transfer includes transition boiling, where intermittent wetting of the heated surface takes place, and film boiling, where the heated surface is too hot to permit liquid contact. The boundary between these PDO heat transfer modes is the minimum film boiling temperature. Depending on the accident scenario, the fuel sheath temperature may undergo significant increases, making CHF undesirable since such temperatures over prolonged periods of time may lead to failure of the sheath

A turbulent boundary layer behaves like a composite system consisting of a thin, low conductivity sublayer, beneath a thicker more conductive buffer layer and the larger conductive turbulent core (Figure 1.1). Turbulence is generated in the buffer layer (which is located between the thin viscous sublayer and the turbulence core of the flow). The thermal resistance of the viscous sublayer is much higher than that of the buffer and turbulent core, since heat transport is limited to laminar phenomena. The strong production of turbulence in the buffer region is responsible for eddies which interact with the viscous sub layer and hence transport heat away from the wall and towards the turbulent core. In nuclear applications involving surface boiling, nucleation/vaporization greatly enhances the local generation of turbulence, due to bubble formation/deformation/collapse and surface rewetting, increasing the local heat transfer coefficient. Due to the CHF mechanisms discussed previously, there is a limit to the heat flux that can be applied in boiling systems beyond which the convection coefficient decreases substantially. As discussed previously, many fuel assembly designs also include flow obstructions, which also act to increase local turbulence and attempt to increase CHF thereby increasing the power density that can be dissipated.

A number of researchers have investigated the effect of spacing devices on CHF and PDO heat transfer [1–3]. In general because of the contraction of the flow area at the obstacle location, the convection heat transfer between the wall and the fluid is enhanced at the obstruction location and persists for some distance downstream of the obstruction. The enhancements observed decrease with distance downstream of the obstruction, since turbulence generated near the obstruction is dissipated steadily in the Streamwise direction. Eventually the additional turbulence generated near the obstruction is dissipated and the convection coefficient reduces to that expected for flows without the obstruction. In these experiments a significant increase in local CHF was also observed downstream of the spacers, primarily due to the higher turbulence level of the two-phase flow. In an actual fuel bundle spacers also play an important role in that they promote lateral pressure gradients inside the bundle thereby enhancing the mixing of fluid between sub-channels, hence preventing a single sub-channel from undergoing significant enthalpy imbalance as compared to the surrounding sub-channels. Sub-channel enthalpy is an important variable in CHF phenomena (along with pressure and mass flux). Therefore obstructions play two roles in the enhancement of CHF in a complex bundle flows. First, it results in higher turbulence level, which improves CHF. Secondly, it enhances sub-channel mixing which prevents a single sub-channel from overheating and thus prematurely reaching CHF. In these base studies the enhancement decays exponentially to the previous CHF between 30 and 50 L/D downstream. Another feature of spacers in direct contact with a fuel element is that it may act as a fin, extending the heat transfer surface area locally and thus also reducing the local heat flux to some extent. The significance of this last mechanism has not been widely established in literature.

2.2 - Simulation based investigations of local turbulence

Kim *et al* [4] authored one of the most sited numerical works related to turbulence in 1987 entitled "turbulence statistics in fully developed channel flow at low Reynolds number". The unsteady Navier-Stokes equations were solved at a Reynolds number of 3300, based on the mean centerline velocity, with 3962880 grid points (192 x 129 x 160, in x, y, z) and channel half-width **δ** (a Reynolds number of 180 based on the wall shear velocity u_t), using direct numerical simulation (DNS). The streamwise and spanwise computational periodic boundary conditions were chosen to be $4\pi\delta$ and $2\pi\delta$ with $\Delta x^+ \approx 12$ and $\Delta z^+ \approx 7$ respectively of grid spacing's in wall units. All essential turbulence scales were resolved on the computational grid without using sub-grid models. A large number of turbulence statistics were computed and compared to existing experimental data at comparable Reynolds numbers of 15000-45600. The fully developed turbulent channel flow was homogeneous in streamwise and spanwise direction, and periodic boundary conditions are used in these directions such as to include the largest eddies on the flow. The flow geometry and coordinate system are displayed in Figure 2.1.

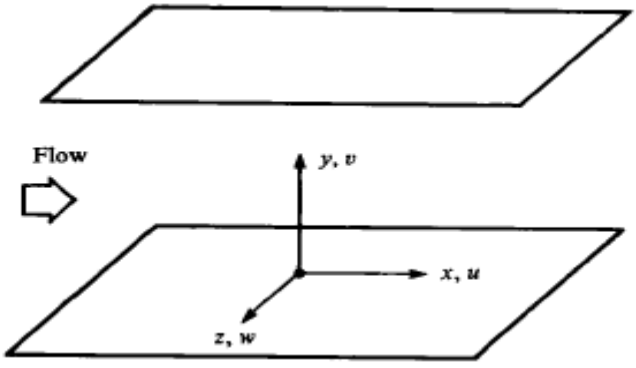

Figure 2.1 - Coordinate system in channel

The author concluded that the general characteristics of the computed turbulence statistics were in good agreement with experimental results illustrated in Figure 2.2, but detailed comparison in the wall region reveals discrepancies. In particular, the computed Reynolds stresses - both the normal and the shear stresses - are consistently lower than the measured values, while the computed vorticity fluctuations at the wall are higher than the experimental values.

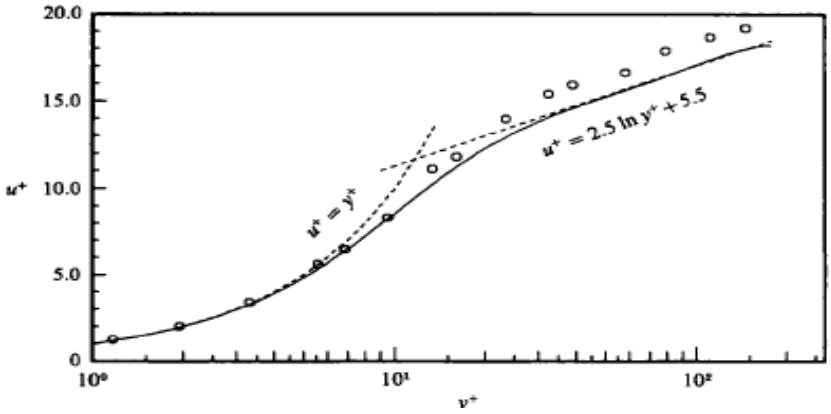

Figure 2.2 - Mean-velocity profiles: -, upper wall; ---, lower wall (masked by solid line); o, data from Eckelmann (1974); ----, law of the wall

Khoury and Barri [5], used DNS to simulate asymmetries in an obstructed turbulent channel flow.

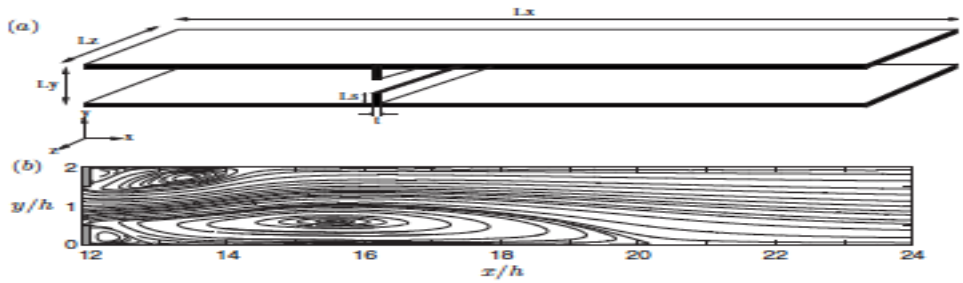

Figure 2.3 - a) Problem Configuration, b) Streamlines of the mean flow

Figure 2.3 illustrates a schematic view of the simulated test section which consisted of a channel of height 2*h* and two-dimensional slits with t=0.1h of thickness and L_s=0.5h of height mounted at x=11.9h. The ratio between total height of the slits and the downstream channel (I.e., 2Ls/Ly = of-1: 2), and the bulk Reynolds number of 5700. The time dependent incompressible Navier-Stokes equations for a viscous fluid were non-dimensionalized by *h* and $u_{\tau i}$. A total of about 25×10^6 grid points have been used. Stretching was employed in the streamwise and wall-normal directions in order to adequately resolve the turbulence scales in the mixing-layers, reattachment regions, as well as in the vicinity of the walls, whereas a uniform mesh was used in the spanwise *z*-direction

Figure 2.4 illustrates the upstream mean velocity profile plotted at *x/h*=5 and these results compare well to Kim *et al.* in terms of the velocity profile, computed turbulence intensities and the total mean shear stress.

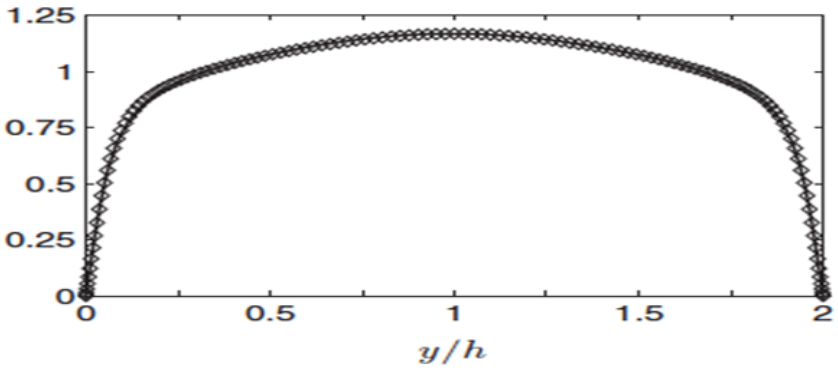

Figure 2.4 - Mean streamwise velocity profile U normalized by Ui at x/h=5: ——, present computation; ◊ , Kim et al

The authors observed that the fluid downstream of the obstruction was pushed to one side where a long region of strong recirculating flow was observed. On the opposite side of the channel, a

weaker recirculation region was formed. The contribution of this paper was to demonstrate the non-symmetrical behavior of the numerical solution even when all geometries and boundary conditions were symmetric. Overall the downstream flow pattern was different from a similar study with of channel flow subjected to periodical obstructions by Makino *et al* discussed below.

Makino *et al* [6] studied turbulent channel flow with periodic two-dimensional slits, using DNS in order to investigate the turbulent statistics and structures behind the slits, Reynolds numbers based on friction velocity of 10-1500 were studied. The periodic boundary conditions were applied in the streamwise (x) and spanwise (z) directions, (Figure 2.5a) and no-slip boundary conditions were used on all the walls. The direct forcing immersed boundary method from Fadlum *et al* [7] was applied on the plates in each side of the obstructions in the shape of slits. The regular grid is applied in the streamwise direction to use the Fast Fourier Transform (FFT) in the solution of pressure-Poisson's equation and a large mesh number was applied in the streamwise direction ($12.8\delta \times 2\delta \times 6.4\delta$), with grid number varied from 78×10^4 ($128\times96\times64$) to 13×10^7 ($1024\times256\times512$). In the wall-normal direction, the density of the computational mesh is higher at the height of the slit edges and near the walls (Figure 2.5b).

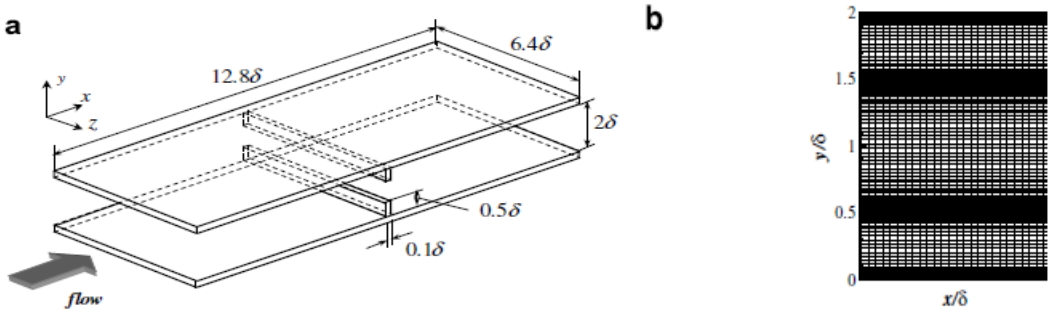

Figure 2.5 - a) Configuration of computational domain b) computational mesh

The author concluded that mean flow becomes asymmetric behind the slit because of the Coanda effect (the tendency of a fluid jet to be attracted to a nearby surface), which can be observed for $30 < Re_{\tau o} < 1500$, i.e., $180 < Re_b < 7800$. The Reynolds number dependence upon the reattachment length is similar to those described in the case of the backward-facing step experiments from Armaly *et al.*, 1983. A sharp decrease in the reattachment length is observed at $Re_b \approx 400$ which, is the transition from laminar to turbulent flow in this case.

Nygard and Andersson [8] numerically simulated turbulent pipe flow through an abrupt axisymmetric constriction using an immersed boundary method (IBM). An axial pressure gradient sufficient to keep the bulk flow constant at *Ub* is the driving force. The incompressible Navier-Stokes equations in cylindrical coordinates were solved on a computational mesh with the number of grid points in θ, r and z directions equal to 128, 170, and 256, respectively. The grid was staggered and a sketch of the two types of computational cells is shown in Figure 2.6

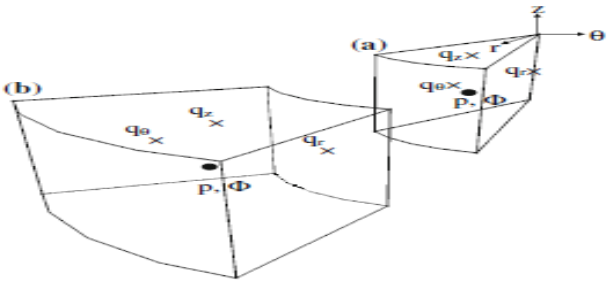

Figure 2.6 - Computational cells a) next to the center line, b) elsewhere

The simulation was carried at Re =4900, on a 5*D* length of computational domain, where *D* is the diameter of the cylinder. The axisymmetric constriction height *H* is half the constriction length *l* and a quarter of the pipe diameter. Figure 2.7 illustrates the flow configuration for the simulation.

The Navier-Stokes equations were discretized by a finite difference method with no-slip at the wall and periodic in the axial and azimuthal directions.

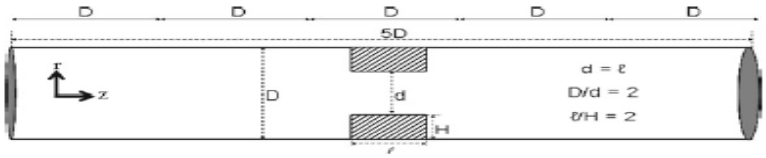

Figure 2.7 - Flow configuration of the axisymmetric computational domain and the cylindrical coordinate system

At 0.5*H* downstream of the constriction the velocity profile was severely affected and the bulk flow was deflected towards the axis of the pipe meaning $U_r < 0$. Then the flow was strongly accelerated through the ring constriction and decelerated again as the resulting jet spreads downwards of the constriction. Figure 2.8 illustrates that process.

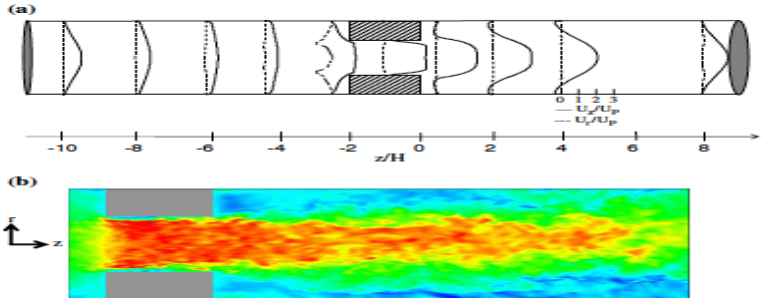

Figure 2.8 - a) Axial variation of mean velocity profiles, b) visualization of the instantaneous axial velocity

The mean flow field and the Reynolds stresses downstream of the ring were comparable with previous experimental data, but in the core regions of the pipe the Reynolds stresses were strikingly higher than the experiments due to the periodic boundary conditions in the streamwise direction. Also the results show some asymmetry with respect to radial coordinates despite the symmetry employed in the solutions. The authors however did not investigate this asymmetry nor

examine the potential azimuthal asymmetries (periodic boundary conditions were employed in the azimuthal direction which may have limited the amount of asymmetries observed)

2.3 - Experimental work

Roberts [9] conducted a numerical and experimental study for an incompressible Newtonian flow in a two-dimensional channel with several sharp edge baffles (figure 2.9). A fluid mechanics model based on the work of Sobey (1980) and Howes (1988), with no slip condition at the wall and on all baffles was employed for the numerical solution. The grid size was varied in order to establish a converged solution. The total number of grid points varied from 54 *(*6 x 9 grid) to 10578 (82 x 129 grid).

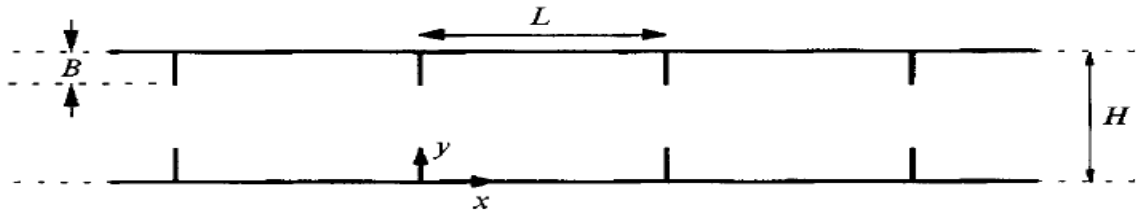

Figure 2.9 - The baffled channel geometry

A diagram of the experimental apparatus is shown in Figure 2.10. The test section consisted of a Perspex channel with periodically placed stainless steel baffles push fitted into the walls. The channel width was 25 mm, with an aspect ratio of 1:8, and a length of 1.3 m (34 baffles). The fluid used was a mixture of methylated spirits and water (60 % water, kinematic viscosity 2.535 x low6m 2/s at 20 "C).

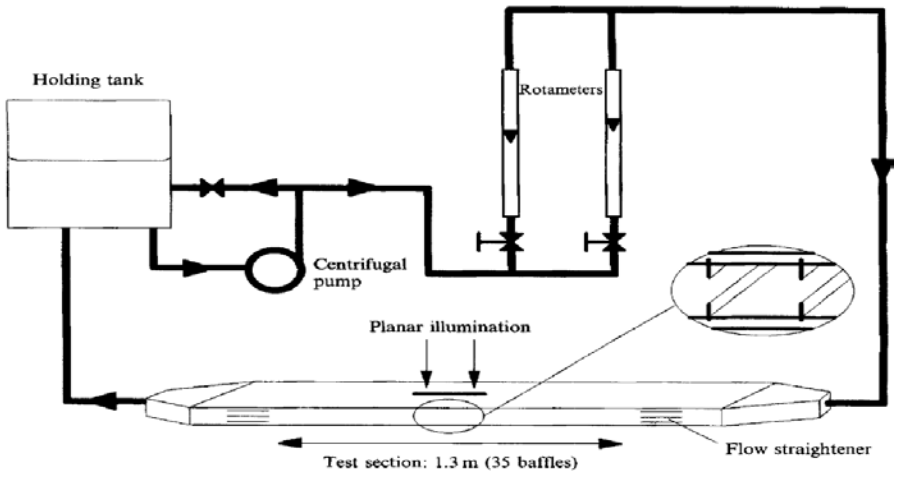

Figure 2.10 - Schematic diagram of experimental apparatus

The author concluded that for low Reynolds number *(Re* < 100) flow in baffled channels, a recirculating region was observed downstream of each baffle. With increasing *Re* the reattachment point was observed to move downstream until it became attached onto the downstream baffle. At *Re* ~ 100 (based on the channel width and cross-sectional mean velocity), the flow was observed both numerically and experimentally to become unsteady and asymmetric. The experimental observations showed that this led to a secondary transition to three-dimensional turbulent flow. The baffles have therefore acted as a turbulence enhancement device leading to early transition, which will improve engineering properties such as heat transfer.

Yao *et al.* [10] performed an experiment for a turbulent horizontal channel flow obstructed with an inserted square rod (i.e., open channel flow). A square rod was vertically inserted 1000 mm downstream from the inlet to the test section. The lateral position of the rod was changed and it is expressed with a clearance ratio defined as $y' = 2c/(H - d)$, where d = 10 mm is the rod thickness, H = 50 mm is the width of the channel, and c the space between the square rod and the channel wall. Figure 2.11 illustrate the test section arrangement. Measurements were executed in a

streamwise region with x/H=5 in horizontal layer of 10 mm vertical thickness; i.e., from 240 mm to 250 mm from the bottom of the channel or from 50 mm to 60 mm down from the free surface.

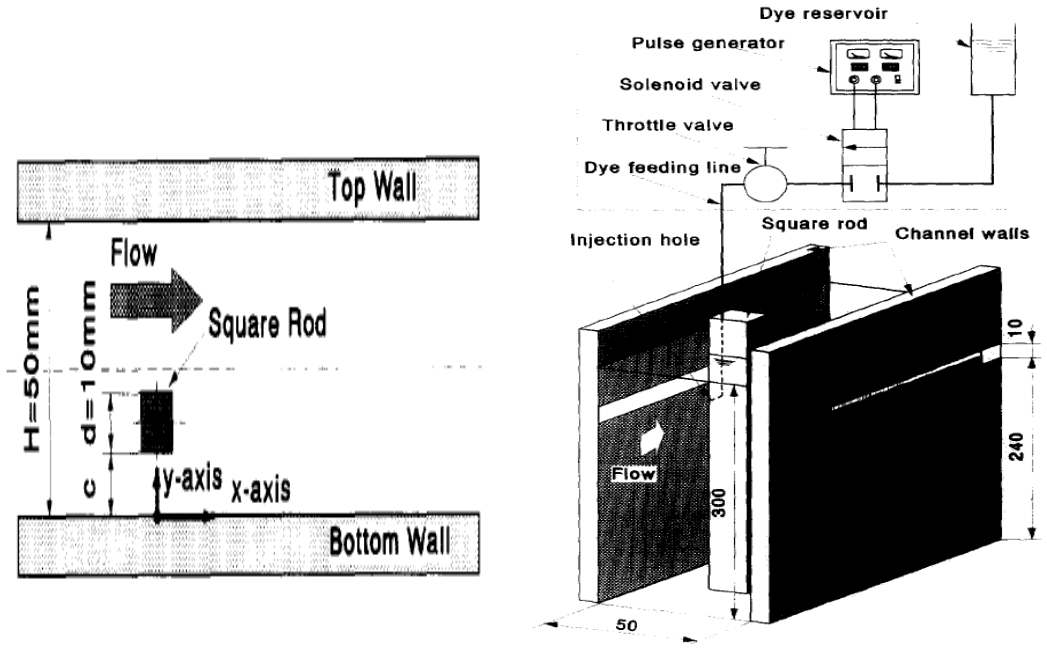

Figure 2.11 - Geometry of test section and detailed view with apparatus

Figure 2.12 depicts the velocity profiles upstream of the rod in the horizontal and vertical planes, at a Reynolds number of 10,500.

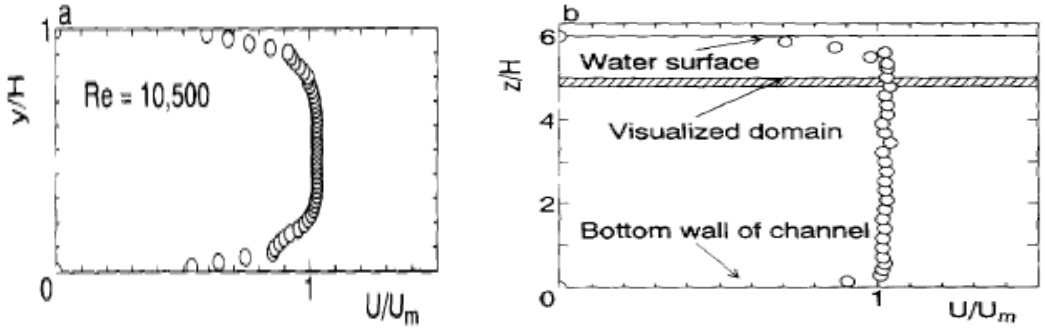

Figure 2.12 - Velocity profile without the rod a) horizontal plane, b) vertical plane

The author concluded that when a turbulent water channel flow at Reynolds number range of Re ≥ 6000, the obstruction creates strong disturbance that promotes the interaction of near wall flow with the Von Karman Vortex, which showed oscillating motion (unsteady flow) that could not be suppressed. The presence of periodic flow structures and their interaction with the free surface was a major contribution from this work.

Chang *et al.* [11] presented results from an experiment entitled " Phenomenological investigations on the turbulent flow structures in a rod bundle array with mixing devices". The experiment was conducted in a cold water test loop, with Reynolds number of 48000, using 2D LDV. The test section consisted of 5 X 5 rod bundle array with 25.4 mm of diameter incased in a 170 mm X 170 mm square (Figure 2.13). The rod bundle had 2 spacer grids, the first was downstream of the test section without any mixing devices, the second is downstream, with Split type and Swirl type mixing devices.

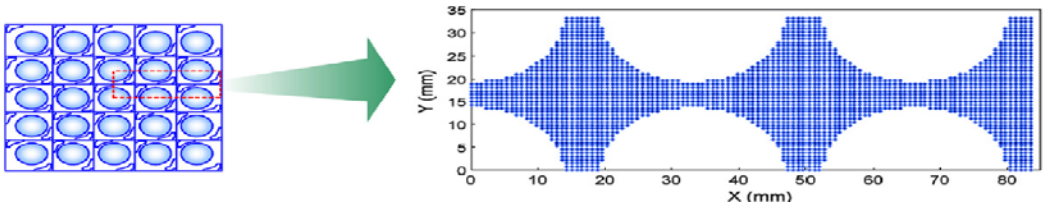

Figure 2.13 - Cross-sectional configuration of the test section and the investigation region

The author concluded that the split type mixing vane generated two symmetric co-rotating small vortices that decayed as the flow moves downstream. For the swirl type, one large vortex of an elliptic shape was generated and that the swirl type may have better performance for a mixing between sub-channels when compared to the split type. However, the turbulent intensity in the case of the split type is larger than that in case of the swirl type just behind the mixing devices and

decays exponentially in both cases in a similar way as the flow moves to the downstream as shown in Figure 2.14.

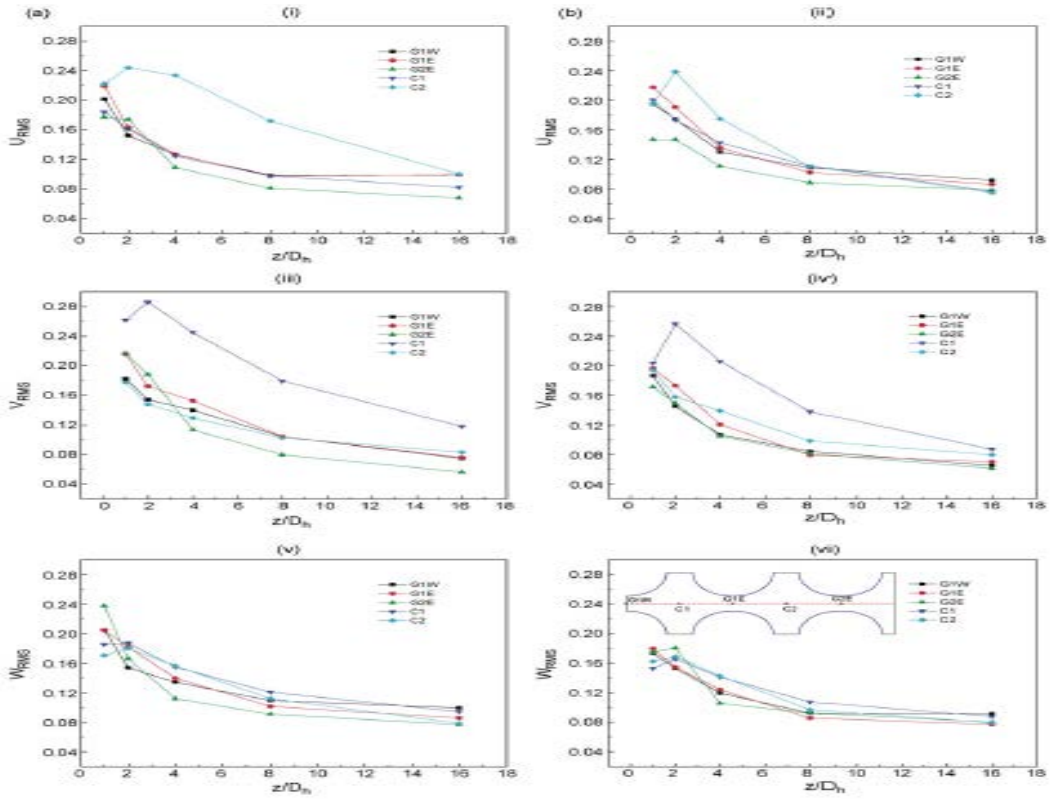

Figure 2.14 - Turbulent intensity decay. a) Split; b) swirl type

Chang *et al.* [12] used the computational Fluid Dynamics (CFD) code of STAR-CCM+ 4.02 to simulate the test section from the experiments described above [11]. A total of 10,140,474 and 10,286,576 mesh cells were produced as a base case for the split and swirl type vane, respectively. Dense mesh models for the split and swirl types were developed as shown in Figure 2.15. Standard k-ε and The Reynolds Stress Model (RSM) were used for turbulence models. 5,000~6,000 iterations were performed as a steady state until the residual of mass, enthalpy, and velocity reached below a value of 1.0E-04.

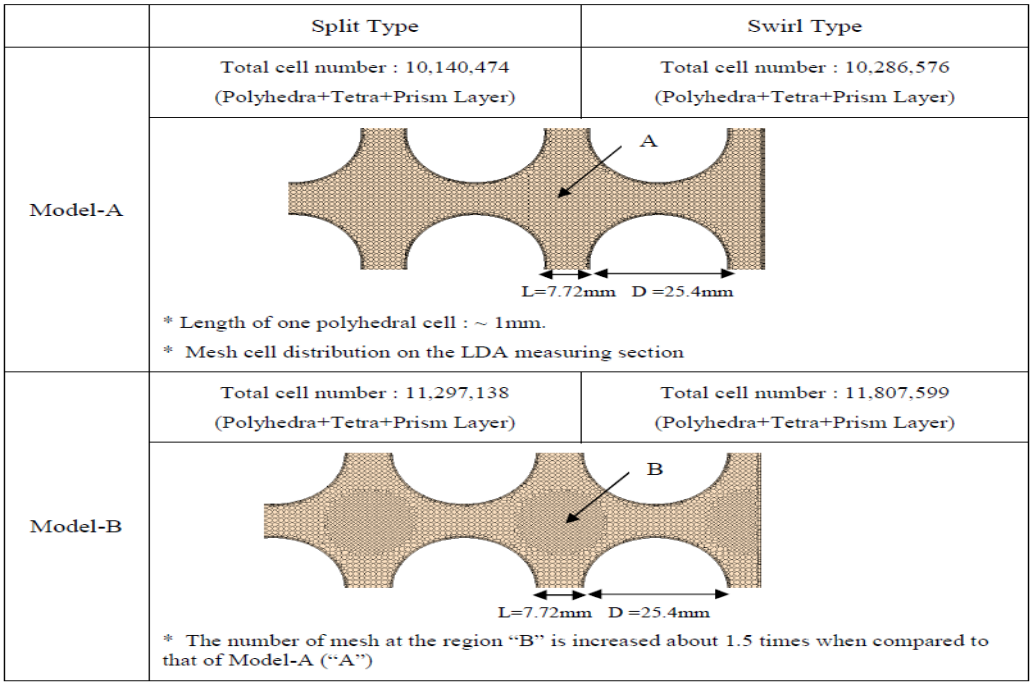

Figure 2.15 - Specification of Grid models A and B

They concluded that the CFD analysis results predicted the axial and lateral velocity profile of the test data at 1 D_h well, except the corner sub-channel region, but overestimated 10~20% for all sub-channels at 2 D_h. The steady CFD results also could not predict the change of turbulent intensity due to the generated vortices around the mixing devices, therefore unsteady and anisotropic turbulence models may be required.

Further work was also done by Chang *et al.* [13], for a second experiment for a 5 × 5 rod bundle with the same mixing devices, and similar flow and loop characteristics, using non-commercial spacer grids. Detailed measurements of the turbulent flow in the sub channels were accomplished using 2-D LDA at four different distances (0.5, 1, 4 and 10 D_H) downstream of the mixing spacer grid. The authors concluded that the lateral velocity fluctuations caused by the mixing vanes are reduced as the flow moves downstream, the turbulence intensities and vorticities also gradually

decayed. The axial velocity profiles show complicated fluctuations caused by the mixing vanes near the spacer grid, but are smoothened as the flow goes downstream. Similar to that discussed above, the shape of the vortices in the sub channels is more elliptic in the case of the split-type spacer grid but is circular in the case of the swirl-type spacer grid. The lateral flow mixing performance in the sub channels is superior in the case of the 'split-type' spacer grid compared to the case of the 'swirl-type' spacer grid.

Podila *et al.* [14] performed a study very similar to [12], where a 5×5 rod assembly with a split-type spacer grid is simulated with ANSYS Fluent 14 using unsteady simulations with a fully conformal hybrid mesh (wall y^+ ~30). A segregated solver based on the Gauss-Seidel technique with multi-grid V-cycle acceleration was used and the SIMPLE algorithm is employed for pressure-velocity coupling. An overall mesh count of 15.31 million cells was used with limited resolution near the walls due to hardware limitations. Two turbulence models, k-ε and RSM with linear pressure strain, were tested using the Unsteady Reynolds-Averaged Navier-Stokes (URANS) approach for the entire solution domain. The authors concluded that URANS RSM solution methodology along with a mesh count of 15.31 million cells under predicted the turbulence intensity due to the generated vortices behind the spacers. The predicted circulation for the trimmed sub channel was in closer agreement with experiments, which neglected steep vorticity variation in the near wall region.

Caraghiaur *et al.* [15] did an experimental investigation of turbulent flow through space grids in fuel rod bundles resembling a boiling water reactor (BWR), in a test loop illustrated in Figure 2.16.

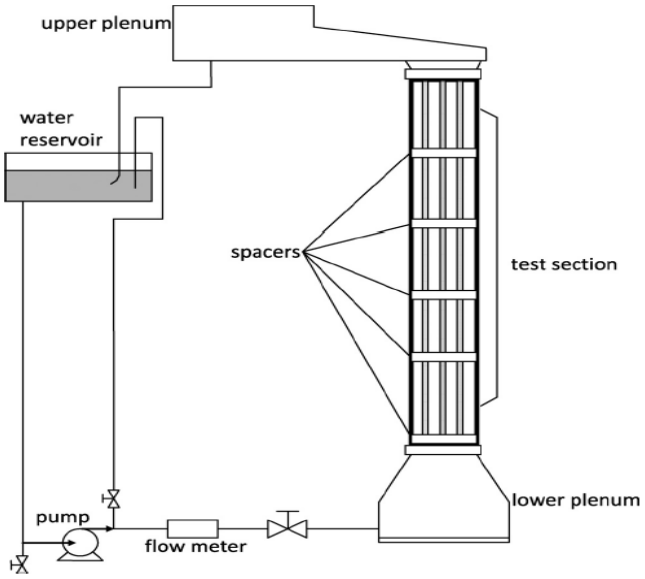

Figure 2.16 - Sketch of the test loop

The test section is a vertical arrangement of 24 rods with a diameter of 9.62 mm, held in position by 5 spacers of thin plate spring construction. The spacers contained dimples, frame vanes and springs, which for this experiment functioned as obstructions. The rod arrangement was surrounded by 10 mm thick glass plates to allow for velocity measurements across the spacer grid at Reynolds number of 25000; 32000 and 42000. Figure 2.17 illustrates the cross sectional view of the test section.

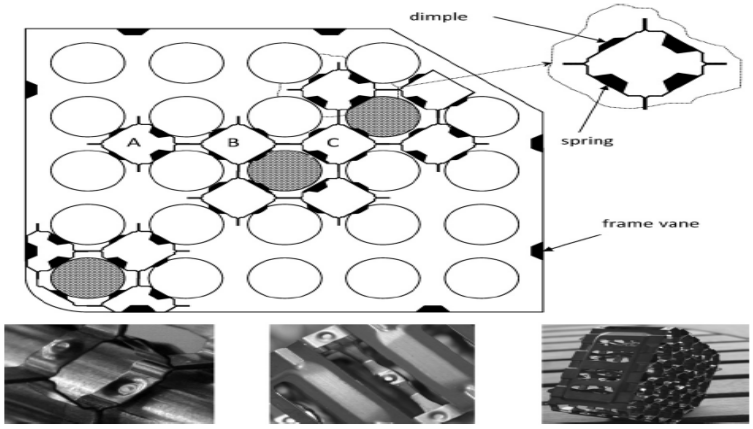

Figure 2.17 - Cross-section of the test section indicating spacer elements

The author concluded that the local velocity in the center of each sub-channels rise suddenly downstream of the obstruction and the Reynolds number increased by 25% but the distance necessary to redevelop the flow varied by sub-channel. Also the turbulence enhancement downstream of the obstruction for sub-channel A due to its proximity to the box wall was comparable to the Nagayoshi and Nishida correlation:

$$\frac{\sqrt{u\prime_{sp}^2}}{\sqrt{u\prime_{o}^2}} = 1.0 + 6.5\theta^2 . e^{-0.27z/Dh} \quad (2.1)$$

However, for sub-channels B and C, the turbulence decreased downstream of the spacer and then gradually increased to maximum 2 spacer lengths from the obstruction, followed by the typical decay. Figure 2.18, illustrated these sub-channel dependent phenomena. Results from the study in this thesis reported in subsequent chapters shows similar phenomena wherein the peak turbulence intensity under some flow conditions occurs 1 to 2 diameters downstream,

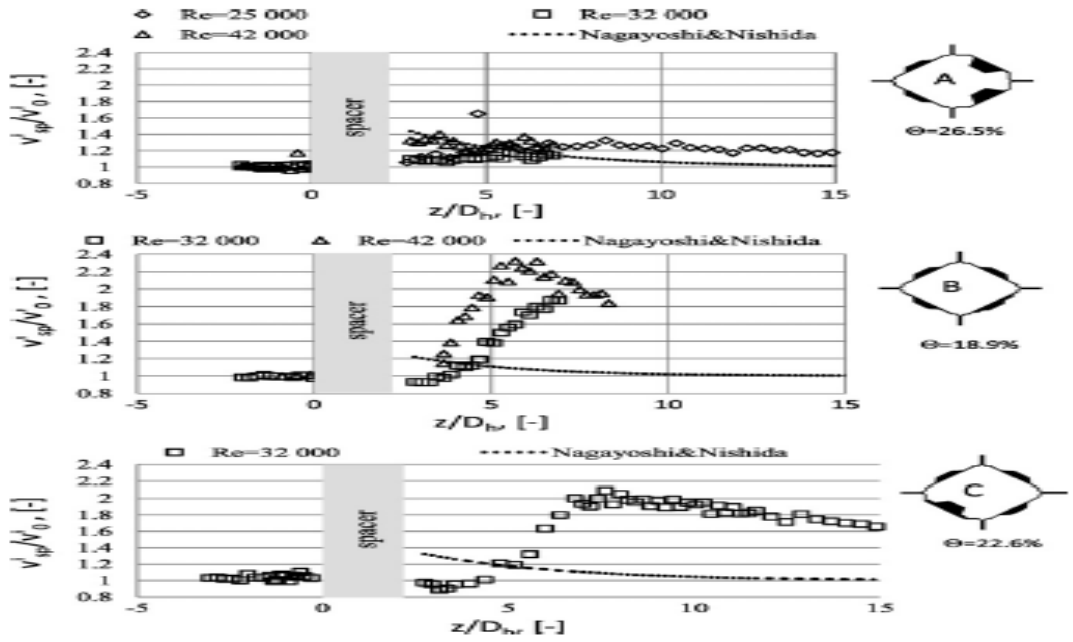

Figure 2.18 - Axial velocity fluctuating component downstream and downstream of the spacer for 3 sub-channels

Hassan *et al.*[16], performed measurements within a 5 × 5 PWR rod bundle with mixing vanes spacer-grids using two-dimensional Time Resolved Particle Image Velocimetry (TR-PIV) as shown in Figure 2.19. An aluminum frame with a polycarbonate channel walls formed the test section. The spacer grid used for these experiments models a Westinghouse support grid design which is used in actual nuclear fuel assemblies for PWR, with a spacer pitch of 510.54 mm. The rods were fabricated using a fluorinated ethylene-propylene (FEP) plastic with dimensions of 9.5 OD×9 ID × 1270 mm long with a ±0.0762 mm tolerance in all dimensions. The test rods were closed at each end using a coned aluminum caps and filled with a solution of water and chlorine in a 5% by volume concentration. The FEP elements were designed to match the optical properties of the water to allow for more detailed PIV measurements.

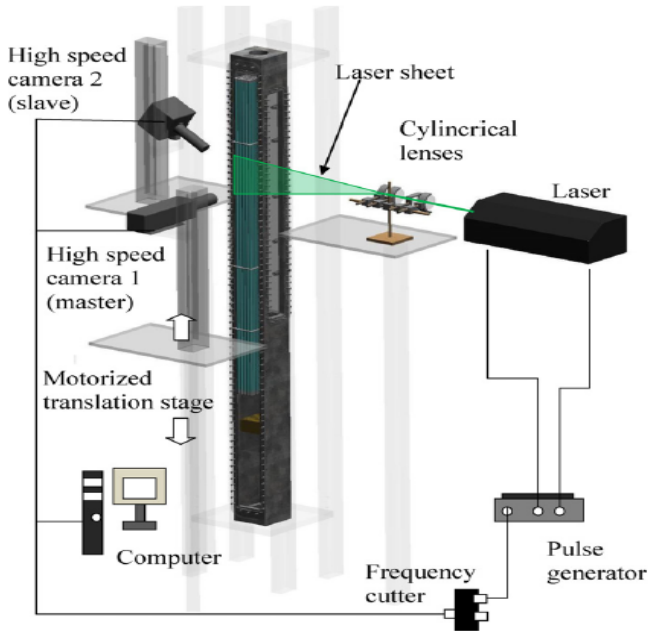

Figure 2.19 - Optical system and location with respect to test section

In this experiment the averaged streamwise component of the velocity vector (U) showed a decrease of 30% in the regions immediately above the mixing vanes (downstream) with respect to the results obtained in the regions immediately below the spacer (downstream). The normal component of the velocity vector (V) showed an increase in magnitude near the split vanes of 50% due to the deflection caused by the split vanes. Turbulence intensities in the streamwise direction (u') have an averaged value of 20% of the maximum velocity (U_{max}) as compared to the upstream turbulence levels of 10%.

2.4 - Summary

The interest in turbulent flow with obstructions characteristics has increased significantly in the recent years, especially with the introduction of MATIS-H international benchmark. This includes higher fidelity measurements as well as CFD modeling. To the author's knowledge, no

experimental work has been done to understand the impact of bearing pad spacers on local velocities and turbulence levels at scales representative of CANDU fuel geometries. This work provides new experimental measurements of the effect of CANDU type obstructions on single sub-channel flows.

3. Experimental Description and Methodology

This chapter presents an overview of the test facility, the flow channel, obstructions, and instrumentation used. A brief description of lab facility and test section is presented in Section 3.1. Section 3.2 discusses the basic principles and procedures of the LDV equipment used. Section 3.3 establishes the methodology approach used during the experimental work, to obtain the data. Section 3.4 describes the validation study for the constructed test section

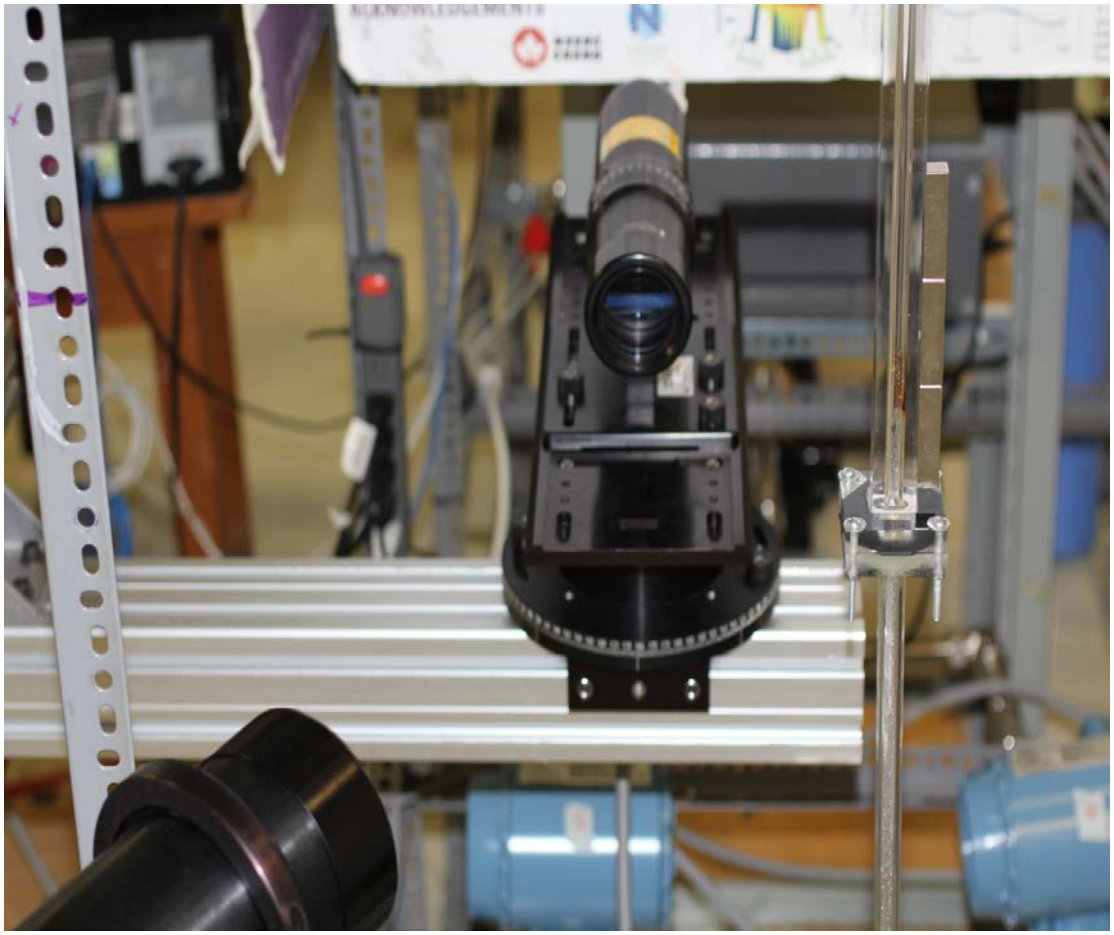

Figure 3.1 - Experimental loop

3.1 - Experimental Setup

3.1.1. Flow Loop

The experiments have been conducted in the low-pressure low-temperature flow loop, illustrated in Figure 3.2 and located at a laboratory in the nuclear research building at McMaster University. A 120 L capacity reservoir feeds water at room temperatures (20 ~ 24° C) to a 3 hp/2.24 kW pump, regulated by a variable frequency drive. The pump supplies a 2.4 m (94.5”) long horizontal stainless steel pipe which leads to an aluminum machined inlet manifold. From the inlet manifold the flow travels through a vertical 0.660 m (26”) clear acrylic tube with 0.0095 m (3/8”) inner diameter that gradually expands to 0.0111 m (7/16”) and 0.0159 m (5/8”) outer diameter development length. After the development length the flow passes through a 0.3048 m (12”) test section (square outer dimensions with an interior machined circular flow section), with details provided in section 3.1.3. The outlet from the test section travels through another 0.3302 m (13”) clear acrylic tube with 0.0095 m (3/8”) inner diameter and 0.0159 m (5/8”) outer diameter. Finally the flow goes through an aluminum machined outlet manifold and then through another horizontal stainless steel pipe and back to the reservoir. Table 1 contains the key characteristics of the loop.

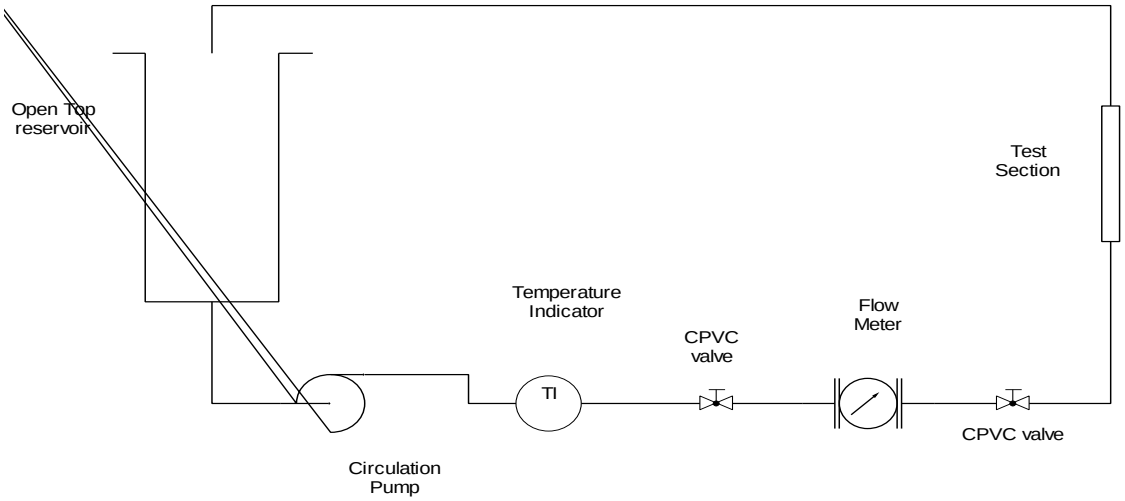

Figure 3.2 - Schematic of flow loop

Table 1- Key characteristics of the loop

Loop	
Working Fluid	Water
Fluid Temperature (^{o}C)	20-50
Max Mass Flow Rate (kg·s^{-1})	2.00
Max Reynolds Number (-)	(1.5)(10^{5})
Operating Pressure (kPa)	101.3

3.1.2. Instrumentation

The 2.4 m horizontal aluminum stainless steel inlet pipe contains the magnetic flow meter and the Platinum Resistive Temperature Device (RTD). An Omega DP-18 temperature indicator and power supply connected to the RTD which is housed within a stainless steel thermowell and connected to the loop using a NPT fitting. The accuracy and uncertainties for the RTD are in table 2.

Table 2 - Accuracy and uncertainties for the RTD

Parameter	Value
Range	-150.0 to 199.9° C
Accuracy	0.4° C ± 0.05%
Resolution	0.1° C

The Rose-mount 8732E magnetic flow meter is located between the pump and the inlet block connected to the loop via flange connections with appropriate upstream and downstream development lengths as specified by the manufacturer. General technical specifications for the device are listed in table 3, while the accuracy and uncertainties are quantified in table 4.

Table 3 - Technical specifications of the magnetic flow meter

Parameter	Value
Line Size (ID)	25.4 mm
Liner Material	PTFE
Low Flow Cut off	0.012 m/s
Maximum Flow Rate	12.00 m/s
Configured Range	0 – 5 m/s
Output Range	4 – 20 mA
Operating Temperature Range	-29 −177 ^{o}C

Table 4 - Accuracy and uncertainties for the magnetic flow meter

Parameter	Value
Base Accuracy	±0.25% of flow rate
Analog Output Accuracy	±4 µA
Repeatability	±0.1% of reading
Stability	±0.1% of rate over 6 months

Ambient Temperature Effect	±0.25% over temperature range

3.1.3. Test section and obstructions

The test section is composed of 2 parts to facilitate easy access to change the obstructions and replacement if needed. The first is a machined 0.3048 ± 0.002 m (12") long 0.0254 X 0.0254 ± 0.0015 m rectangle, manufactured from a single cast acrylic square block. An extrusion cylindrical path is machined along its axis of 0.0111125 ± 0.0005 m (7/16") in diameter with a surface roughness ε of 9 μm. the square outer dimensions and cylindrical inner dimensions were selected to minimize interference with optical LDV measurements. With a 0.0254 m (1") deep 0.0159 m -18 straight threads are machined for connection to the second section. This is the measuring portion of the test section, it is within this first part that the metal obstructions were magnetically attached and moved along to measure the velocity components.

The second part is a matching threaded 0.3302 m (13") clear acrylic tube with 0.0095 m (3/8") of inner diameter and 0.0159 m (5/8") outer diameter. The diameter of this section was selected to match that of the measuring section above and provides upstream development length for the flow; due to minor imperfections in fabrication this part couples 1.13° of angle. By uncoupling this spool piece from the measurement volume it is easy to exchange obstructions.

Figure 3.3 - Test Section

All 3 obstructions were made of keystock low carbon grade steel (see Figure 3.4). They all have a rounded bottom side that matches the curvature of the test section inner diameter of 0.0111125 m (7/16”). They have the same width and length dimensions but the heights are different to provide different flow blockage areas. In order to secure the obstructions under high flows three individual 0.0508 × 0.0127 × 0.0127 m Neodymium (N42) Rare Earth Magnets are used for each obstruction. The length and width of the obstructions were selected to be representative of a CANDU bearing pad while various heights were examined. Table 5 provides the dimension of the obstructions.

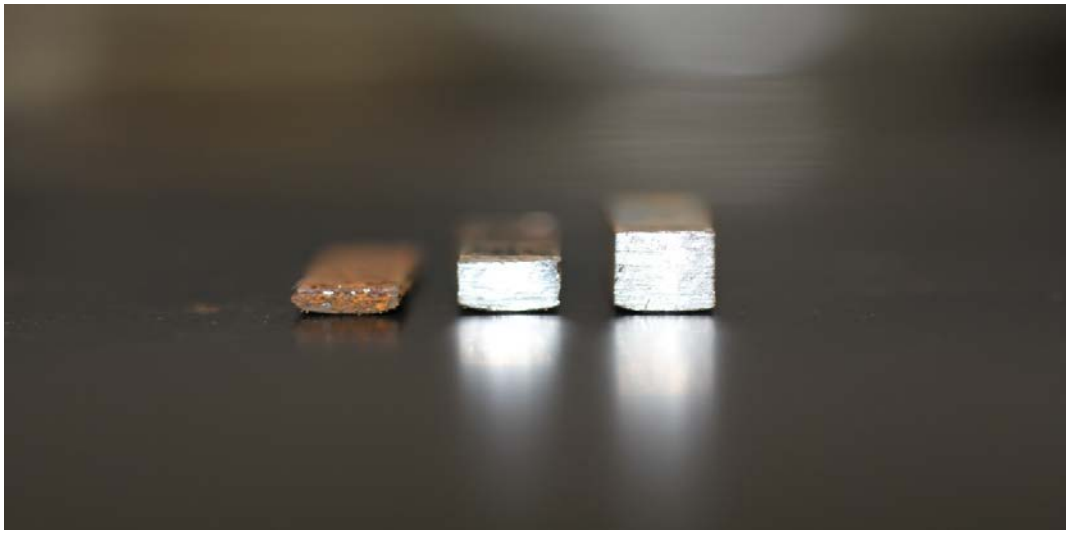

Figure 3.4 – Obstructions, note the corrode appearance of one obstruction, due to prolonged time in the test section).

Table 5 - Dimension of the obstructions

Obstructions	**Height (mm)**	**Length (mm)**	**Width (mm)**	**Streamwise Obstruction Area (mm^2)**	**Flow area blockage (%)**
1st 	1.27 ± 0.5	25.4 ± 0.20	5.08 ± 0.20	0.03995	41.19
2nd 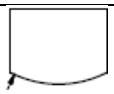	3.30 ± 0.5	25.4 ± 0.20	5.08 ± 0.20	0.05270	51.83
3rd 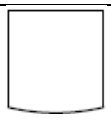	5.08 ± 0.35	25.4 ± 0.20	5.08 ± 0.20	0.05930	61.14

3.2 - Laser-Doppler Velocimetry (LDV)

3.2.1. Principles of LDV

Laser Doppler Velocimetry is a non-intrusive technique that uses the Doppler shift in a laser beam to measure the velocity of a fluid. The first laser Doppler instrument with an optical configuration know as reference-beam mode was present by Cummins in 1964 [17]. The currently used dual-beam mode was introduced almost simultaneously by Lehmann [18] and Vom Stein and Pfeifer [19], the latter of which were granted a patent. When the wavefronts of two coherent laser beams passing through the transmitting optics interfere at a certain angle within the measuring volume interference fringes (see Figure 3.5) with spacing d_f are formed. These bright and dark fringes are equivalent to a region where the amplitude of the laser beams construct or destruct each other, depending on their relative phases.

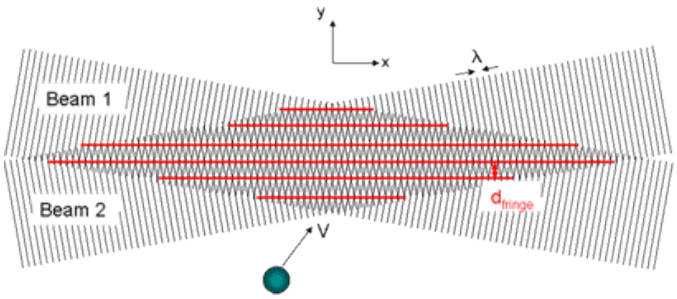

Figure 3.5 - Interference pattern in measurement volume [20]

Tracer particles transported by the flow through the volume will scatter light according to the constructive or destructive interference fringes, yielding the Doppler frequency at the detector. This frequency is determined for each individual tracer particle passing through the measuring volume, yielding flow velocity readings in time. The frequency of this scattered light will then

depend upon the spacing of the fringes (d_f), which is defined as the distance between the centerlines of two consecutive dark fringes, and the particle velocity (u_z). The fringe spacing is only a function of the half-angle between the laser beams (κ) and the wavelength of the laser illumination (λ):

$$d_f = \frac{\lambda}{2\sin\kappa}$$

(3.1)

The flow can be artificially seeded with tracer particles of an appropriate size range or with tracers naturally found in water flow. The velocity of the particle can then be calculated from the fringe spacing and the measured frequency of light scattered by the particle (f_D). Since many tracer particles pass through the volume statistics can be acquired which yield mean velocity and fluctuating components. Multiple laser colors can be used in slight different directions to provide multi dimension measurements simultaneously.

$$u_z = f_D d_f$$

(3.2)

Light is received by a photo detector module (PDM) with a photomultiplier tube (PMT) and is separated by color. The PMT produces an electrical current proportional to this light flux. Variations in this electrical current caused by the particle passing the fringes are subsequently analyzed to determine the velocity of the particle. In the forward scatter mode, the receiving optics and detector are placed on the opposite side of the flow from the transmitting optics, which yields higher signal levels and hence sampling rates in forward scatter, but the alignment of the receiving and transmitting optics is more complicated. The signal from the PMD becomes input for a signal processor, a device that isolates the signal from the background noise using a band

pass filter and amplifies the signal to extract information such as frequency, phase, burst transit and arrival time from these signals and sends it to the computer with the FlowSizer software .

If the two laser beams that interfere are of exactly the same frequency, the fringes will be stationary in the measuring volume, thus the particles with a certain velocity moving one way across the fringes may have exactly the same frequency as particles (having the same magnitude of velocity) moving in the opposite direction, making it impossible to determine if particles were moving in a positive or negative flow direction. To eliminate this problem in LDV systems, one of the two laser beams is frequency shifted by a Bragg cell by 40 MHz. These results in fringes that are essentially moving at a rate of 40 MHz in the measuring volume, and particles crossing the measurement volume will now have a frequency either above or below 40 MHz, depending on their direction. Thus the frequency of light scattered by a particle will be 40 MHz plus or minus an amount due to its velocity. If a particle is moving against the fringes, it will have a frequency of 40 MHz plus the Doppler frequency (the frequency due to the particle velocity) and if a particle is moving with the fringes it will have a frequency of 40 MHz minus the Doppler frequency. Frequency shifting also allows you to measure velocities near zero, where without the shifting there would be no oscillating pattern of light scattered from the particle at all.

3.2.2. LDV System and Procedures

The Velocities were measured using a two-component Laser Doppler Velocimetry system (TSI, Inc.) in forward scatter mode with a water cooled argon-ion laser (Coherent Innova 70C), with two vertical beams (green, at 514.5 nm wavelength) connected to channel 1, and two horizontal beams (blue, 488 nm wavelength) connected to channel 2, operated at 1.5 W of power. A Model XPD50-I beam expander was used for the Model TLN05-250 transmitter probe. The high-pass

filter was set to 20 MHz. the main components of the LDV system are shown in Figure 3.6 and listed in Table 6

Table 6 - List of LDV system main components

Type	***Item***	***Model No.***
LASER	Laser Laser table	Coherent Innova 70c
LDV	Fiberlight multicolor beam separator Input beam alignment tube Fiberoptic couplers Transmitting probe Receiving probe Beam expander 2:1	450205 CPL2001 TM 50 – TLN05-250 TLN07-300 XPD50-I
SINAL ANALYSIS	Multibit digital processor Photo detector module	FSA3500 PDM1000
SOFTWARE	FlowSizer windows XP	Version 2.0.4.0
TRAVERSING MECHANISM	Isel Microstep Controller Isel three axis motor controller	C 142-4.1 Marc 2.0 A

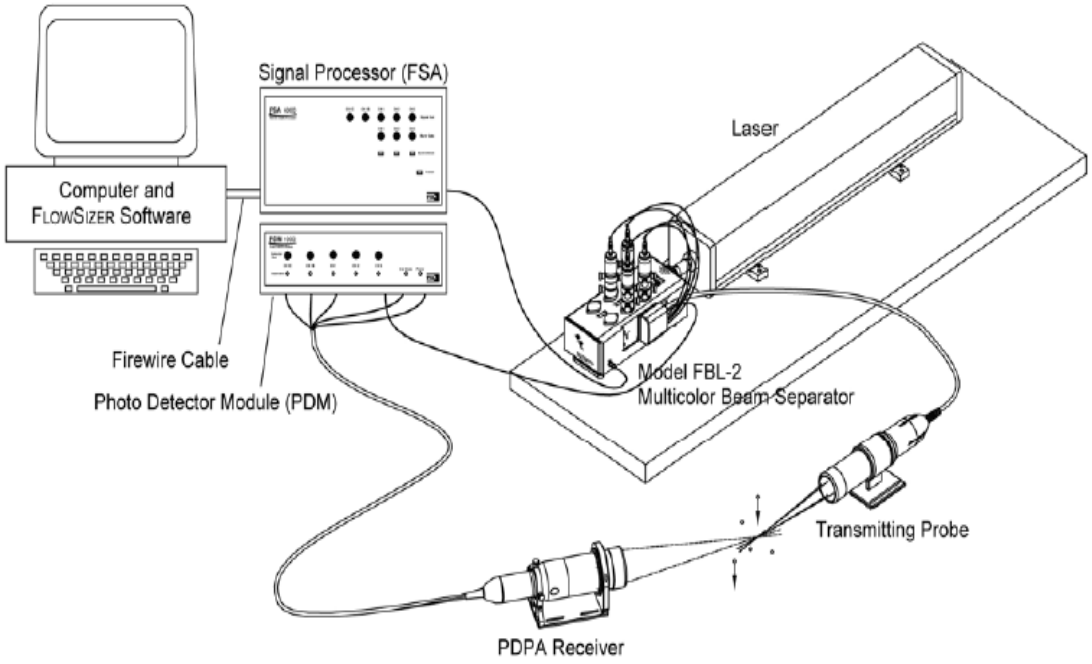

Figure 3.6 - LDV system components [21]

The measurement volume created by the intersection of the laser beams corresponds to the surface on which the light intensity of the fringes is $1/e^2$ of the maximum intensity, which occurs at the center of the measurement volume. Fringe spacing decreases with increasing angle κ. The measurement volume takes the shape of an ellipsoid whose dimensions can be calculated using the equations from the LDV/PDPA system manual [21]. The corresponding axes of the ellipsoid in the *x, y* and *z* directions are ℓ_m, d_m and h_m.

$$d_m = \frac{d_{e^{-2}}}{\cos\kappa} \tag{3.3}$$

$$\ell_m = \frac{d_{e^{-2}}}{\sin\kappa} \tag{3.4}$$

$$h_m = d_{e^{-2}} \tag{3.5}$$

$$d_e = \frac{4f\lambda}{\pi D_{e^{-2}}} \tag{3.6}$$

Here d_e is the beam diameter at the intersection of the beams. Using the above equations (3.3 - 3.8) and the parameters of the LDV system given in Table 7, the dimensions of the measuring volume ellipsoid are approximately 0.05 mm × 0.6 mm × 0.05 mm in the *x*, *y* and *z* directions. The volume of the ellipsoid can be calculated using the equation from the LDV/PDPA system manual [21]

$$V_D = \frac{\pi d_{e^{-2}}^3}{6\cos^2\kappa \sin\kappa} \tag{3.7}$$

Since the test section is square on the outside with a cylindrical flow channel on the inner side, it acts as a planar concave lens which distorts the laser and reflects light to some degree. This has the net effect of moving the location of the measurement volume slightly as compared to the case without lens. So the half angle of the beams κ suffers alterations while traveling through the different indexes of refraction (air, polished cast acrylic and water), altering the real location within the test section compared to the apparent position in the traverse system; therefore corrections were implemented to match the appropriate data points to the respective positions. For details of the positional correction please consult Appendix A.

Table 7 - Operating parameters of the LDV system

Parameter	***Symbol***	***Value***
Laser wavelengths (nm)	λ_1	514.5
	λ_2	488.0
Focal Length (mm)	f	250
Beam spacing (mm)	D_b	40
Beam diameter	D_e	3.54
Fringe spacing (μm)	d_{f1}	3.21
	d_{f2}	3.05
Beam half angle in air (°)	κ	4.60

The experiment procedures followed during of typical streamwise/azimuthal velocities are described in the following paragraphs:

1. *Open the laser water cooling line. Turn on the laser circuit brake. Turn on the laser.*
2. *Find the laser beam, according to the instructions from the TSI Inc. manual. Align fiberligh multicolor beam separator with the laser head.*
3. *Find the shifted and unshifted laser beams. Attached fiberoptic couplers.*
4. *Mount the transmitting probe to traverse system arm. Connect fiber optic cables from transmitting probe to the fiberoptic couplers. Adjust beam brightness and fine tune beams according to the instructions from the TSI Inc. manual.*
5. *Mount the receiver to traverse system arm parallel to transmitting probe arm.*

6. *Turn on the pump circuit brake. Turn on the pump. Adjust traverse system coordinates to place the laser beams measuring volume within the test section.*

7. *Find and focus measuring volume within the test section through the receiver (152.5° off axis from the transmitter for optimal results). Connect receiver fiber optic cables to the photo detector module. Connect photo detector module to signal processor. Connect signal processor to computer.*

8. *Adjust pump frequency to achieve the desired mass flow rate* $\dot{m}$.

9. *Run the Flowsizer LDV software. Move transmitting probe and receiver with the traverse system to desired starting position.*

10. *Start data acquisition. Export acquired data.*

11. *Turn off the laser and the pump after the desired collected data.*

12. *Apply corrections to data points to account for the planar-concave lens effects of the test section geometry.*

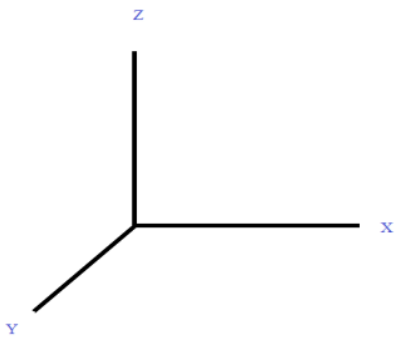

Figure 3.7 - Experiment Coordinate system

3.3 - Methodology

All the experiments were carried out in the same flow loop. The reservoir was filled with water at room temperature (21° C ~ 38° C) without seeding particles. The laser was operated at 1.5 W for all the experimental runs; the beam transmitter and receiver probes positions were recorded based on the traverse displayed position. Continuous data collection took place for process measurements (RTD temperature data and magnetic flow meter measurements). LDV data was collected in all cases over an interval of at least 60 seconds, and a maximum number of samples were pre-specified to between 6000 - 15000 for all the LDV profiles. Repeated measurements were performed for each blockage between 3 and 5 times on different days after test section disassembly and reassembly. The traverse system was operated by robotic positioning with an accuracy superior to 0.1 mm.

The first measurements were taken across the test section without an obstruction, by moving the traverse system in the Y^+ direction with increments of 0.44 mm, to acquire at least 15 measuring points across the diameter of the test section (the near wall locations were limited by the curvature of the inside walls, created a blind spot or unmeasurable area, details explained on appendix A). These measurements were taken at different axial locations; by moving the Z^+ axis of the traverse system. For unobstructed flows data was collected at 3 different locations along the test section corresponding to 25%, 50% and 75% of the test section length. For flows with obstructions 8 axial positions were examined downstream of the blockage. These measurements were taken with flow rates ($\dot{m}$) of 0.250, 0.500 and 0.750 kg/s; on 3 different dates, to ensure repeatability.

Each obstruction was placed at 25.4 mm in height (Z) within the test section, perpendicular or at 90° in relation to the transmitting probe, and held in place by three 50.8 × 12.7 × 12.7

Neodymium (N42) Rare Earth Magnets placed on the outside of the test section. The eight axial measurement locations were selected with more spatial resolution closest to the obstruction and then increasing with Streamwise direction. The first position measured was as close as possible given the measurement volume of the LDA system (about 51.7 mm from the entrance of the test section or ~ 1 mm from the trailing edge of the obstruction). Then three axial positions were measured with increments of D/2 or 5.56 mm, the two positions with increment of D or 11.11 mm, then an increment of 2D or 22.22 mm, and finally the last spacing was 5D or 55.55 mm increment. This spacing was selected in order to observe the near and far field effect of the obstructions. Table 8 illustrates the measurement locations and used terminology as a function of Z downstream of the obstruction.

Table 8 - Axial Measurement Locations (note the trailing edge of the obstruction is located at 50.8 mm)

Used terminology	With obs	½ D	D	1.5 D	2.5 D	3.5 D	5.5 D	10.5 D
Measurement location Z in mm	51.7	57.26	62.82	68.38	79.49	90.6	112.82	168.37

The Y increments for measurements across the test section at each measurement location were 0.44 mm except near locations were significant gradients in the velocity due to obstruction were present. For fine measurements near the obstructions 0.06 mm increments were used. In some experiments past y ~ 7.1 mm the software would either take too long (*i.e.* Over 30 minutes) to collect data, and the burst efficiency was below 20 % yielding less than 1000 samples; probably due to interference of wall material with the measurement volume and hence these values were discarded.

The temperature of the flow was continuously recorded for each measurement, and based on the temperature and mass flow rate, other parameters like the fluid density ρ, kinetic viscosity ν, dynamic viscosity μ and Reynold's number were calculated.

3.4 - Validation Study

In 1997, J. den Toonder and F. Nieuwstadt [22] performed experiments to investigate the influence of the Reynolds number on inner scaling in turbulent pipe flow for low to moderate Reynolds number. This study included the detailed measurements and hence was repeated with the facility and instrumentation in this thesis to demonstrate the validity of the equipment and test procedure. Both studies use tap water at room temperature without seeding particles as the working fluid and both test sections are geometrically identical, squared on the outside with a cylindrical pipe inside. While the physical dimensions and orientation are different the results are provided on a dimensionless basis and both are single phase and unheated so that directional effects are negligible. Both experiments provide detailed LDV data for each flow rate.

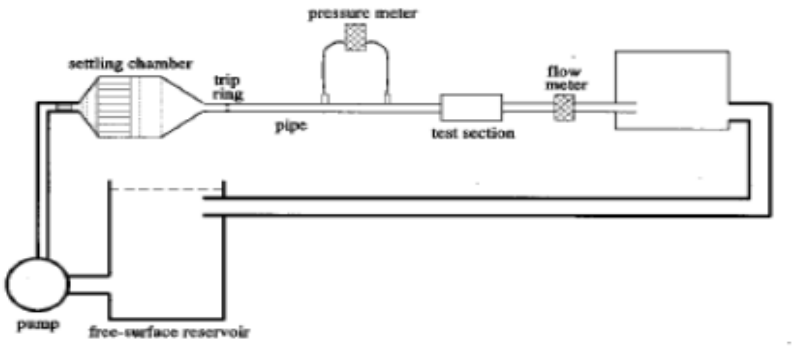

Figure 3.8 - Pipe flow facility schematic

Reference [22] provides profile measurements for four distinct Reynolds numbers: 4900, 10000, 17800 and 24600. While these are below the values tested in subsequent chapters they still cover a representative range of Reynolds number near those in this thesis. The experiments were carried out in a re-circulatory pipe flow loop facility of the laboratory for Aero and Hydrodynamics, a schematic diagram of which is shown in Figure 3.8. The loop consists of a cylindrical Perspex pipe with 34 m in length and 40 mm inner diameter, with a disk pump, a settling chamber, a trip ring device 1 m behind the pipe entrance to force the flow to transition to turbulent, two membrane differential-pressure transducers one before and one after the settling chamber to measure the pressure gradient across the pipe, a test section located 30 m downstream of the inlet pipe, a magnetic inductive flow meter, and a free surface reservoir with a thermocouple to measure the fluid temperature. The pipe wall in the test section was partially replaced by a thin foil made of Teflon FEP with a thickness of 190 μm, which makes the test section inner diameter 40.37 mm. the entire pipe flow section is contained within a square Perspex box filled with water to minimize the refraction of the laser beams. Figure 3.9 illustrates the test section.

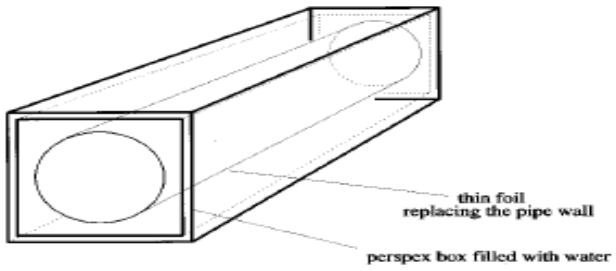

Figure 3.9 - Test section

The results for the velocity profiles were normalized by:

$$U^+ = f(y^+) \tag{3.8}$$

where $U^+ = U/\mu_\tau$ is the scaled mean velocity and $y^+ = y\mu_\tau/v$ is the dimensionless distance to the wall. The *f* is a universal function presumably independent of Reynolds number and generally known as ‘‘the law of the wall.’’ The friction velocity was determined from the pressure measurements according to

$$\mu_\tau = \sqrt{\frac{D}{4\rho}\left|\frac{\Delta P}{\Delta z}\right|} \tag{3.9}$$

Where *D* is the diameter of the pipe, Δ*P* is the measured pressure difference and Δ*z* is the distance over which Δ*P* is measured. The viscosity and fluid density are obtained using the temperature. Figure 3.10 illustrates the mean velocity profiles at the different Re.

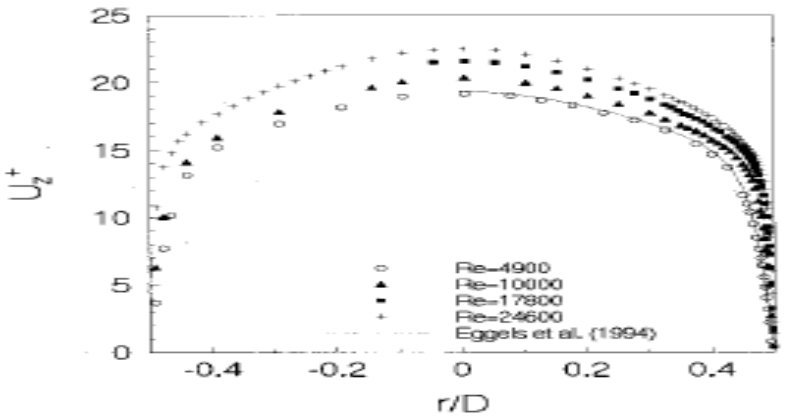

Figure 3.10 - Mean velocity profiles normalized by the friction velocity

To validate the constructed test section for the present study, test where carried at the same set of Reynold numbers, multiple times, at 3 different dates to ensure repeatability. Since the loop used for the study did not possess pressure transducers, the friction velocity μ_τ could not be taken into account. Figure 3.11

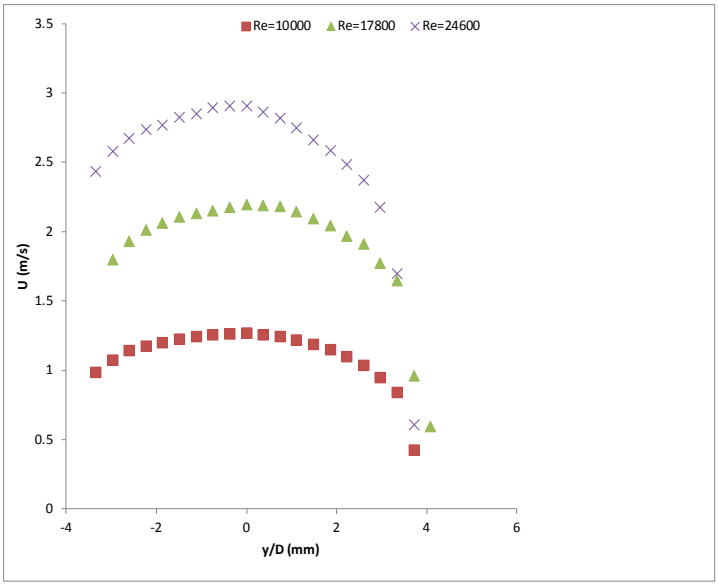

Figure 3.11 - Mean velocity profiles

So the data sets where normalized by the correspondent bulk velocities Ub (0.41, 0.84, 1.5, and 2.07 m/s). as depicted in Figure 3.12, when comparing both graphs side by side ignoring the different normalization factors used, the results from the validation trial are in reasonable agreement with the results from J. den Toonder and F. Nieuwstadt [22]; except for a minor difference on the data set for Reynolds 4900, due to a small imperfection on the test section.

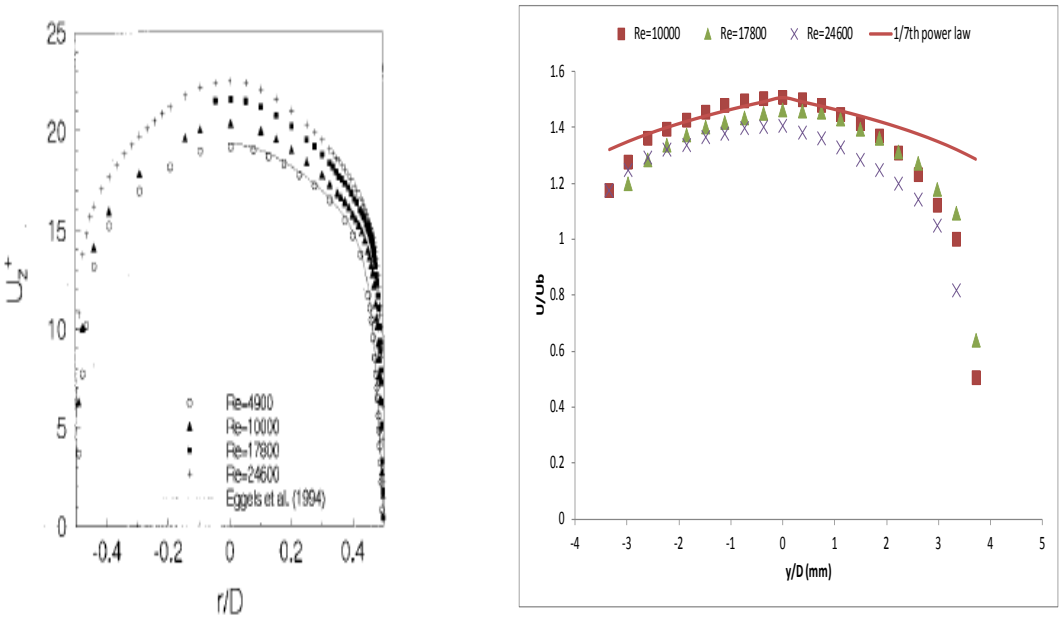

Figure 3.12 - Side by side mean profiles comparison

4. Results and Analysis

This chapter describes the results of the measurements taken at eight different axial locations downstream of the flow-obstructions for mass flow rates of 0.250, 0.500, and 0.750 kg/s. LDV results in terms of radial profiles of the mean velocities and root-mean-square fluctuations of the streamwise and azimuthal velocity components are presented for each obstruction and flow rate. The effects of each obstruction on the velocity profiles are analyzed and compared to the velocity profiles without obstructions. The effects of height variation of the obstructions on the turbulence intensities are also analyzed and compared to the unobstructed flow statistics of the flow. The locations downstream of the obstruction in the profiles in this section are expressed normalized to the unobstructed diameter D. Also note that the measuring volume of the laser beams limits the measurements to values greater than 0.9 mm after the obstruction so on the graphs the terminology "with obs" represents the first possible measure location right after (0.9 mm) the obstruction. Consult Table 8 for the exact measurement locations as a function of Z.

4.1 - Flow characterization without obstructions

Two component LDV measurements were performed in the flow loop at Reynolds number of 30700 (0.250 kg/s), 61400 (0.500 kg/s) and 99000 (0.750 kg/s) based on the average bulk velocity and inner tube diameter. The streamwise (axial) and azimuthal (angular) velocity profiles *U(y, z)* and *V(y, z)*, respectively, were measured across the diameter of the pipe at different radial positions (y), and different z locations downstream of the obstruction; as well as their respective turbulence intensity profiles *Tu*, defined as:

$$Tu = \frac{U_{rms}}{U} or \frac{V_{rms}}{V} \tag{4.1}$$

Note that the azimuthal turbulence intensity profiles were also measured, but the results are difficult to interpret since the proprietary software uses the above formula to calculate turbulence intensities and the normalizing azimuthal velocity is approaching zero which causes unphysically large intensities, so their illustration became impractical.

In the figures presented in this section, the mean values and rms fluctuations of the streamwise and azimuthal velocity components are normalized by the respective average flow velocity U_b = 2.58, 5.17, 7.76 m/s respectively. The radial position is represented by y.

Recall that turbulent flow in a pipe consists of three regions, characterized by the distance from the wall. The first and closest to the wall is the viscous layer; it is very thin, and the velocity profile is nearly linear, since there is a lack of eddies for turbulent mixing the turbulent stresses are damped. Next to the viscous layer is the buffer layer; which is larger than the viscous layer and both viscous and shear stresses are important, since turbulent effects become significant, but the flow is still influenced by viscous effects. Above that is the turbulent layer; this is the largest layer and turbulent effects dominate over viscous effects.

The turbulent velocity profiles for the unobstructed flow of the three Reynolds numbers are typical, with a sharp velocity gradient near the wall. The distribution near the wall became steeper with increase in Reynolds number (see Figures 4.1, 4.2) while the turbulent core becomes more uniform. As depicted in Figures 4.3-4.4, the time-variable components of the streamwise velocity or the streamwise velocity root mean square Urms have typical profiles as well; the peak value and the position of the peak value are approximately the same for all 3 Reynold numbers (approximate peak 0.12 between 6.5 - 8.8 mm). The streamwise turbulence intensity profiles *Tu* are also typical of turbulent flows, their shapes are very similar to the correspondent streamwise variable component profiles, averaging between 7.4 - 8.3 % for the different Reynold numbers.

The lowest values of the turbulence intensity are at the center line of the pipe (between 4.90 - 5.33 mm), the highest values for the intensity are at the outer edge of the buffer layer, followed by a drop near of the wall (Figure 4.5).

As expected, the measured azimuthal velocity profiles V are essentially zero in the core of the flow away from the walls, reaching the maximum value very close to the wall (see Figures 4.6, 4.7). The variable components of the azimuthal velocity remain constant in the core and increase near the wall, reaching a peak value in close proximity to the wall, the distributions show a certain dependence on Reynold numbers as expected, with increasing Re the peak value becomes larger and situated further from the wall, as depicted in Figures 4.8-4.9.

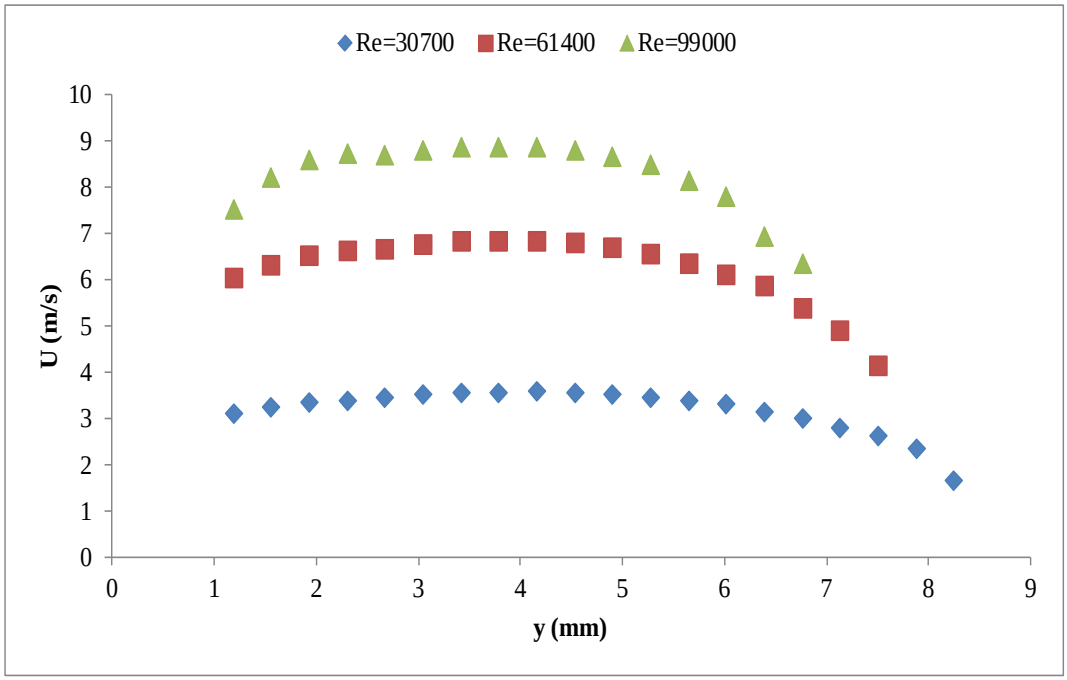

Figure 4.1 - Streamwise mean velocity profiles without obstructions

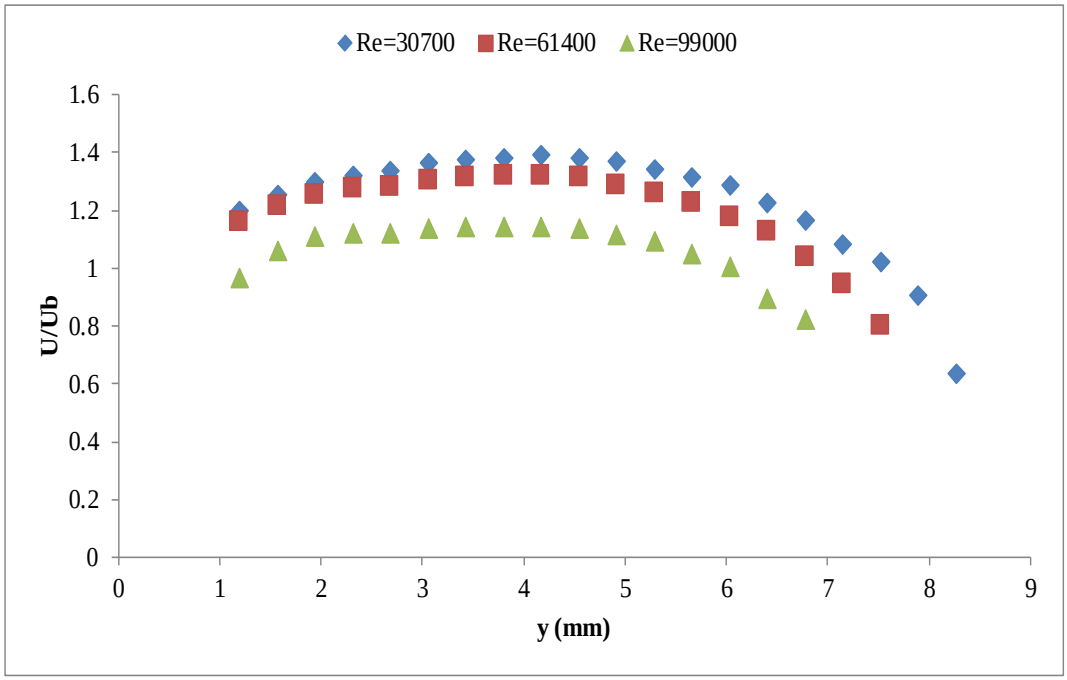

Figure 4.2 - Normalized streamwise velocity profiles without obstructions

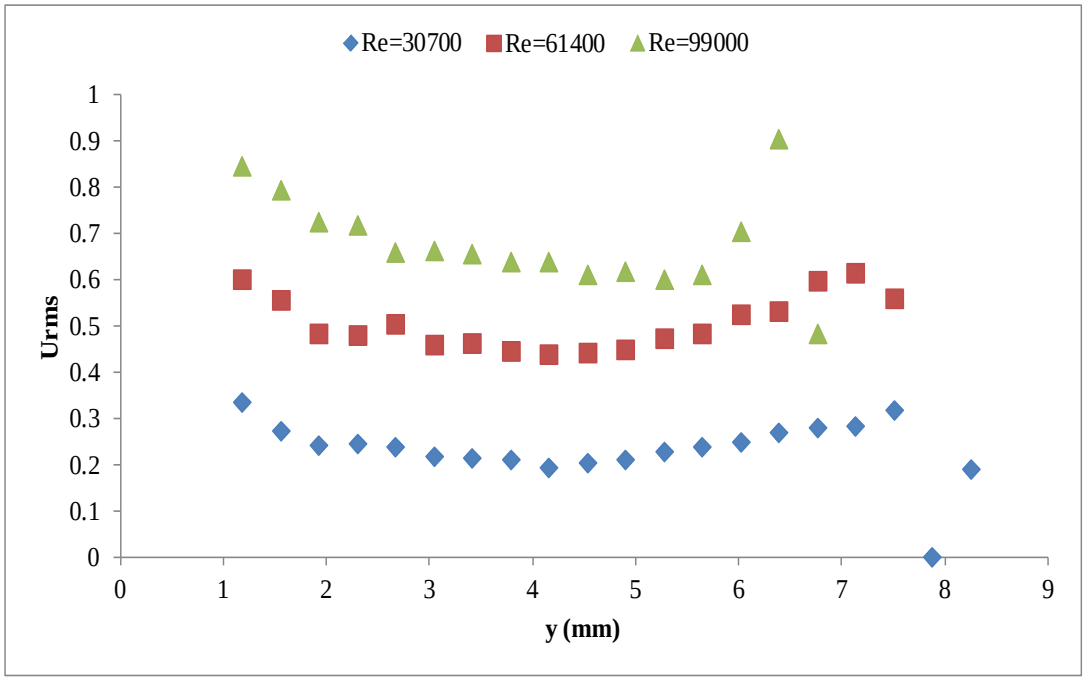

Figure 4.3 - Streamwise rms velocity profiles without obstructions

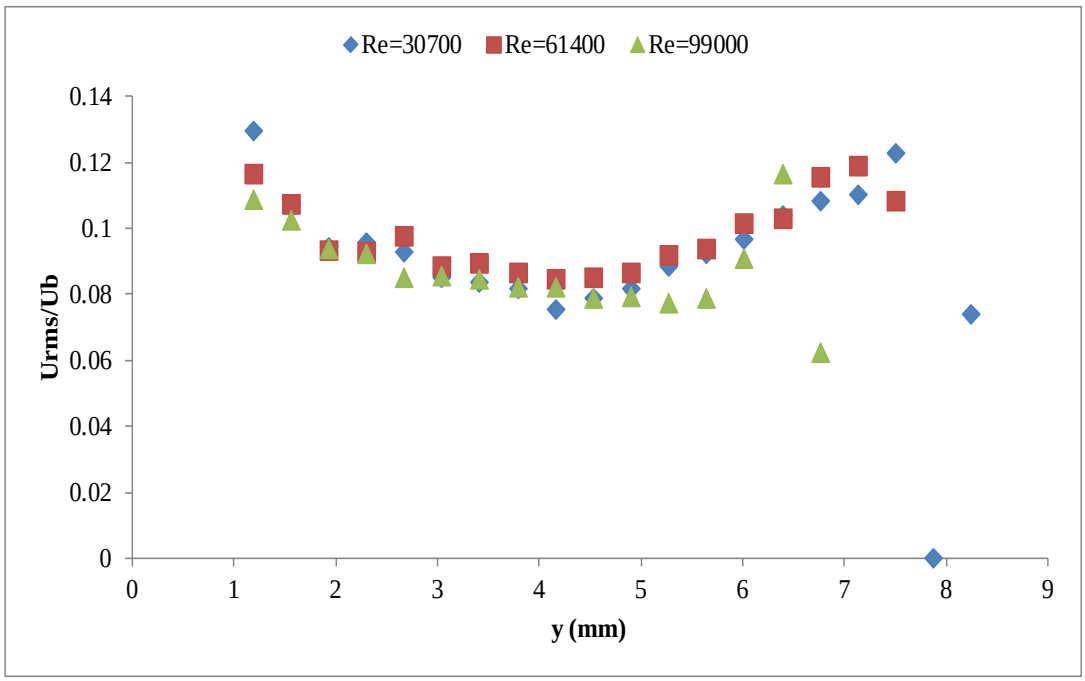

Figure 4.4 - Normalized streamwise rms velocity profiles without obstructions

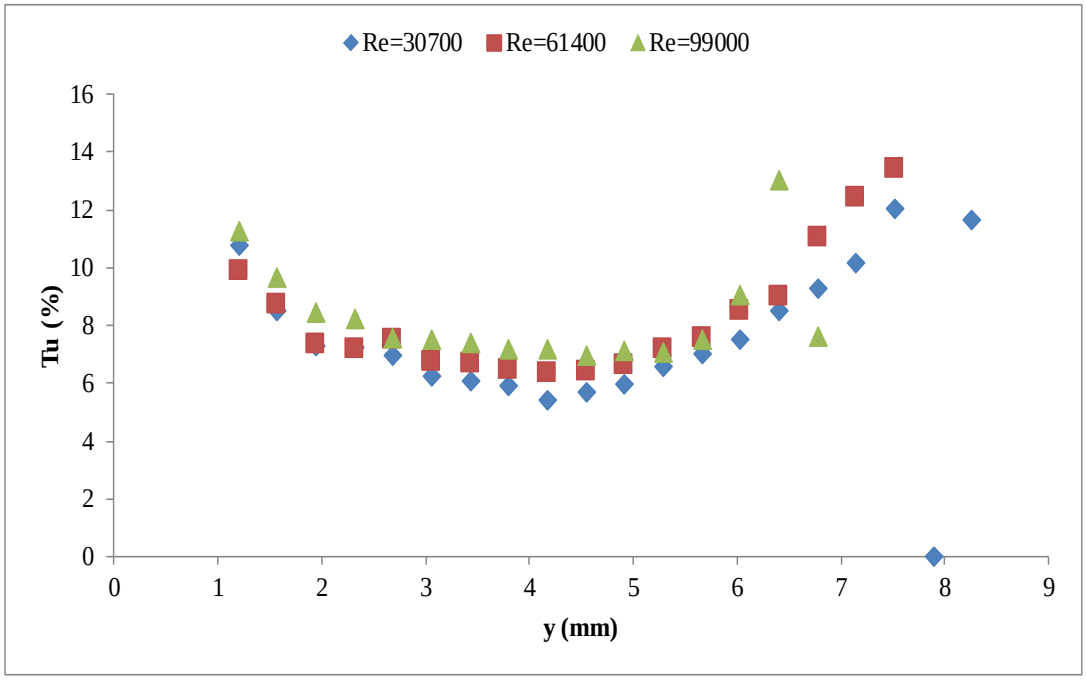

Figure 4.5 - Streamwise turbulence intensity profiles without obstructions

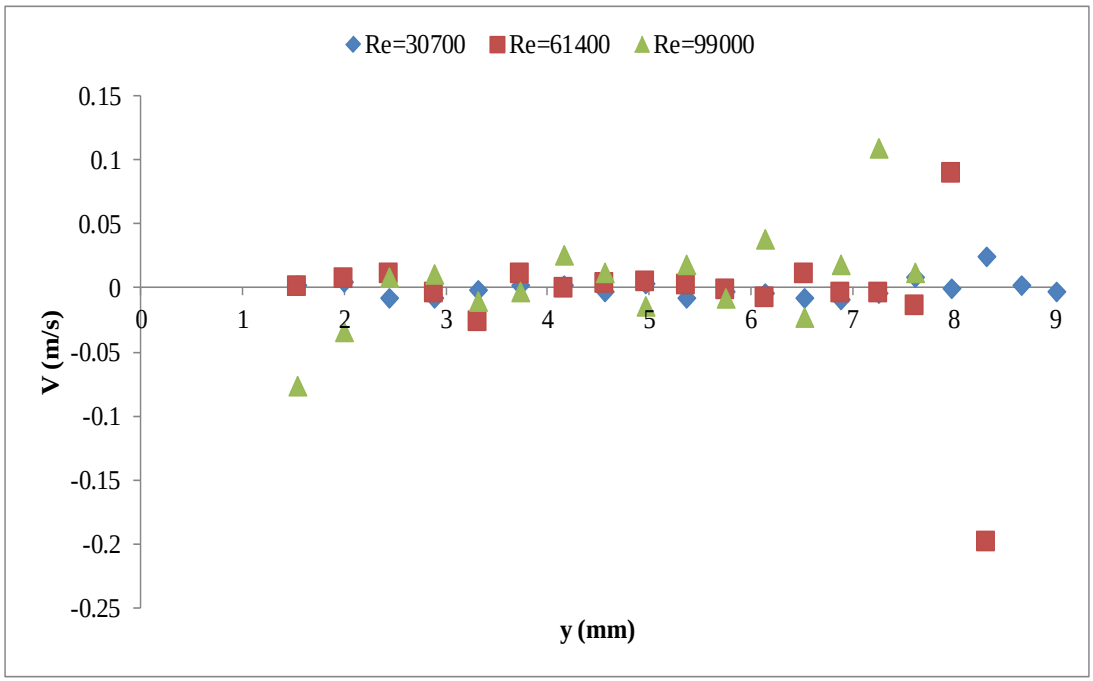

Figure 4.6 - Azimuthal mean velocity profiles without obstructions

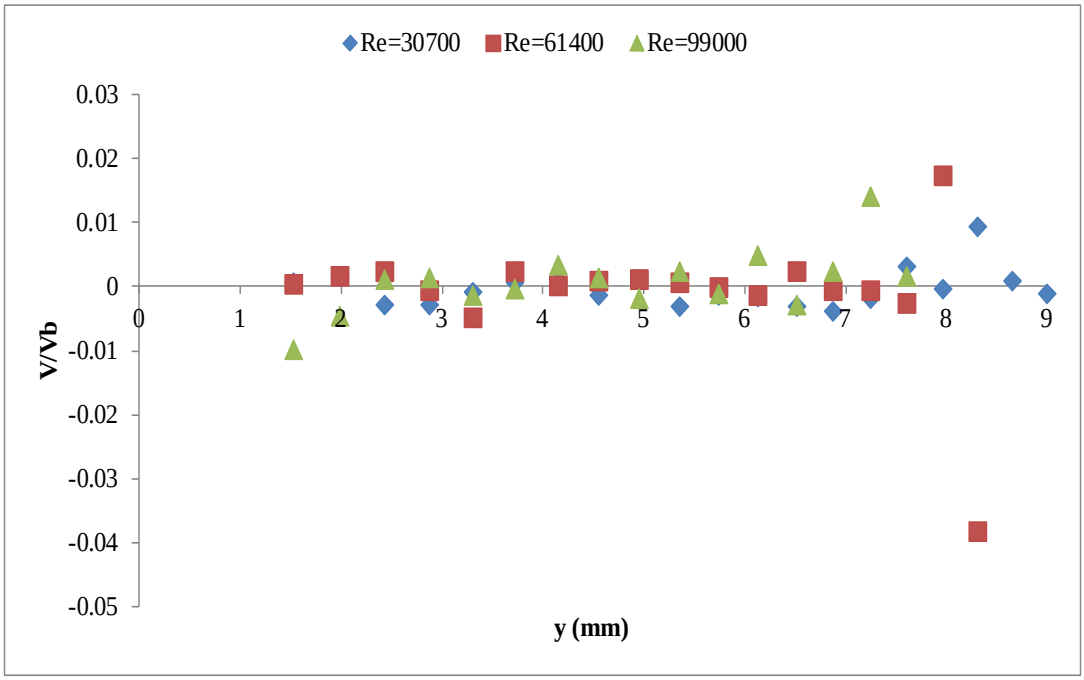

Figure 4.7 - Normalized azimuthal velocity profiles without obstructions

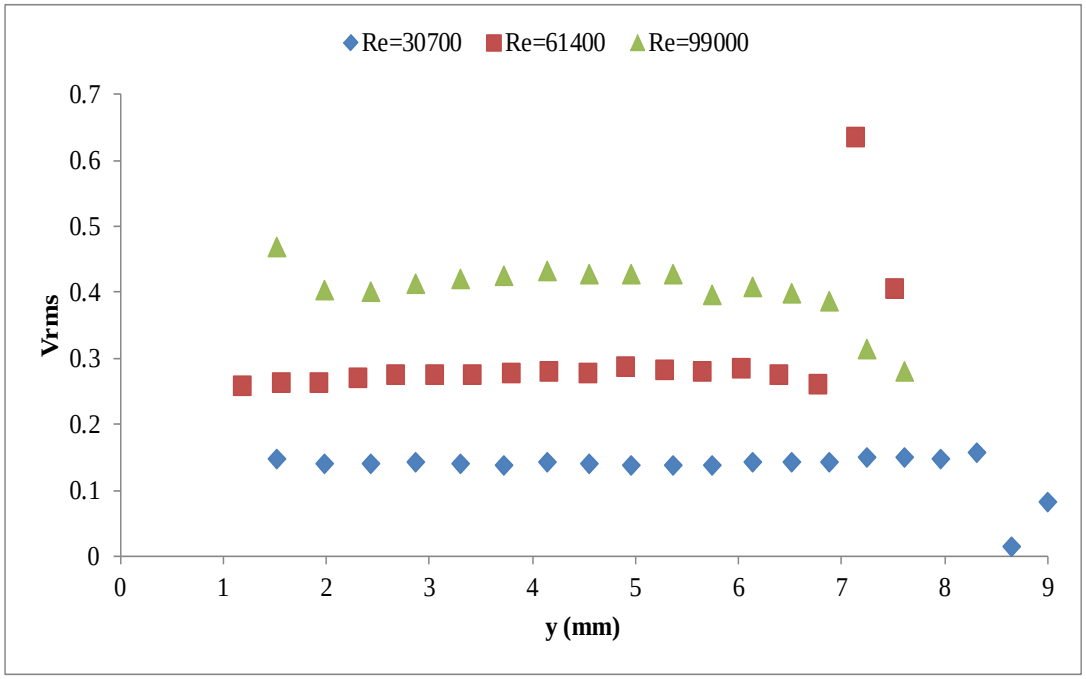

Figure 4.8 - Azimuthal rms velocity profiles without obstructions

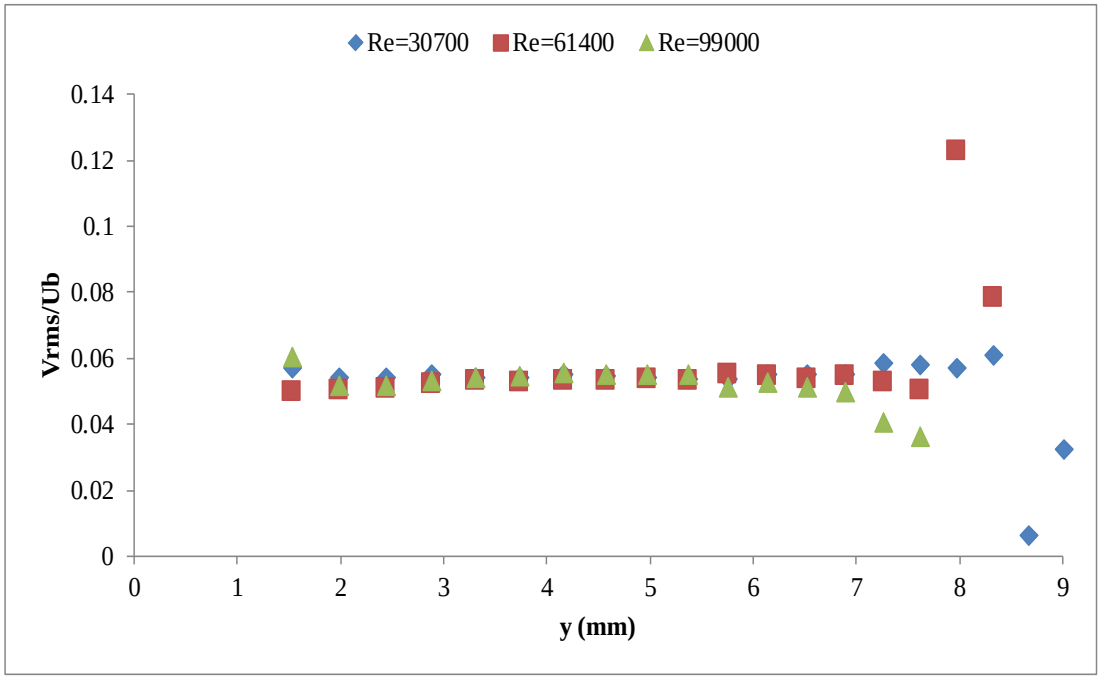

Figure 4.9 - Normalized azimuthal rms velocity profiles without obstructions

4.2 - 40% Blockage Measurements

The first obstruction represents 41.19 % area blockage. The obstruction caused a significant deviation in the streamwise mean velocity profiles (see Figure 4.10, 4.11). For a Reynolds number of 30700 the streamwise velocity decreased immediately downstream of the obstruction and negative values (from 6.74 to 8.25 mm) were observed in its wake (indicating regions of recirculation). The recirculation zone near the wall persisted through 1 D (11.12 mm) downstream of the obstruction. At 1.5 D the flow profile remains perturbed but the recirculation zone is no longer present. At 2.5 D the velocity profile becomes similar to the fully developed profile so that the zone of reversed streamwise flow or recirculating flow zone lasted for 1-1.5 D (11.12 - 16.68 mm). The profiles of the RMS streamwise velocity were also perturbed significantly (see Figures 4.12, 4.13) for distances up to 2.5 D (27.8 mm) along the channel. About 1.37 mm from the center of the tube, between the obstruction tip and mid height. The RMS velocity components peak at a

radial location approximately in mid-plane of the obstruction (half way up its height). At 3.5 D (38.92 mm) the U_{rms} profiles show semblance to the unobstructed pattern. With the obstruction the turbulence intensity increased tenfold at the obstruction radial location (see figure 4.14) with a change in the average intensity from 7.44 to 70.7 at 0.5 D (see Figure 4.15). After 2.5 D, the streamwise turbulence intensity profile was restored to unobstructed levels.

For Reynolds number of 30700, the azimuthal velocity profiles were also significantly affected by the obstruction ranging from -2.5 m/s to 2.8 m/s at a radial location corresponding to the mid-plane of the obstruction and finally it decreased when approaching the buffer/viscous sublayer (see figure 4.16, 4.17). This effect lasted for 1.5 D downstream of the obstruction and at 2.5 D the azimuthal velocity profiles return to near zero levels similar to that for unobstructed flow. The fluctuating components of the azimuthal velocity V_{rms} nearly quadrupled and then decreased with distance from the obstruction (see figure 4.18, 4.19). After 2.5 D the azimuthal velocity rms profile also returns to unobstructed levels.

At higher flows corresponding to a Reynolds number of 61400 the obstruction causes the streamwise velocity profiles to still experience a steep flow velocity reduction (see Figure 4.10, 4.11) at the radial location of the obstruction. However, in this case the recirculation zone was not observed possibly because such regions may be restricted to regions inaccessible to the LDV measurement volume at higher flow rates. Moreover, in general the velocity profile and turbulence characteristics caused by the obstruction persist much further downstream. The results shown in Figures 4.10 and 4.11 depicts that the profiles return to unobstructed values after approximately 10.5 D. Similarly, the streamwise velocity rms components experience a decrease at the trailing edge of the obstruction and then a rapid increase doubling their mean value and reach a local maximum value at around 7.2 mm (see Figures 4.12, 4.13). At these intermediate

Reynolds numbers, the gradient in U_{rms} are not as severe as those at lower flow rates, but the effects of the obstruction last longer, up to about 5.5 D downstream of the obstruction. The average streamwise turbulence intensity showed a modest increase from 8 % without obstruction to about 14 % with the obstruction at 2.5 D (see Figures 4.14, 4.15). The turbulence intensity while approaching the unobstructed case did not return to 8% within the measured domain. However given the repeatability of turbulence intensity is on the order of 2%, it can be assumed that the Tu intensity returned to fully developed levels at approximately 10.5D.

The azimuthal mean velocity profiles showed stronger effects from the obstruction as compared to the lower Reynolds number case (see Figures 4.16, 4.17). The velocities varied from -0.5 to 0.5 m/s at the radial location of the obstruction and lasted for 2.5 D downstream. The fluctuating components of the azimuthal velocity V_{rms} had a similar increase in value on the obstruction radial location as in the previous Re, from 0.05 to 0.23 (see Figures 4.18, 4.19). Similar to the streamwise behavior, the RMS behavior persisted up to 5.5 D downstream of the obstruction.

At the highest flow rate corresponding to a Reynolds number of 99000 the effect of the obstruction is evident in the streamwise velocity profiles, however no recirculation zone was observed and the effects of the obstruction are limited to a small region of the cross section (see Figures 4.10, 4.11). There is decrease in the streamwise velocities at the radial location of the obstruction, but no recirculation zone is observed. At 3.5 D the streamwise velocity profile reverts to a typical turbulent streamwise velocity profile. The U_{rms} profiles undergo a slight increase in the middle of the obstruction for about 1 D after the obstruction (see Figures 4.12, 4.13). The effect of the obstruction on the streamwise turbulence intensity at this flow rate seems to be small, since the turbulence fluctuated around 1 % increase after the obstruction (see Figures 4.14, 4.15). While the streamwise measurements do not clearly indicate the length required for turbulence to decay, the following azimuthal measurements provide further insight.

The azimuthal velocity profiles showed large distortions over the entire length (see Figures 4.16, 4.17) and the values fluctuated between -1 to 1.5 m/s. The fluctuating components of the azimuthal velocity also show a significant increase near the centerline, from 0.05 up to 0.40 for the entire 10.5 D axial measurement length (see Figures 4.18, 4.19). This indicates that the turbulence generated by the obstruction persists beyond the 10.5 D available measurement length.

The general trend is that the effect of the obstruction on turbulence generated seems to reduce as a function of Reynolds number, but that the turbulence persisted for longer lengths. For the smallest obstruction the turbulence observed seems isotropic with no significant systematic spatial distortion.

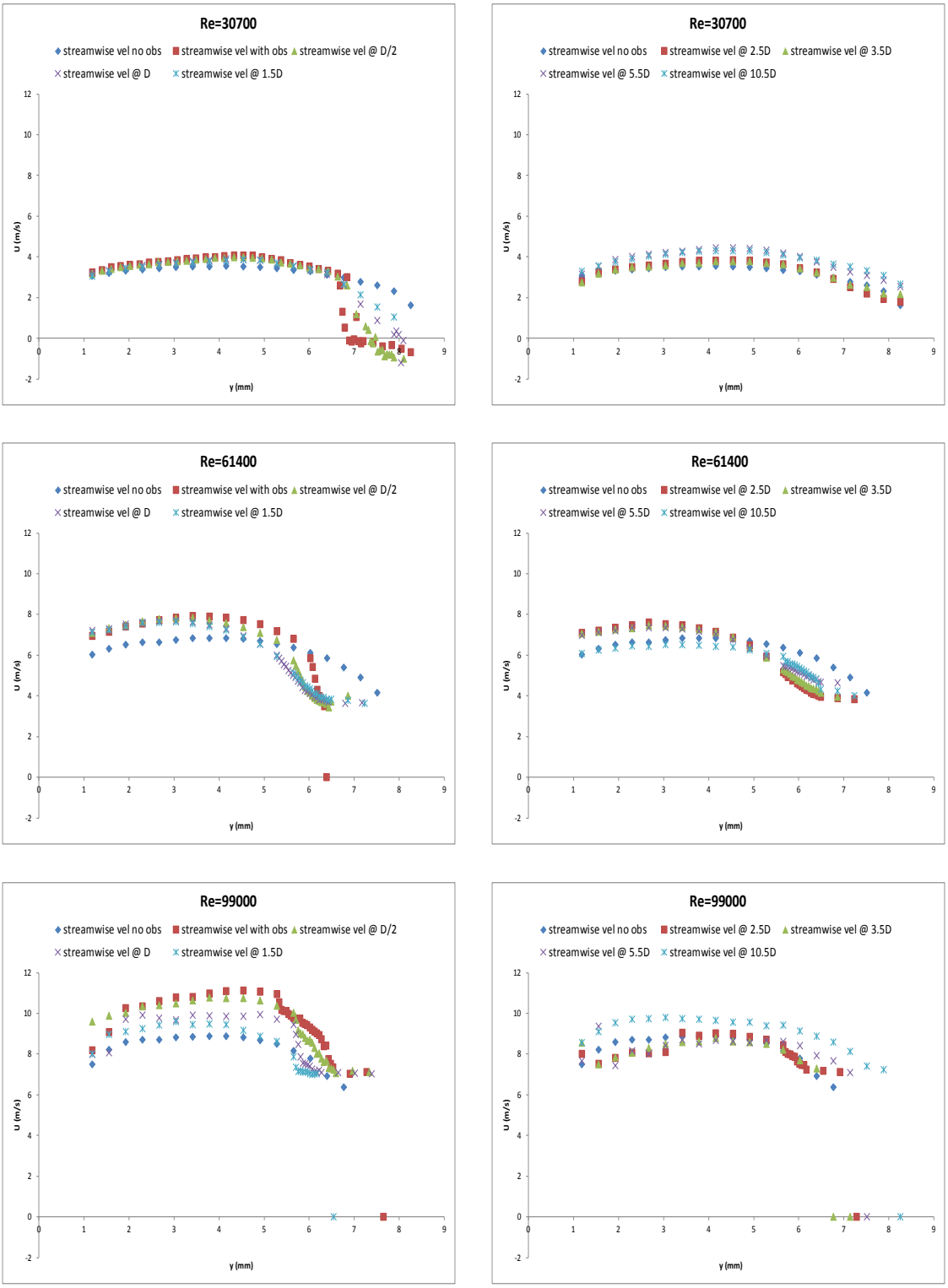

Figure 4.10 - Streamwise mean velocity profiles 1st obstruction

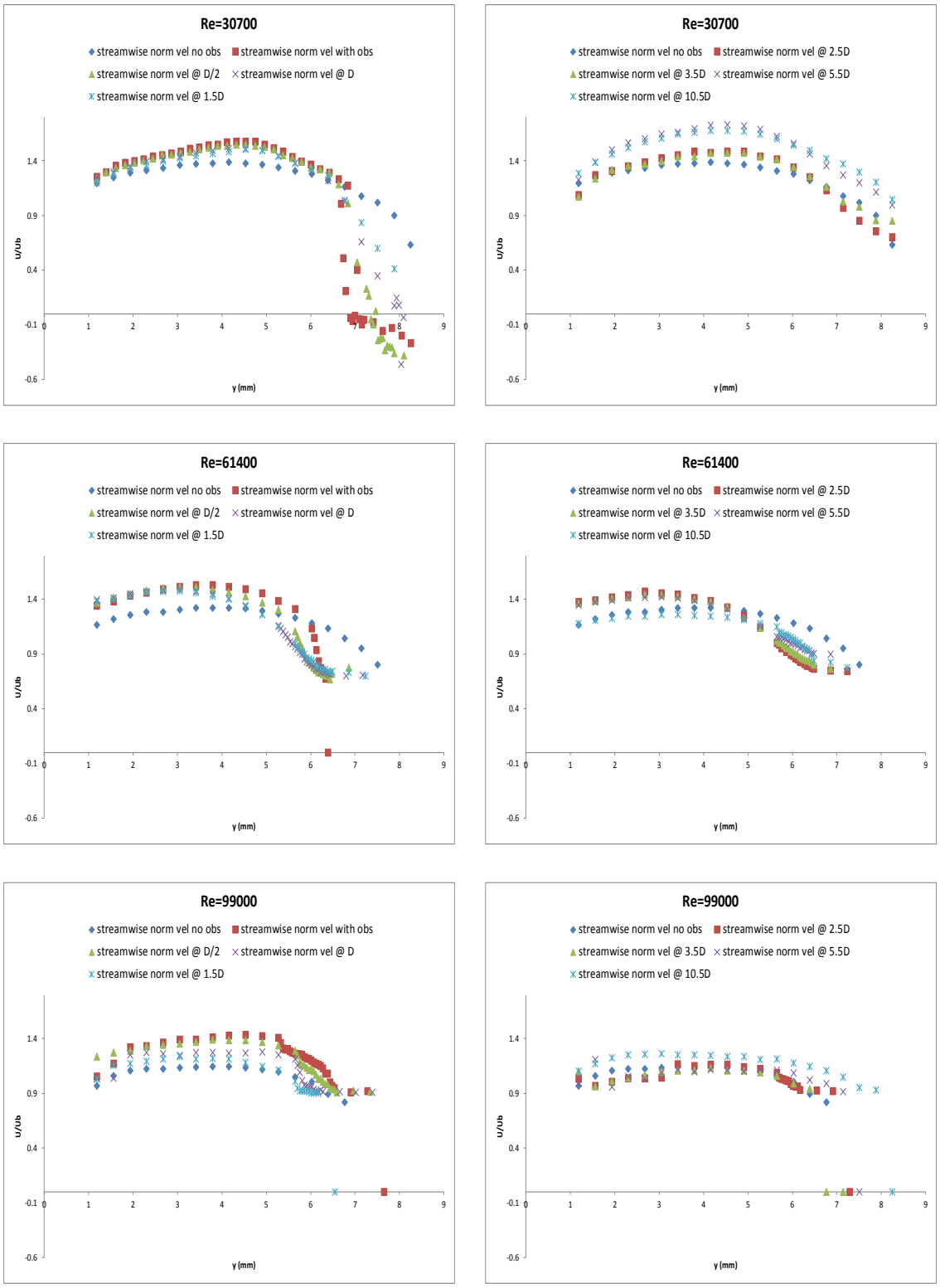

Figure 4.11 - Normalized streamwise velocity profiles 1st obstruction

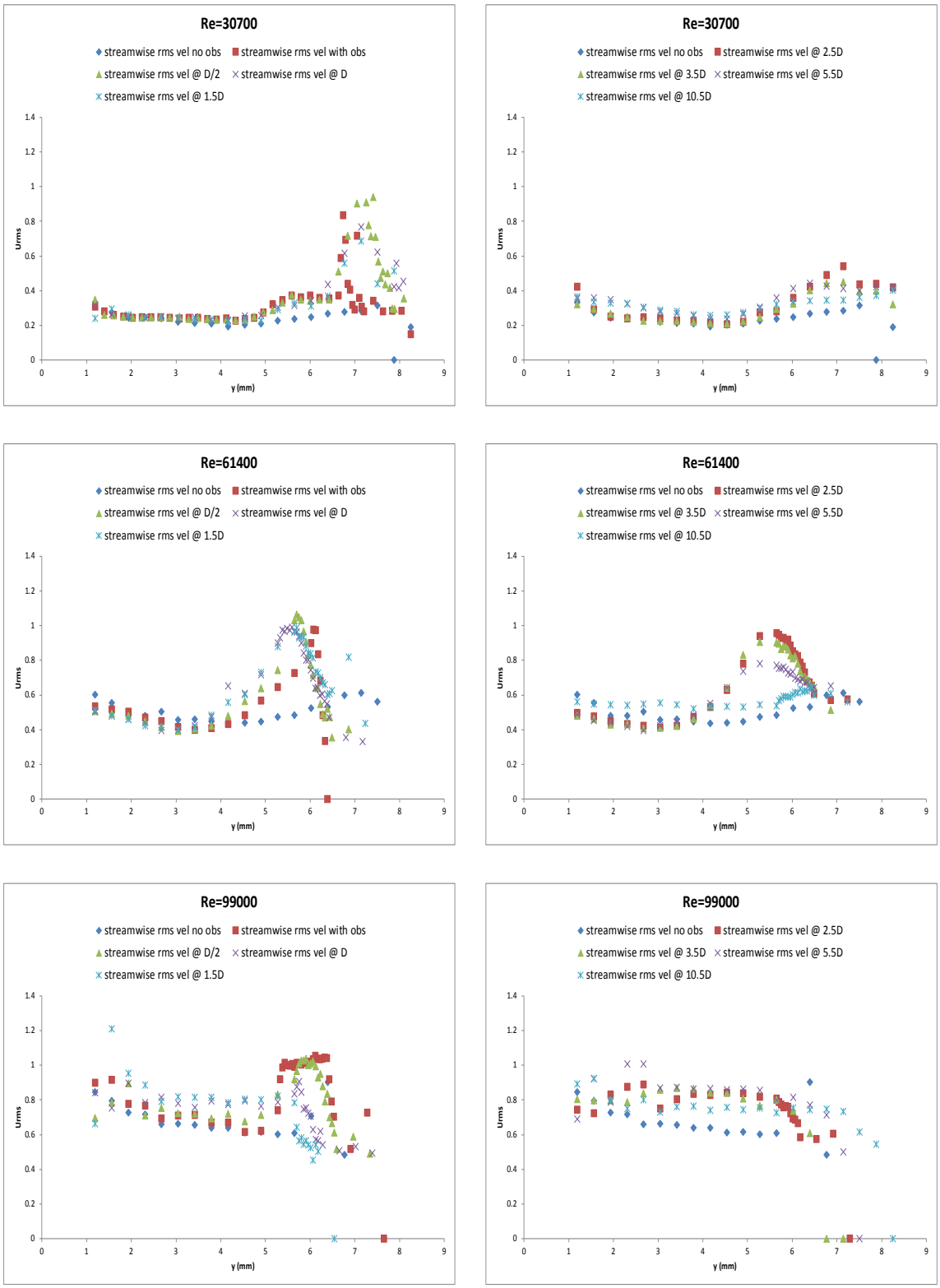

Figure 4.12 - Streamwise rms velocity profiles 1st obstruction

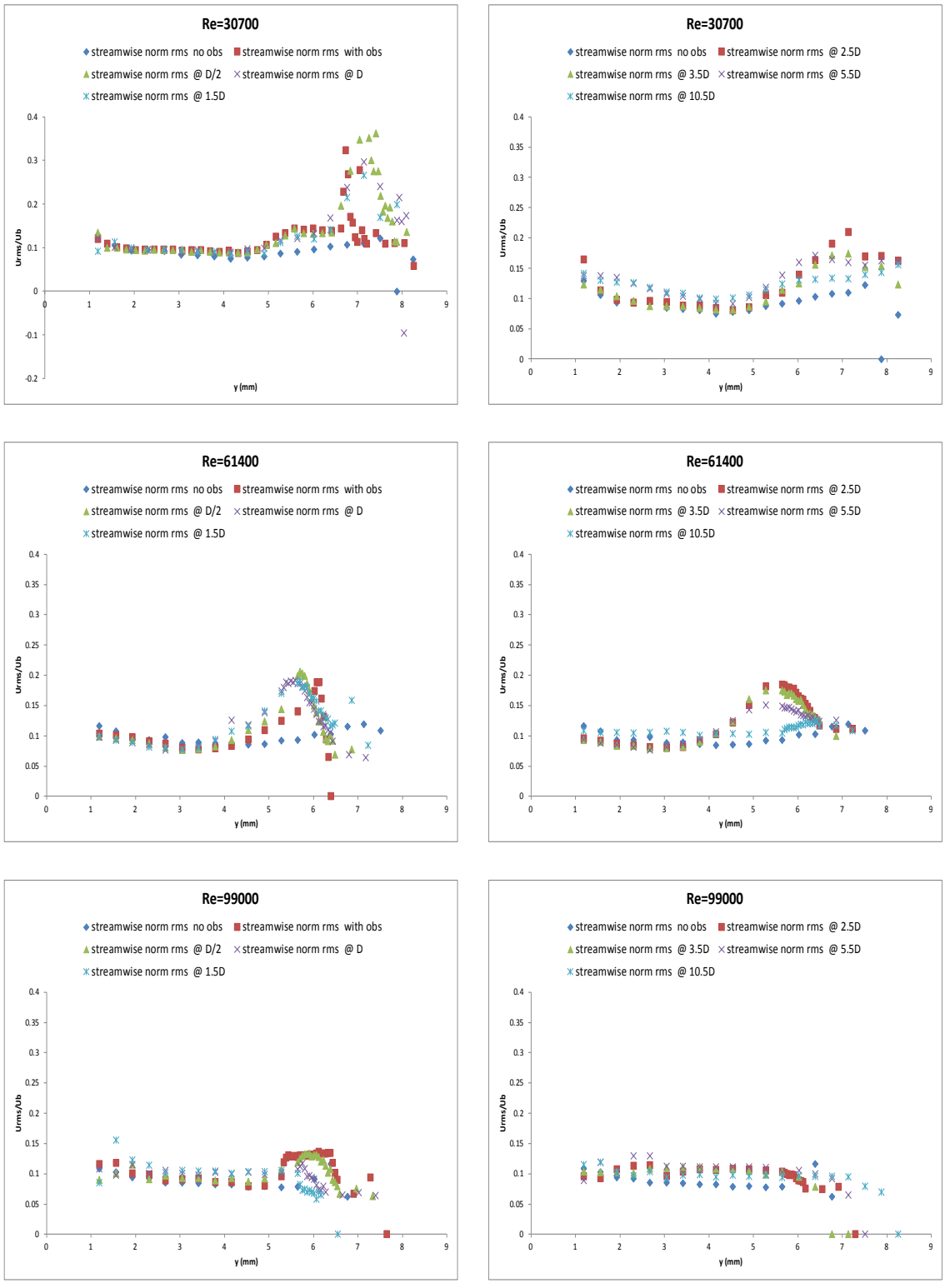

Figure 4.13 - Normalized streamwise rms velocity profiles 1st obstruction

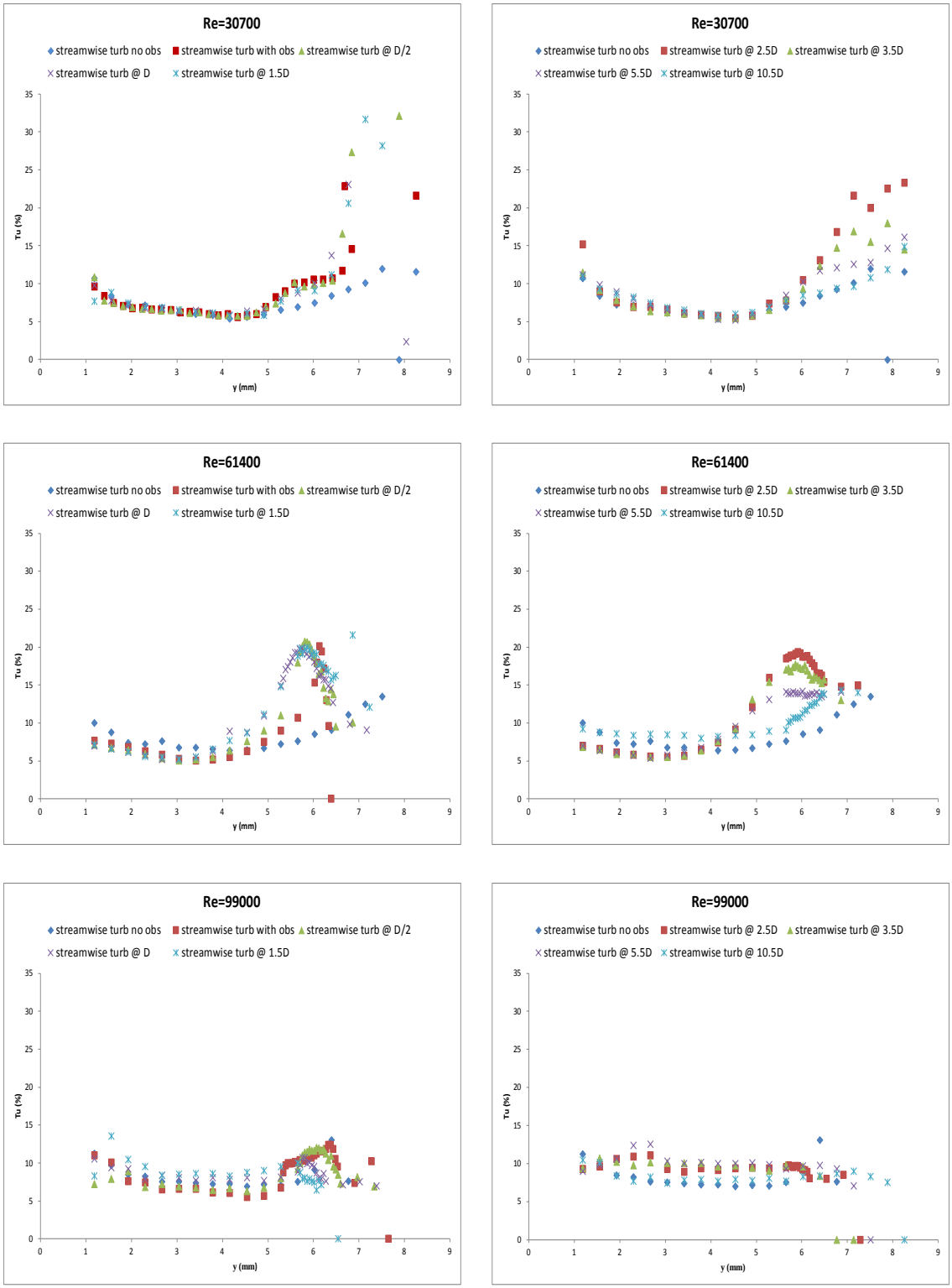

Figure 4.14 - Streamwise turbulence intensity profiles 1st obstruction

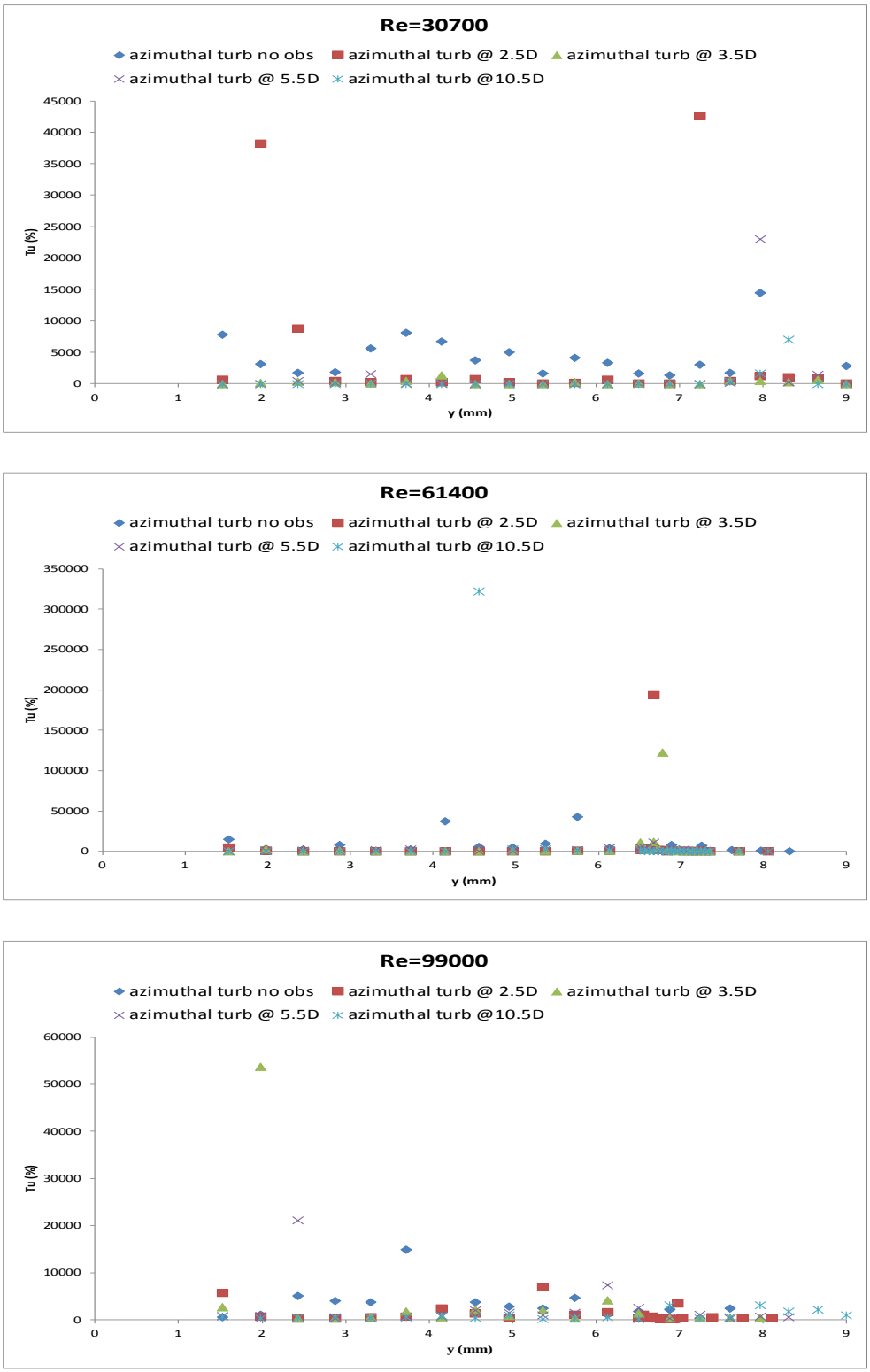

Figure 4.15 - Average &mean streamwise turbulence profiles 1st obstruction

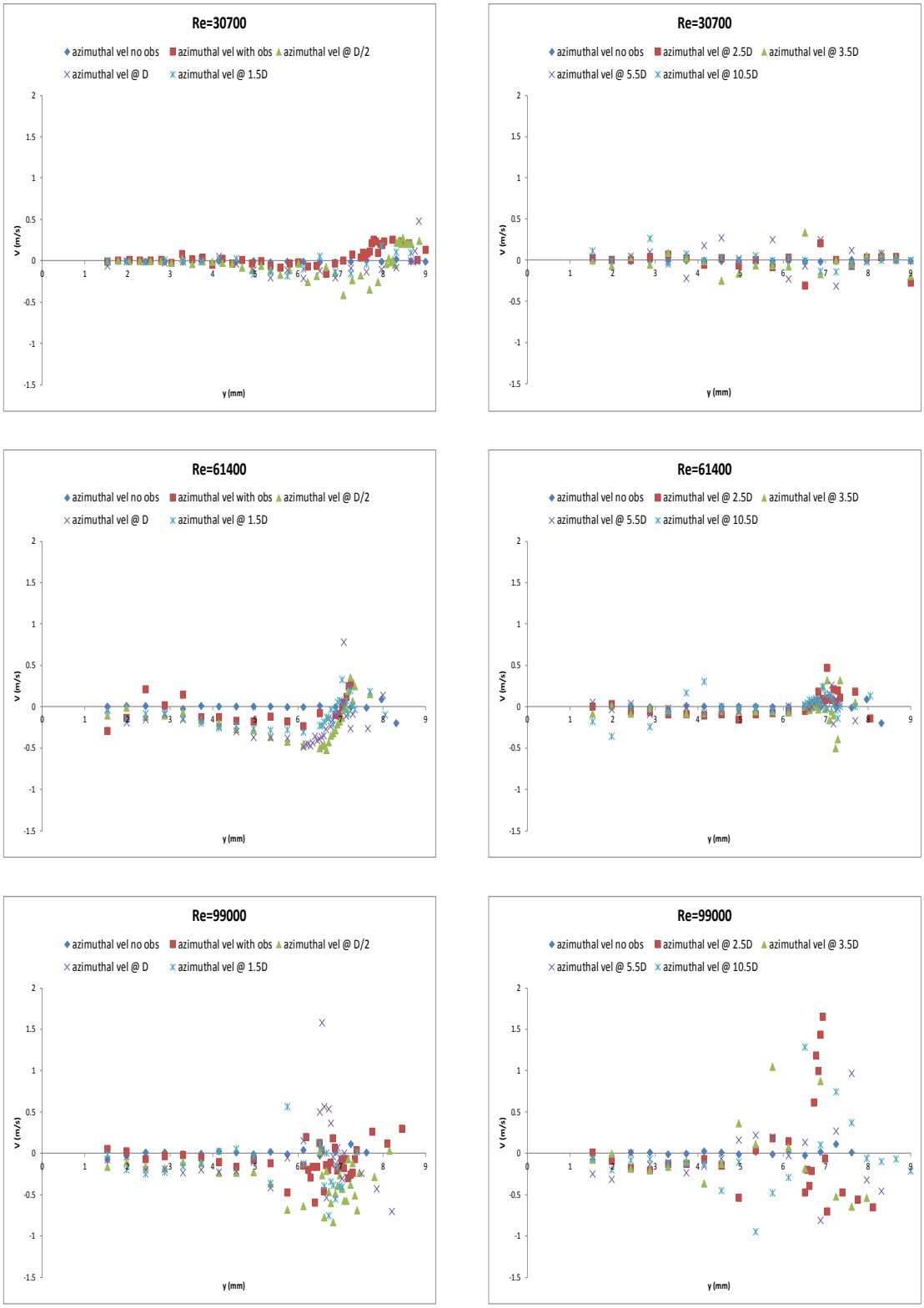

Figure 4.16 - Azimuthal mean velocity profiles 1st obstruction

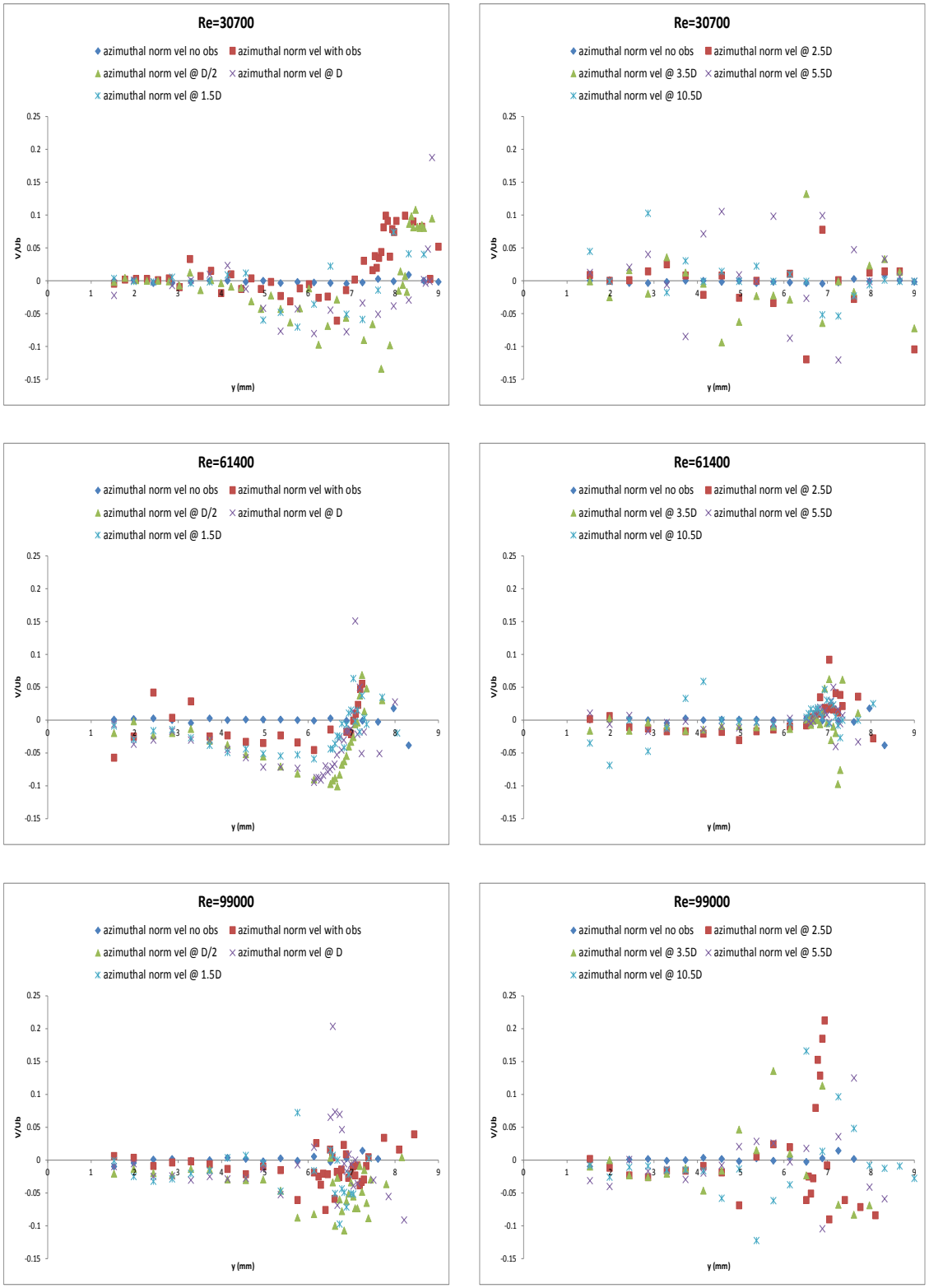

Figure 4.17 - Normalized azimuthal velocity profiles 1st obstruction

Figure 4.18 - Azimuthal rms velocity profiles 1st obstruction

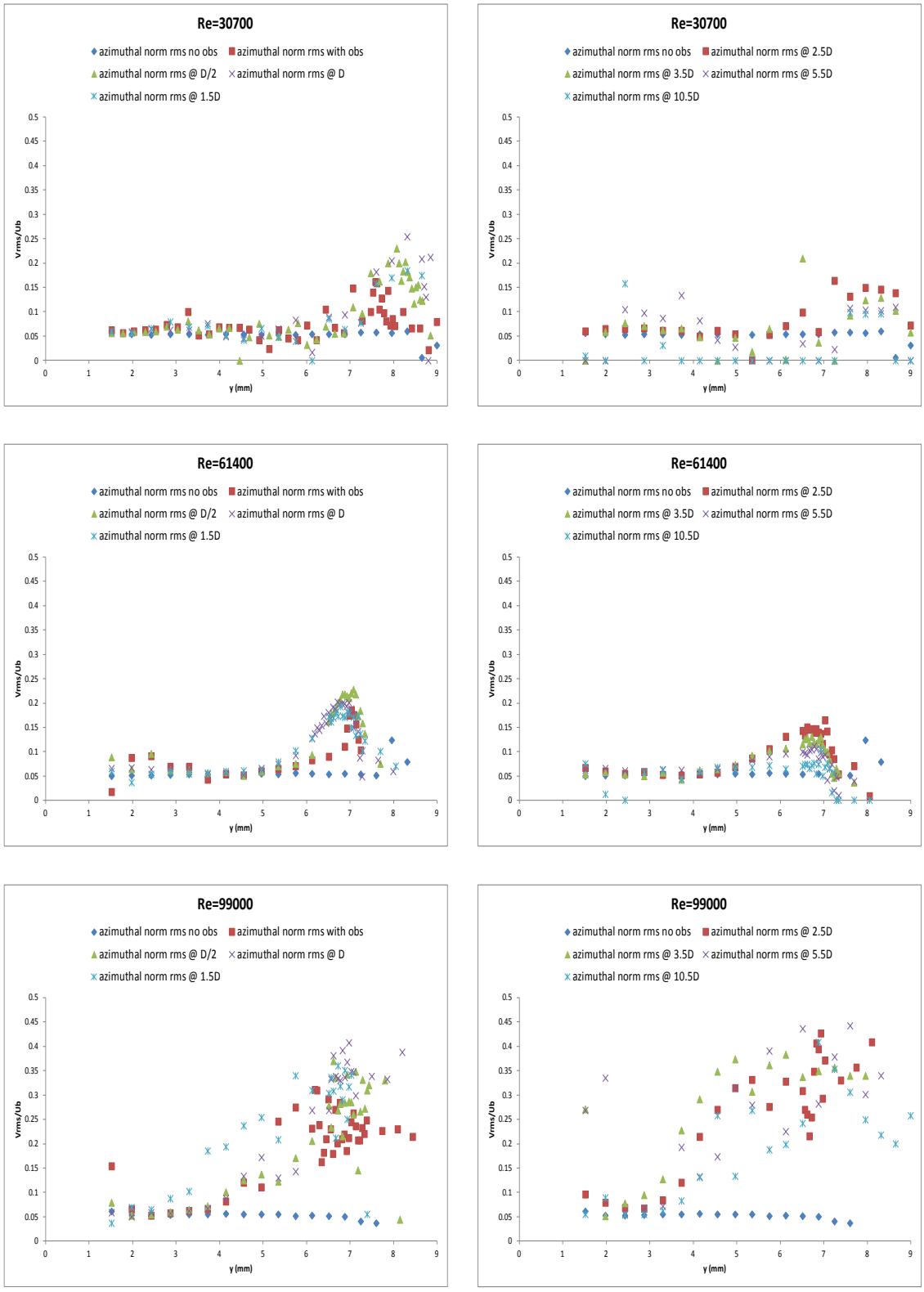

Figure 4.19 - Normalized azimuthal rms velocity profiles 1st obstruction

4.3 - 50% Blockage Measurements

The second obstruction represents a 51.83 % flow area blockage. At a Reynolds number of 30700, the streamwise velocity profiles clearly demonstrate the impact of the obstruction and reverse flow or negative velocities are observed in its wake (see Figures 4.20, 4.21). These negative velocities prevail up to 1.5 D downstream of the obstruction, and the deformity on the streamwise velocity profiles is observed up to 5.5 D downstream of the obstruction. Even at 10.5 D the streamwise velocity profile remains altered and hence the effects of the obstruction last beyond 10.5D. In essence, the overall behavior resembled the smaller obstruction as Figures 4.20 - 4.25 depict.

In the azimuthal direction the effect is largest at the obstruction mid-plane and then decreases with distance (see Figures 4.26, 4.27). However, the effects of the obstruction seem to last the entire 10.5 D downstream of the obstruction. The fluctuating components of the azimuthal velocity also show changes over the entire measurement length (see Figures 4.28, 4.29).

At higher flows corresponding to a Reynolds number of 61400, the local streamwise velocities decrease below zero up to 1 D downstream of the obstruction (see Figures 4.20, 4.21) at the radial location corresponding to the obstruction height similar to the lower velocity cases. Local negative velocities are still observed up to 3.5 D downstream of the obstruction which indicates the presence of a recirculating flow zone. After 5.5 D downstream of the obstruction the stream velocity profile reverts to a typical turbulent velocity profile. The fluctuating components of the velocity rapidly increase at the radial location of the obstruction for distances less than 1.5 D from the obstruction (see Figures 4.22, 4.23). beyond 1.5 D the fluctuating components decrease with distance from the obstruction. The streamwise turbulence intensity increase from 8 % to 360 %

right after the obstruction (see Figures 4.24, 4.25) then it gradually decreases, remaining above 20 % of intensity along the 10.5 D downstream of the obstruction.

In the azimuthal direction, the velocity profiles increase and reach a maximum value at the middle of the obstruction as observed at ½ D after the obstruction (see Figures 4.26, 4.27). However between 1and 1.5 D, the local velocities become negative, and gradually increase back to near zero. Between 2.5 to 10.5 D downstream of the obstruction the azimuthal velocities range between -1 and 0.5. The fluctuating components of the azimuthal velocity increase and fluctuate between 0.07 and 0.25 for the remained of the measurement location as shown in Figures 4.28 and 4.29.

At the highest flow rate corresponding to a Reynolds number of 99000 the streamwise velocity profiles near the obstruction (less than 1D downstream) show negative mean velocity values including the presence of a recirculation zone (see Figures 4.20, 4.21). The velocities remain distorted until 5.5 D downstream of the obstruction. The fluctuating components of the streamwise velocity increase from 0.1 to 1 between ½ D up to 10.5 D downstream of the obstruction (see Figures 4.22, 4.23). The streamwise turbulence intensity increased up to a peak of 1400 % at 1.5 D and then decreased to 140 % at 10.5 D (see Figures 4.24 and 4.25). For this configuration, there were still strong effects of the obstruction that persisted beyond the test section outlet.

In the azimuthal direction, the obstruction did not seem to have a coherent effect on the mean velocity immediately downstream of the obstruction albeit the velocities are appreciable (between -1.5 and 1.5 m/s, see Figures 4.26, 4.27). Coherent azimuthal velocities developed around 2.5 D with mostly negative azimuthal components which may indicate the formation of swirl structures

(see Figures 4.28 and 4.29). This occurred throughout the entire measurement volume and hence the effects of the obstruction on turbulence continue wall beyond 10.5 D downstream.

As expected, the 2nd obstruction had a greater impact on the streamwise velocity flow profiles and streamwise turbulence intensity profiles. The azimuthal velocity profiles suffered a greater impact from the second obstruction as well.

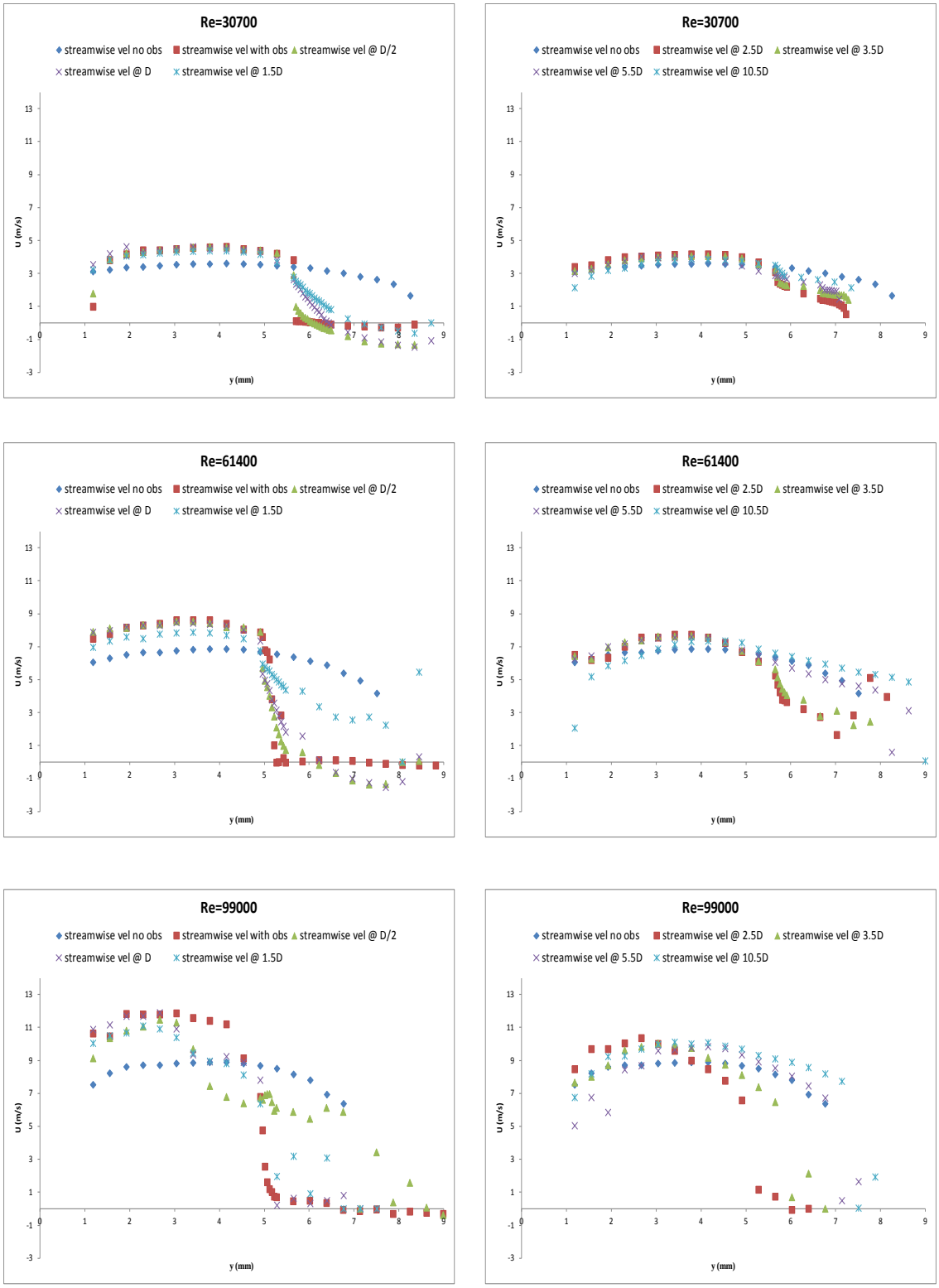

Figure 4.20 - Streamwise mean velocity profiles 2nd obstruction

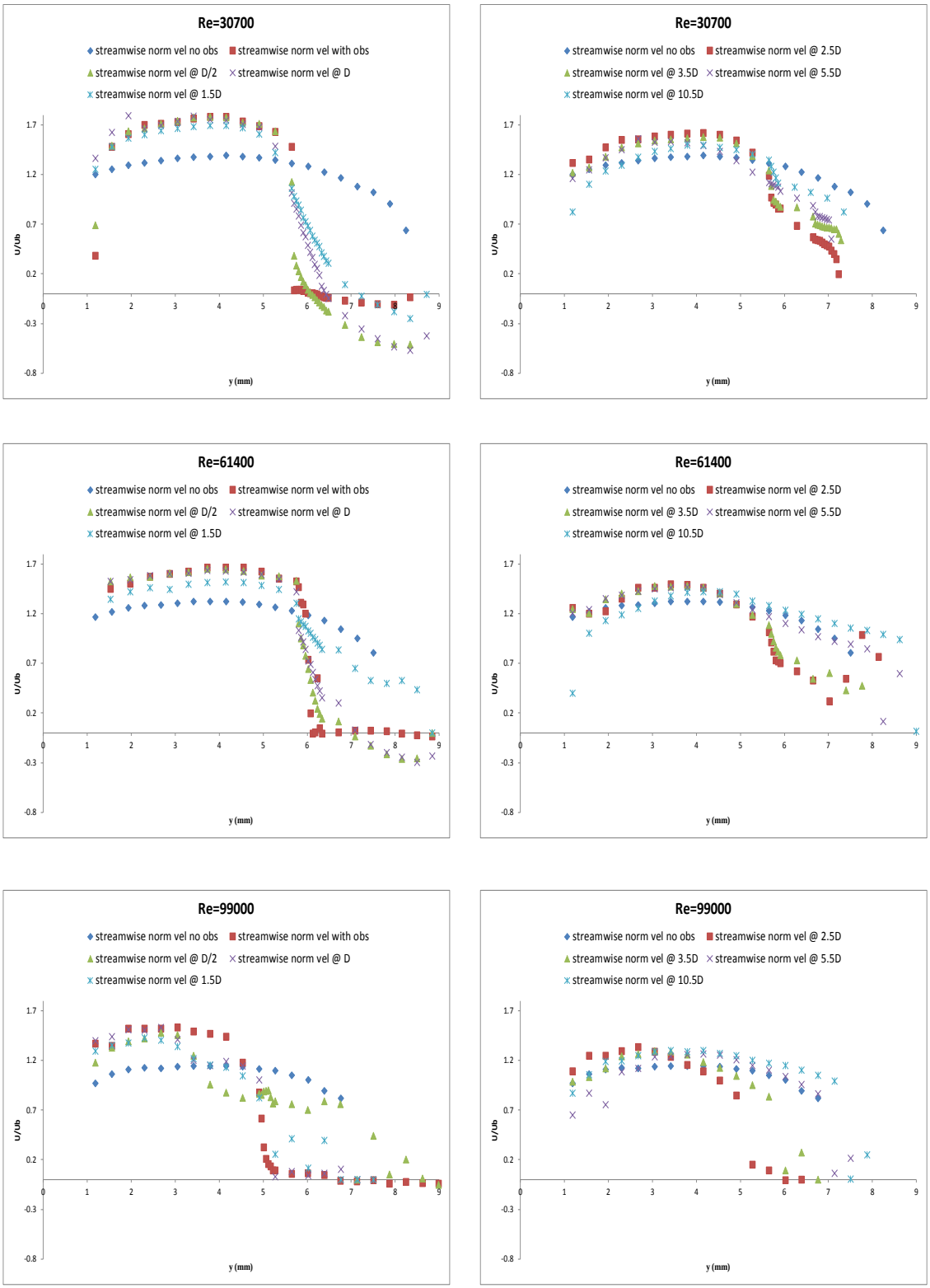

Figure 4.21 - Normalized streamwise velocity profiles 2nd obstruction

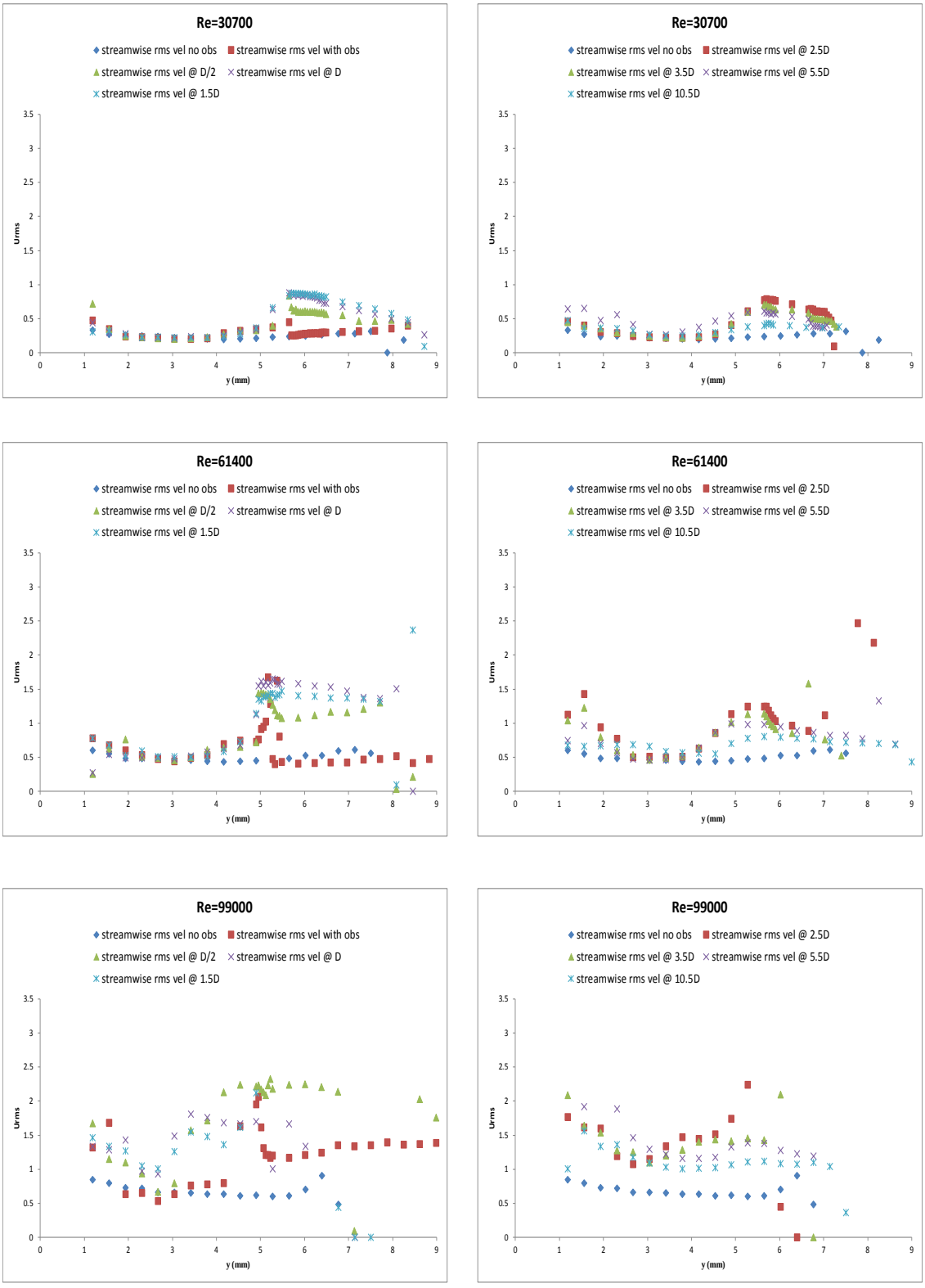

Figure 4.22 - Streamwise rms velocity profiles 2nd obstruction

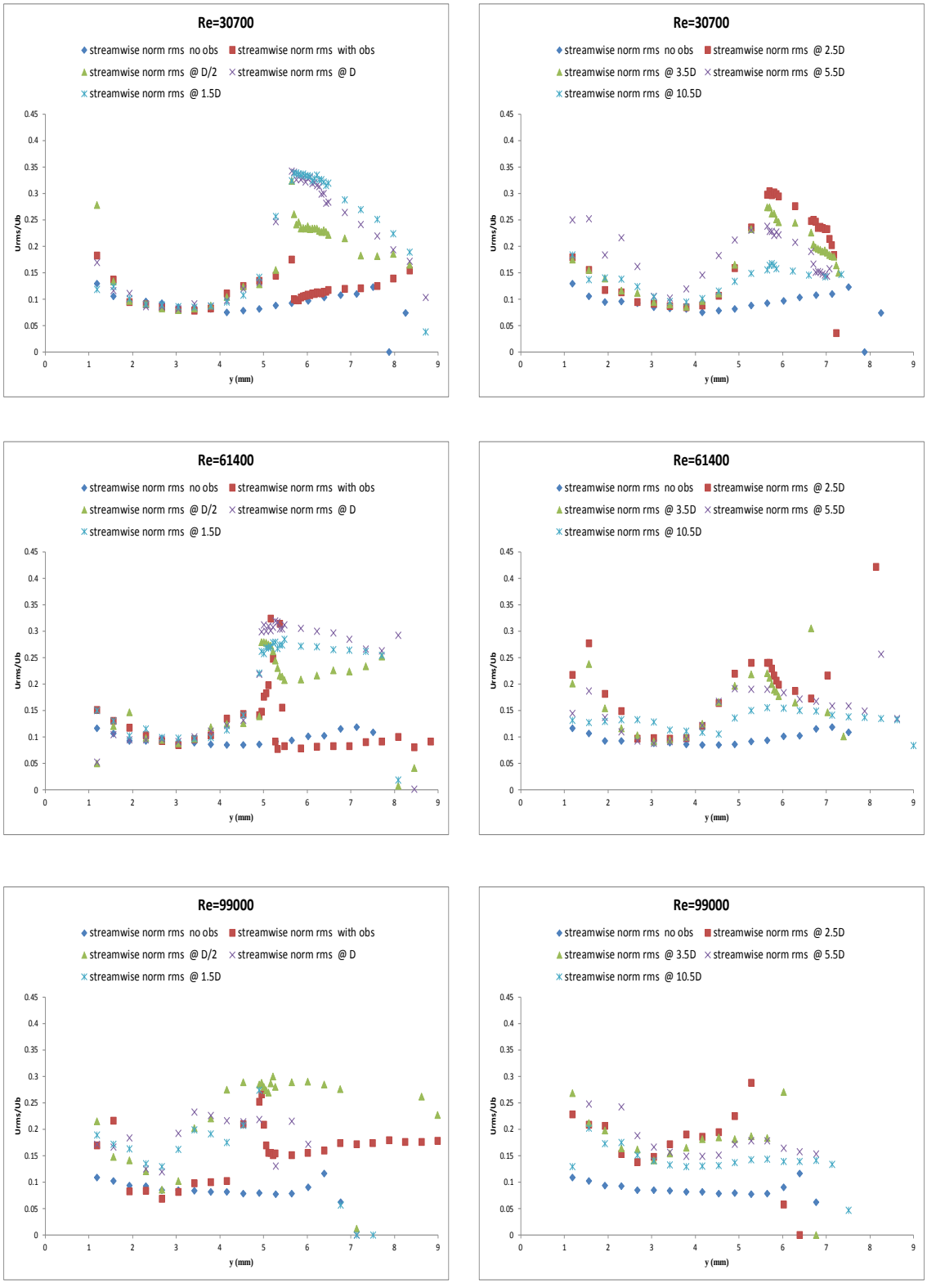

Figure 4.23 - Normalized streamwise rms velocity profiles 2nd obstruction

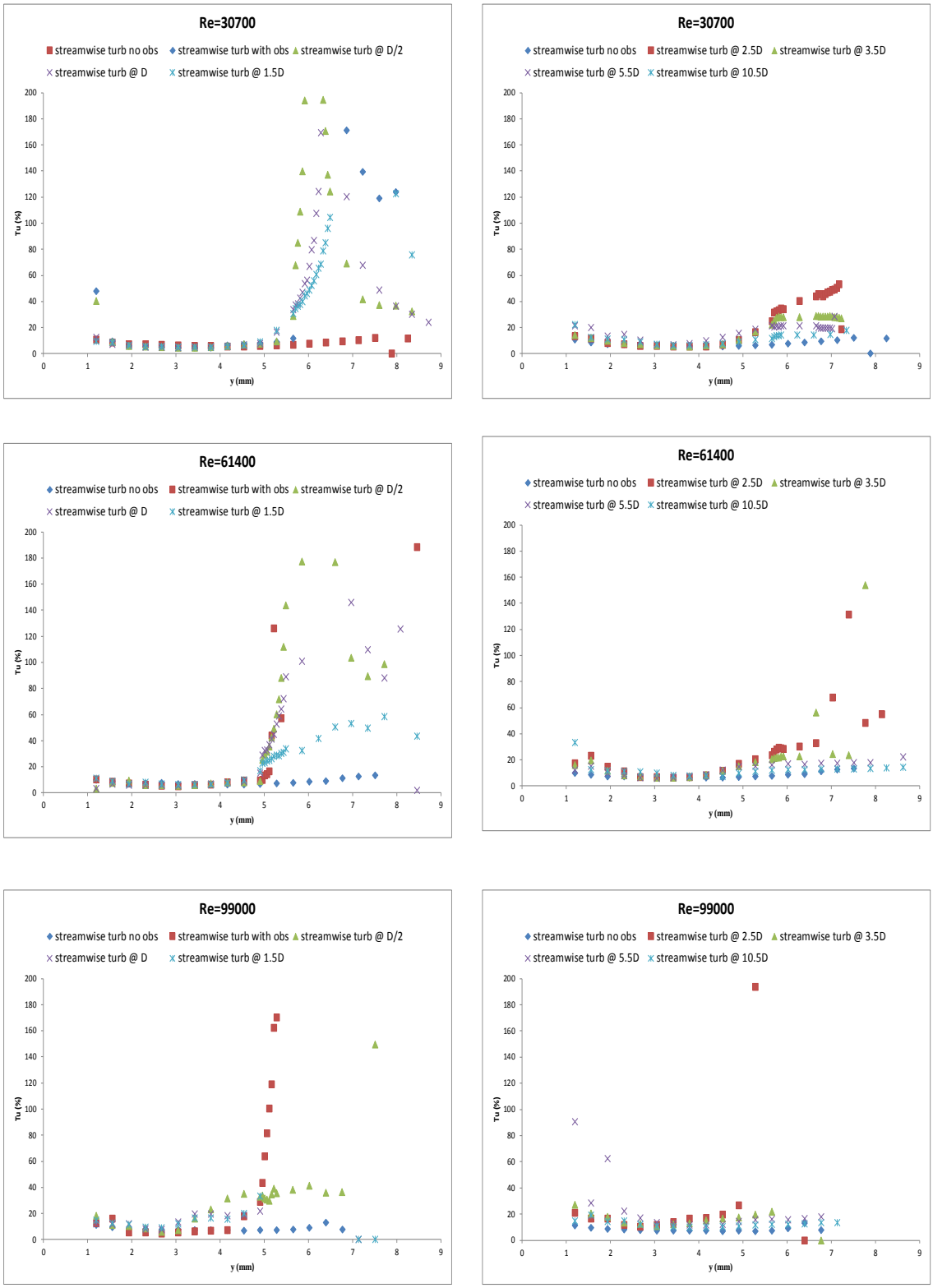

Figure 4.24 - Streamwise turbulence intensity profiles 2nd obstruction

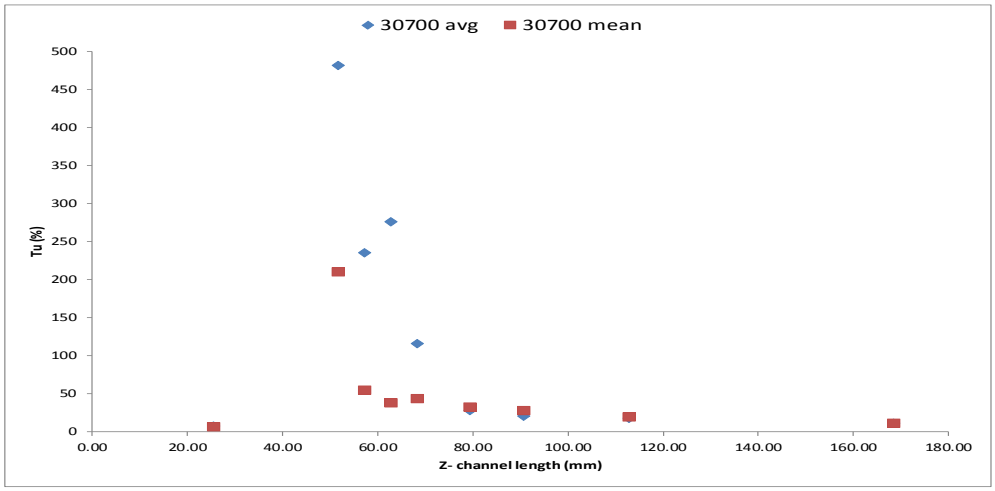

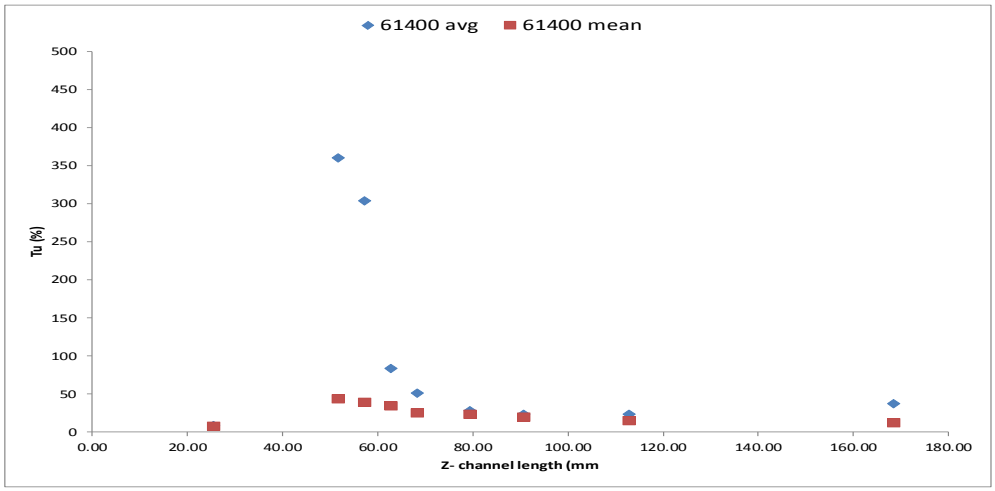

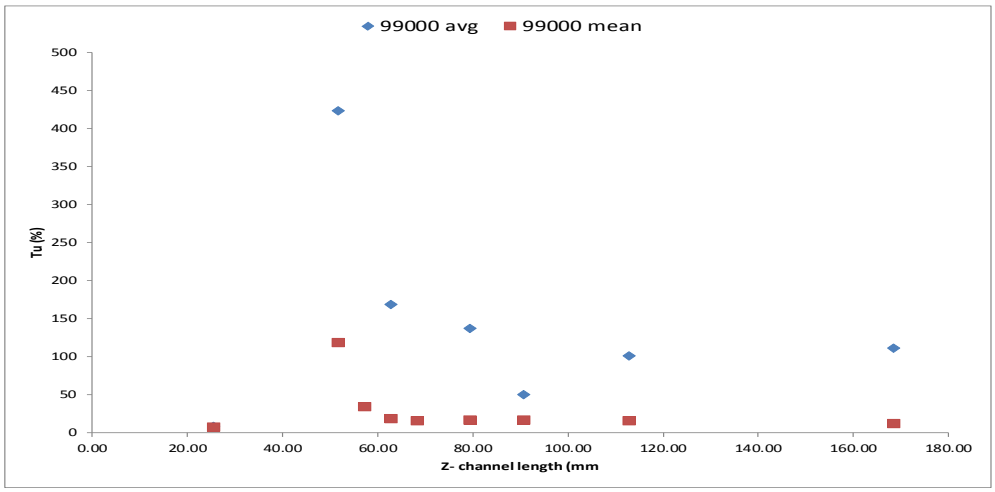

Figure 4.25 - Average & mean streamwise turbulence 2nd obstruction

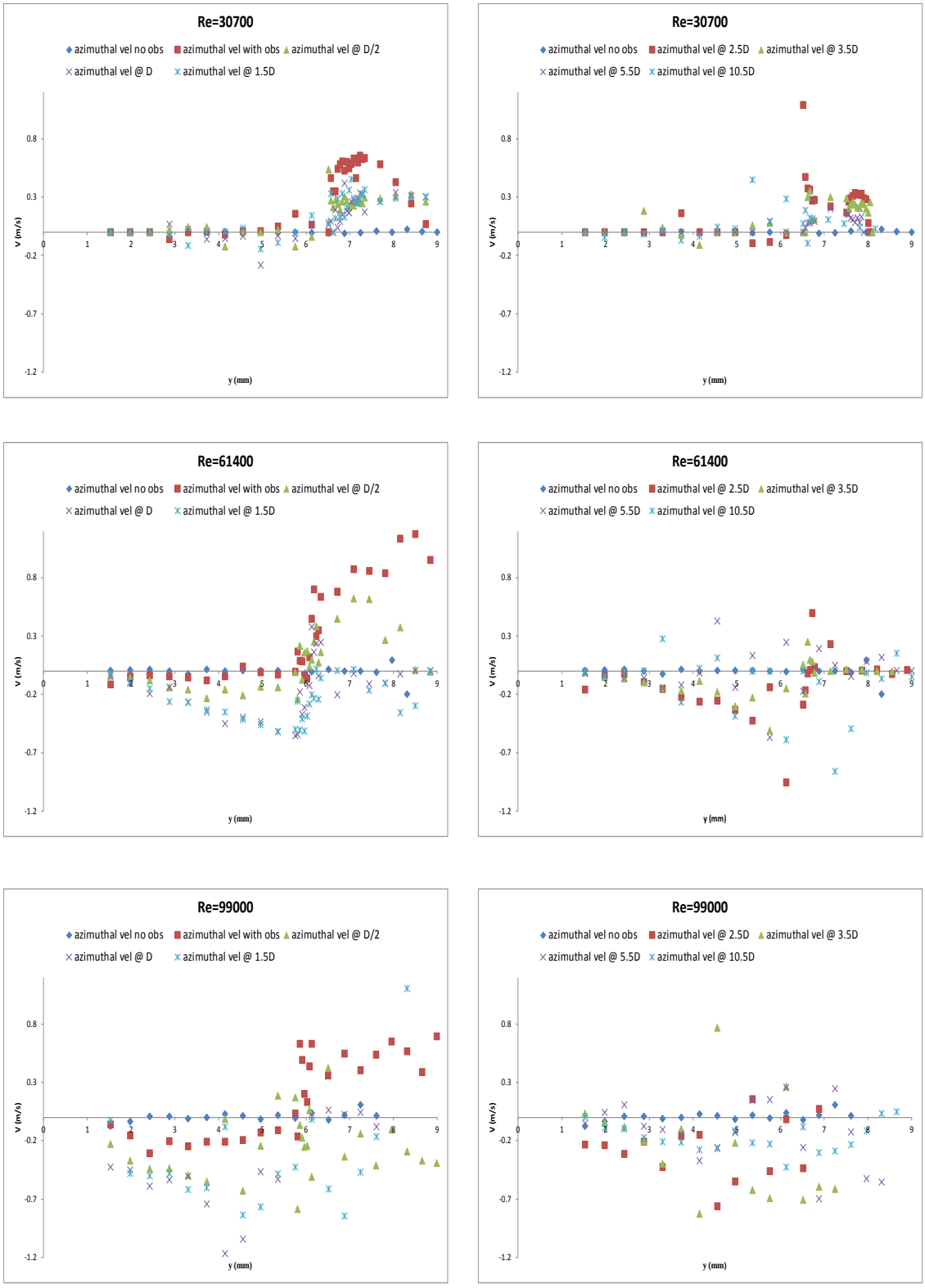

Figure 4.26 - Azimuthal mean velocity profiles 2nd obstruction

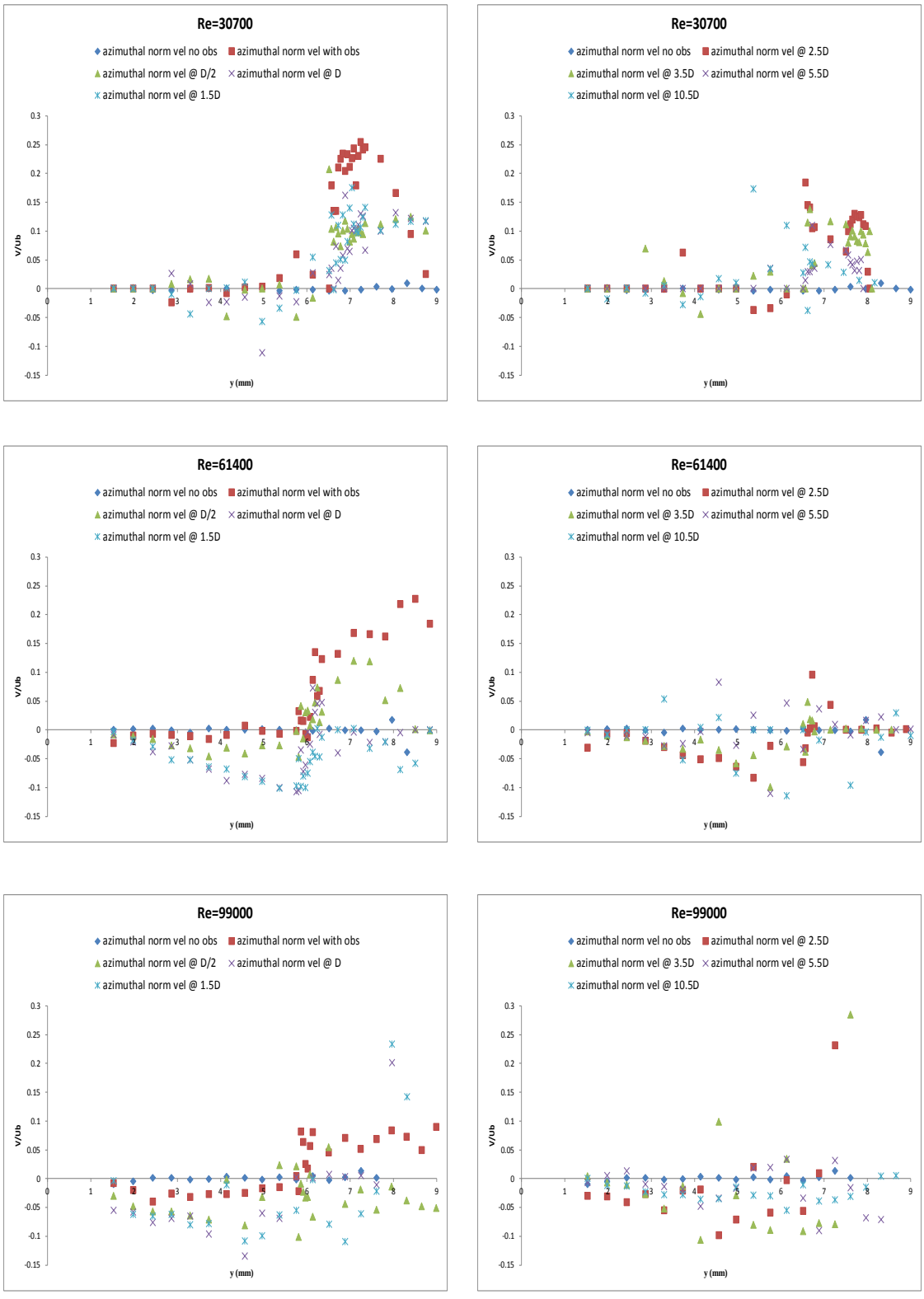

Figure 4.27 - Normalized azimuthal velocity profiles 2nd obstruction

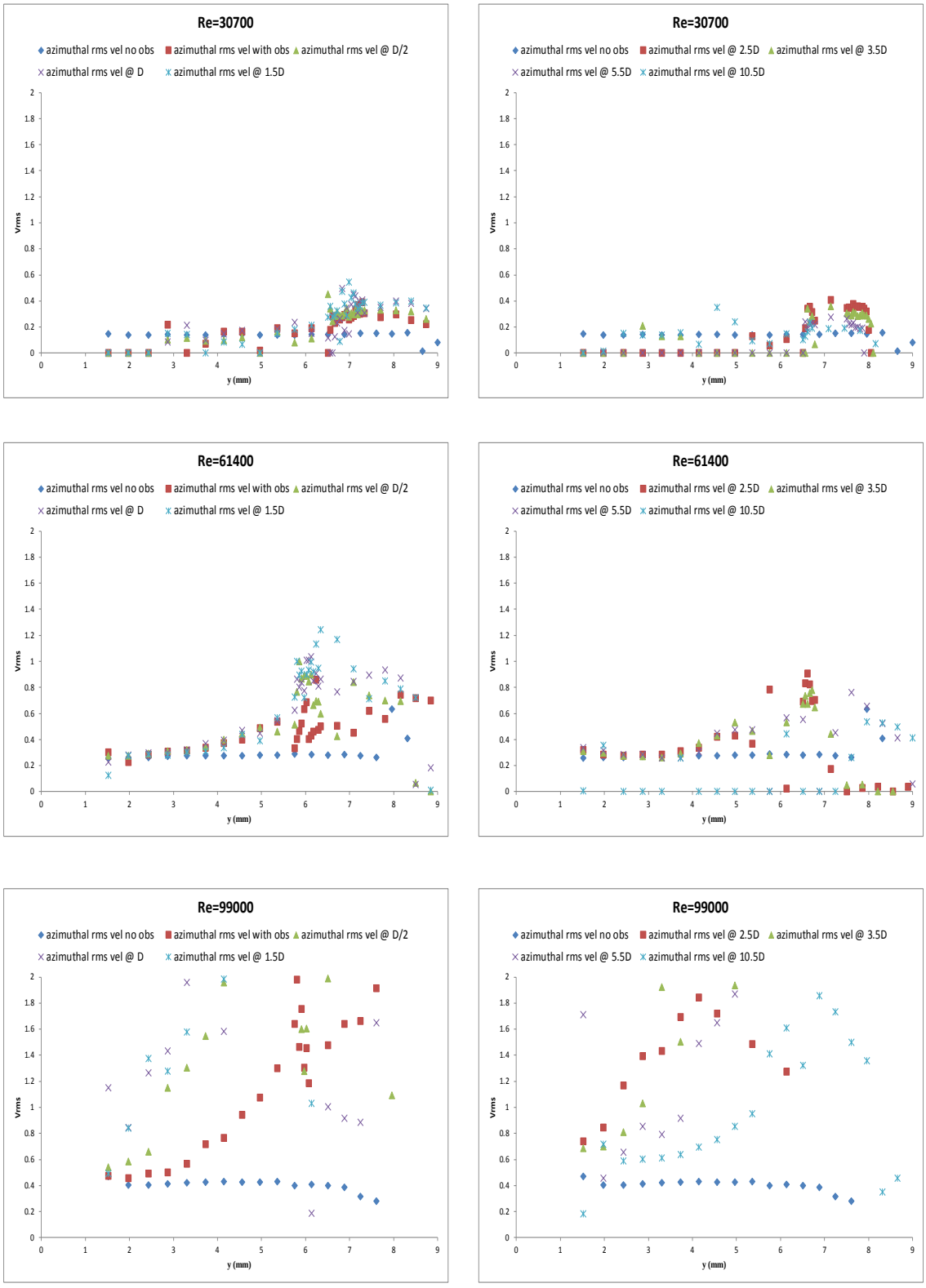

Figure 4.28 - Azimuthal rms velocity profiles 2nd obstruction

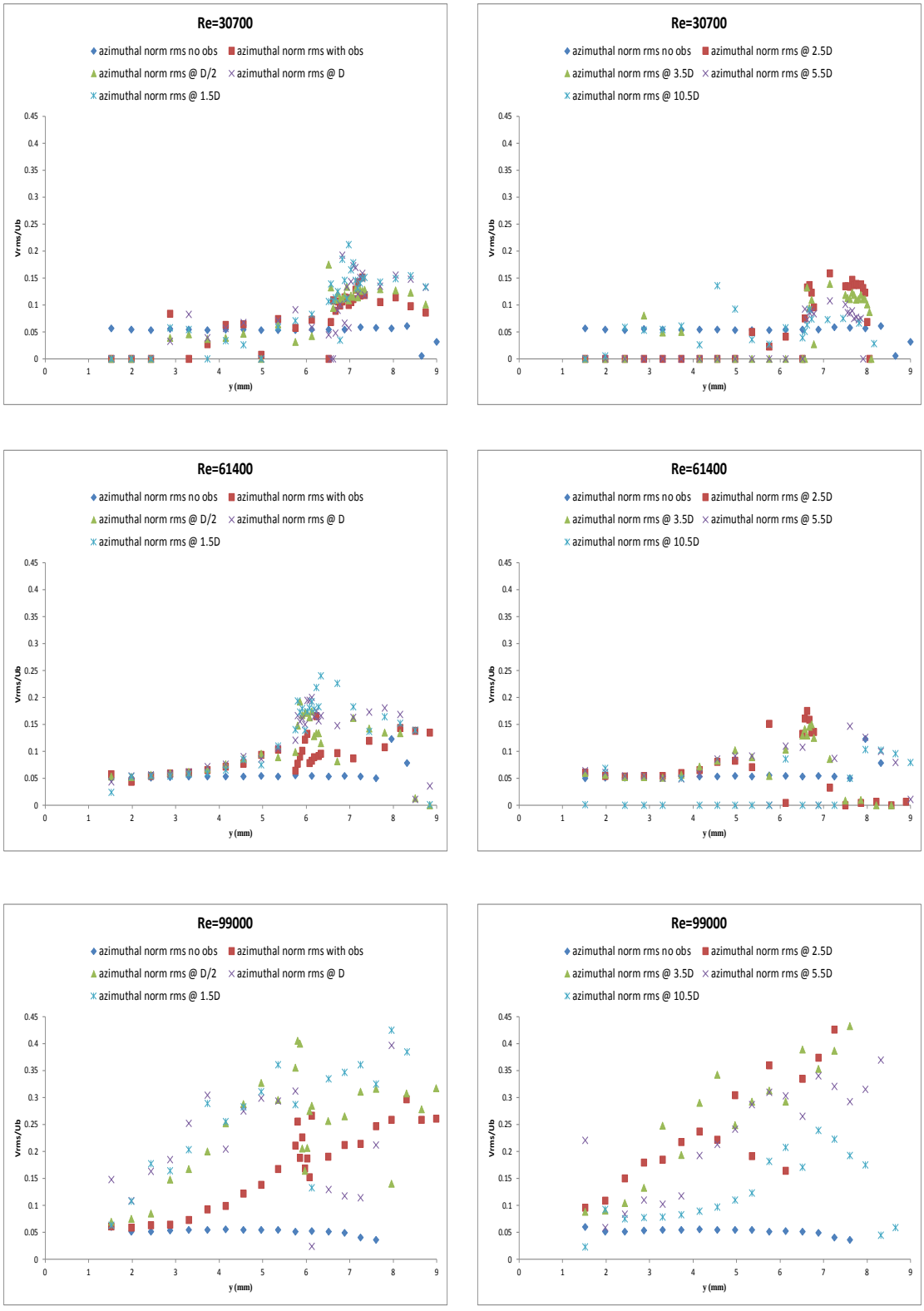

Figure 4.29 - Normalized azimuthal rms velocity profiles 2nd obstruction

4.4 - 60% Blockage Measurements

The third obstruction represents 61.14 % flow area blockage and for Reynolds number of 30700 the streamwise velocity profiles are significantly distorted and a recirculation region form; persisting up to 1.5 D downstream of the obstruction. The effects of flow profile deformation caused by the obstruction are visible up to 3.5 D downstream of the obstruction (see Figures 4.30, 4.31). At 5.5 D, the peak velocity maximum approaches the centerline and by 10.5 D downstream the profiles resemble the unobstructed patterns. The streamwise fluctuating component of the velocity increased and decreased sharply between 3 and 7 mm radially (i.e. near the trailing edge of the obstruction) up to 1.5 D downstream of the obstruction (see Figures 4.32, 4.33). The streamwise turbulence intensity increases reaching a peak of 500 % at 1 D (see Figures 4.34, 4.35) and gradually decreases remaining near 20% beyond 10.5 D downstream of the obstruction.

The azimuthal profile of the velocity appears to be completely random (see Figures 4.36, 4.37) at, ½ D with large positive and negative values over the diameter with a mean approximately of zero. From 1.5 D to 10.5 D the profiles behave in a similar manner, but the local maximum and minimum values seem to decrease as the flows move further from the obstruction. The fluctuating components of the azimuthal velocity seem to sharply increase near the trailing edge of the obstruction and gradually decrease as they approach the wall up to 1.5 D downstream. Beyond this point the local velocities fluctuate randomly with no discernable pattern (see Figures 4.38, 4.39).

At higher flows corresponding to a Reynolds number of 61400, the streamwise velocity profile suffers a greater and longer decrease when compared to the previous flow rate which indicates a larger recirculation zone; local velocities values close to zero and negative were observed up to 10.5 D downstream of the obstruction (see Figures 4.30, 4.31). The velocity profile right after the

obstruction suffers a steep decrease to negative values at around 3 mm radially, then at 6.5 mm it becomes positive again and ultimately decreases to zero. At 2.5 D, the local velocities decrease at a slower rate than upstream, but they still cross values below zero. The fluctuating components of the streamwise velocity seem to rapidly increase midway of the obstruction radial location for all 10.5 D downstream of the obstruction (see Figures 4.32, 4.33); note that the local rms velocities do not drop back to near zero values within the measurement domain. The streamwise turbulence behaves non-monotonically (see Figures 4.34, 4.35).

In the azimuthal direction, the profile of the velocity right after the obstruction is mainly positive (see Figures 4.36, 4.37) with local velocities between -1.5 and 2 (i.e., approximately 30% of the streamwise component). All other azimuthal profiles after the obstruction are negative, up to 10.5 D downstream of the obstruction. The fluctuating components of the azimuthal velocity are almost all negative aside from the position right after the obstruction (see Figure 4.38, 4.39), which indicates the presence of swirl-like structures. This obstruction appears to generate coherent structures which persist much further downstream than the normal obstruction related turbulence phenomena.

At the highest flow rate corresponding to a Reynolds number of 99000 the streamwise velocity profile reverse flow is observed in the wake of the obstruction up to 1.5 D downstream and in the velocity profile distortions are observed up to 5.5 D downstream (see Figures 4.30, 4.31). At 10.5 D, it reverts to a typical turbulent flow profile, although the global maximum velocity for that distance is asymmetric relative to the geometric centerline. The streamwise velocity rms profiles almost triple within 1.5 D downstream of the obstruction. As the flow moves further from the obstruction, the local rms values start to decease and become steadier or stabilized (see Figures 4.32, 4.33). The streamwise turbulence intensity increases from an unobstructed value of 8 % to

1200 % right after the obstruction and after ½ D drops to 250 %, a small increase to 270 % is observed between 1 and 1.5 D downstream of the obstruction with non-monotonic behavior up to 1.5D (see Figures 4.34, 4.35). The turbulence intensity eventually decreases to 14 % at 10.5 D downstream of the obstruction.

In the azimuthal direction, the mean velocity profile right after the obstruction increases steeply as it approaches the radial centerline and then decreases to negative values (see Figures 4.36, 4.37); the flows after ½ D from the obstruction are mostly negative, and even after 10.5 D downstream the rotational velocities remain significant. The fluctuating components of the azimuthal velocity behave similarly to the lower flow rates. However, the local V_{rms} values are lower when compared to the previous flow rate (see Figures 4.36) which indicates that the structures have less fluctuation.

Of the 3 obstructions studied, the 3rd had the largest impact on the streamwise velocity and turbulence profiles but the largest increase in average turbulence intensity was observed at Reynolds number of 61400. The azimuthal velocity profiles became increasingly negative with higher Reynolds number and larger obstructions, which eventually originated large scale structures believed to be swirl in nature, although no swirling devices were present and none was observed in the unobstructed flow. No swirl-like structures were observed with obstructions at low Reynolds numbers either and the presence of these structures persisted beyond the test section downstream measurement locations.

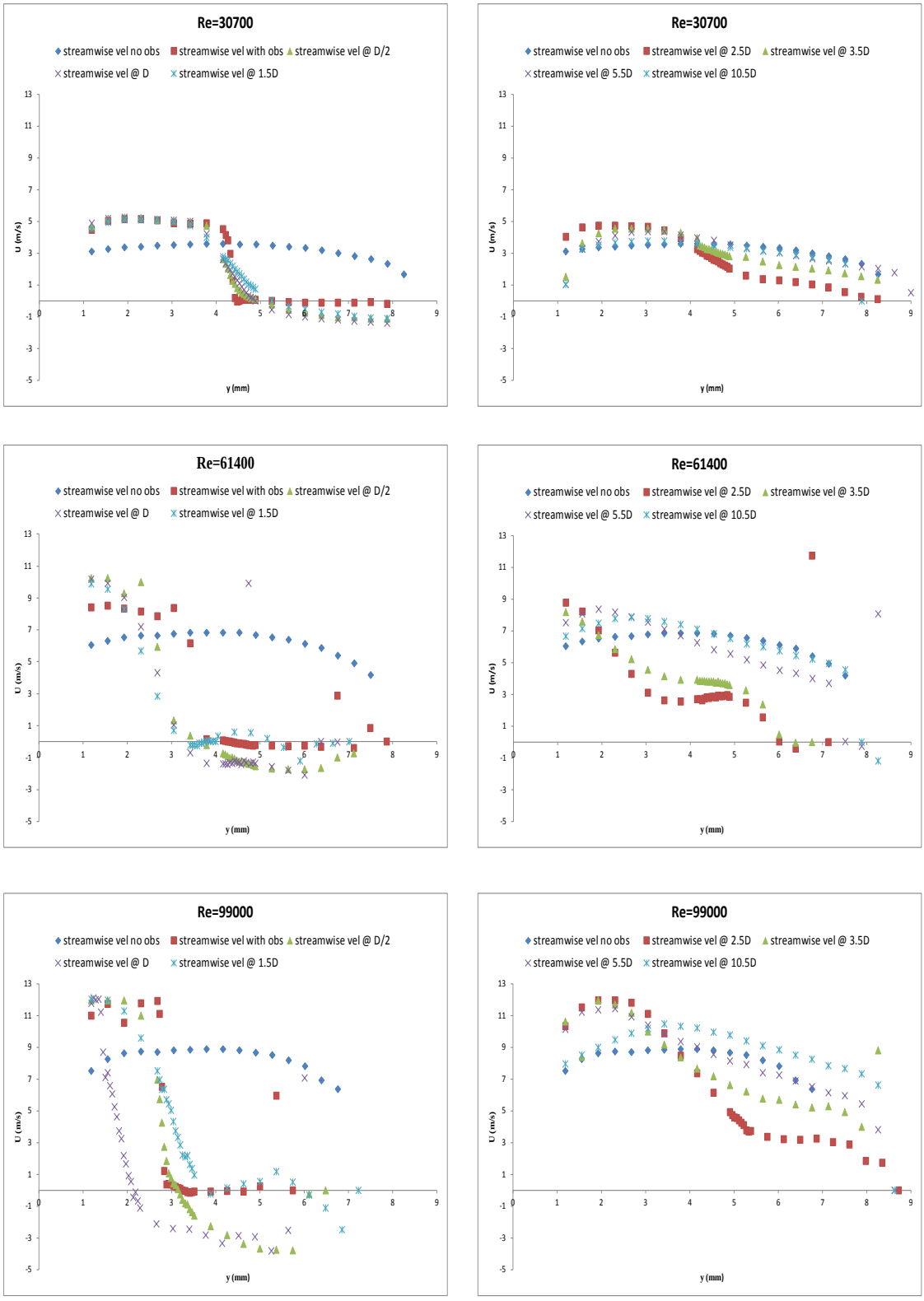

Figure 4.30 - Streamwise mean velocity profiles 3rd obstruction

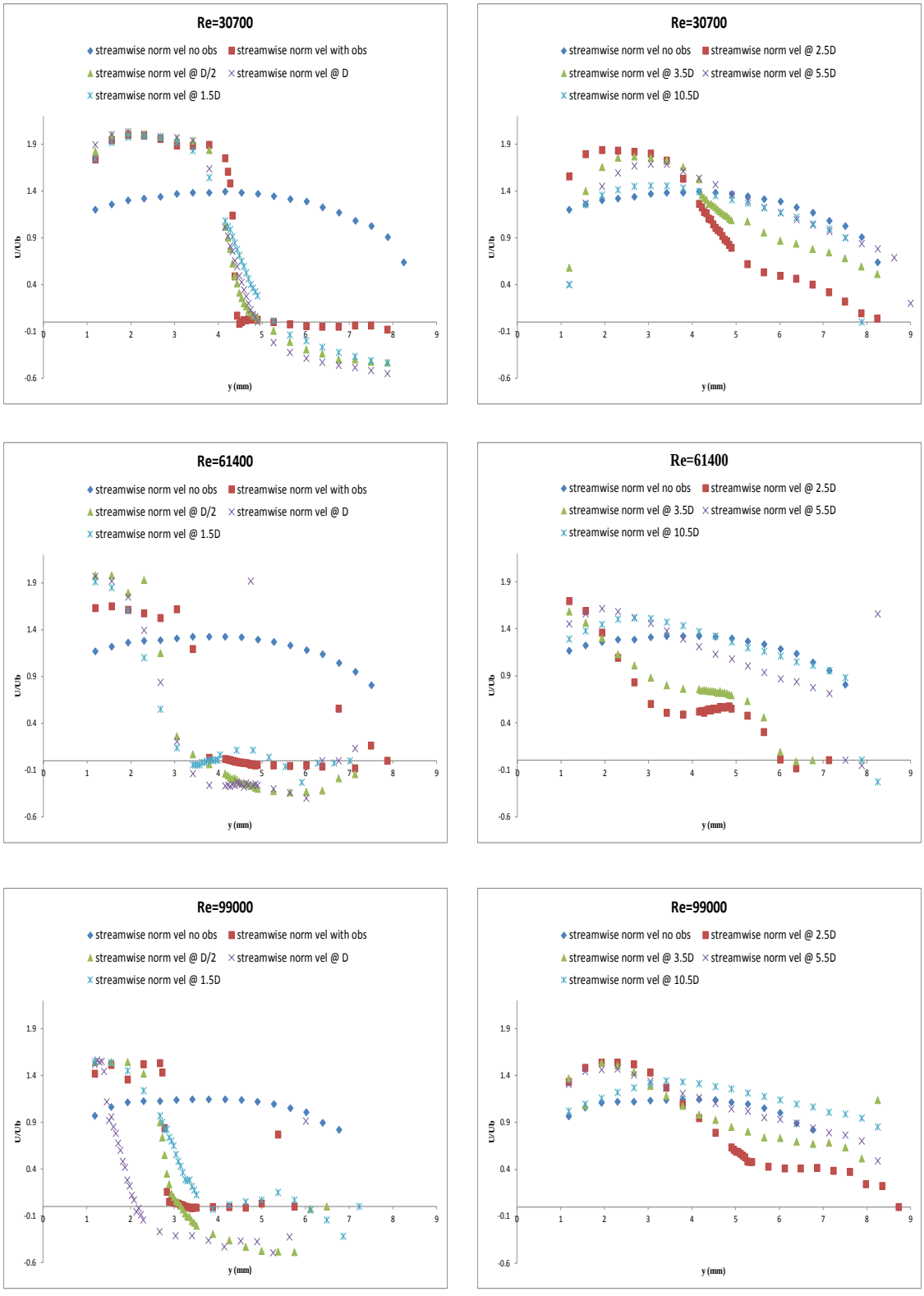

Figure 4.31 - Normalized streamwise velocity profiles 3rd obstruction

Figure 4.32 - Streamwise rms velocity profiles 3rd obstruction

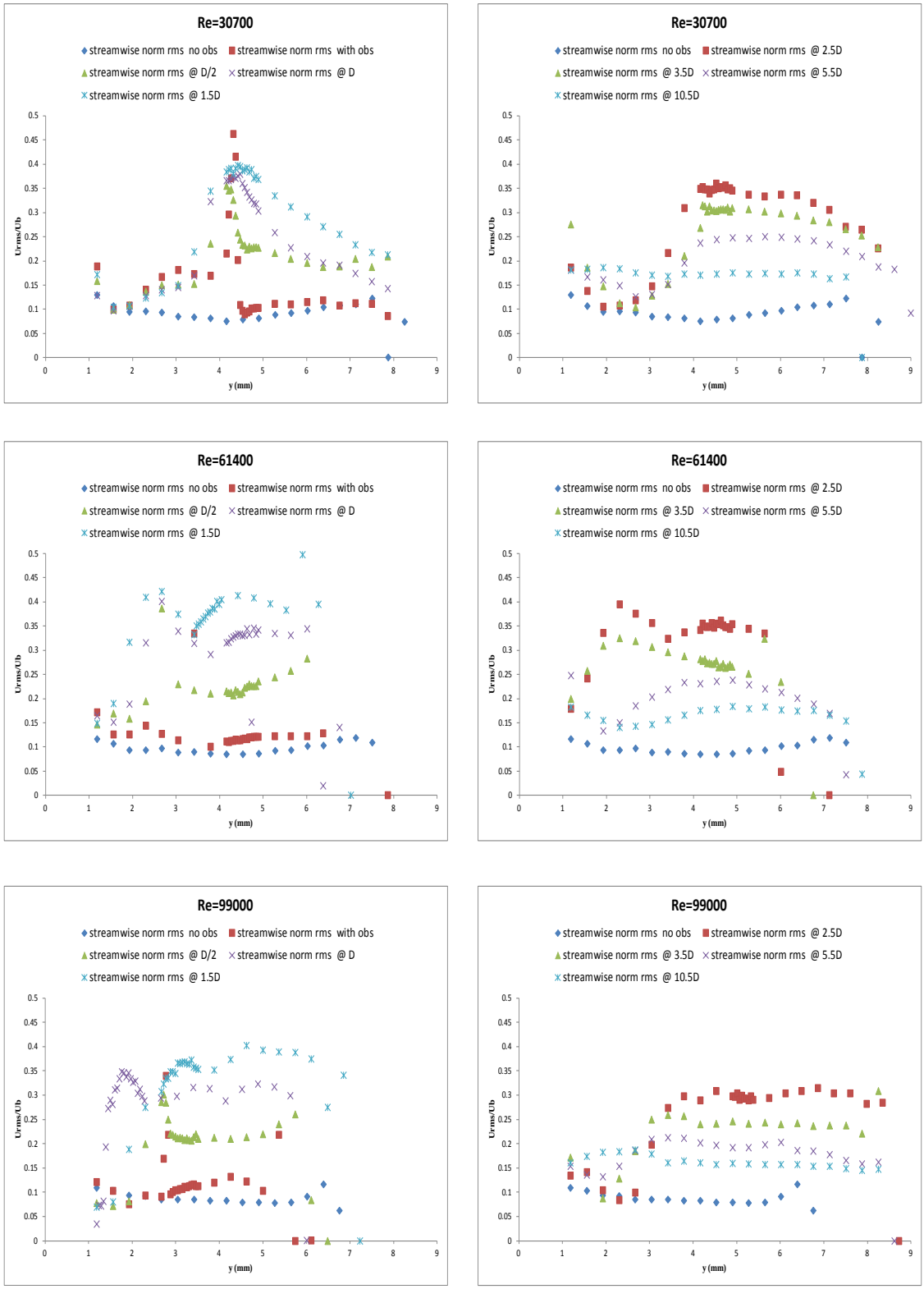

Figure 4.33 - Normalized streamwise rms velocity profiles 3rd obstruction

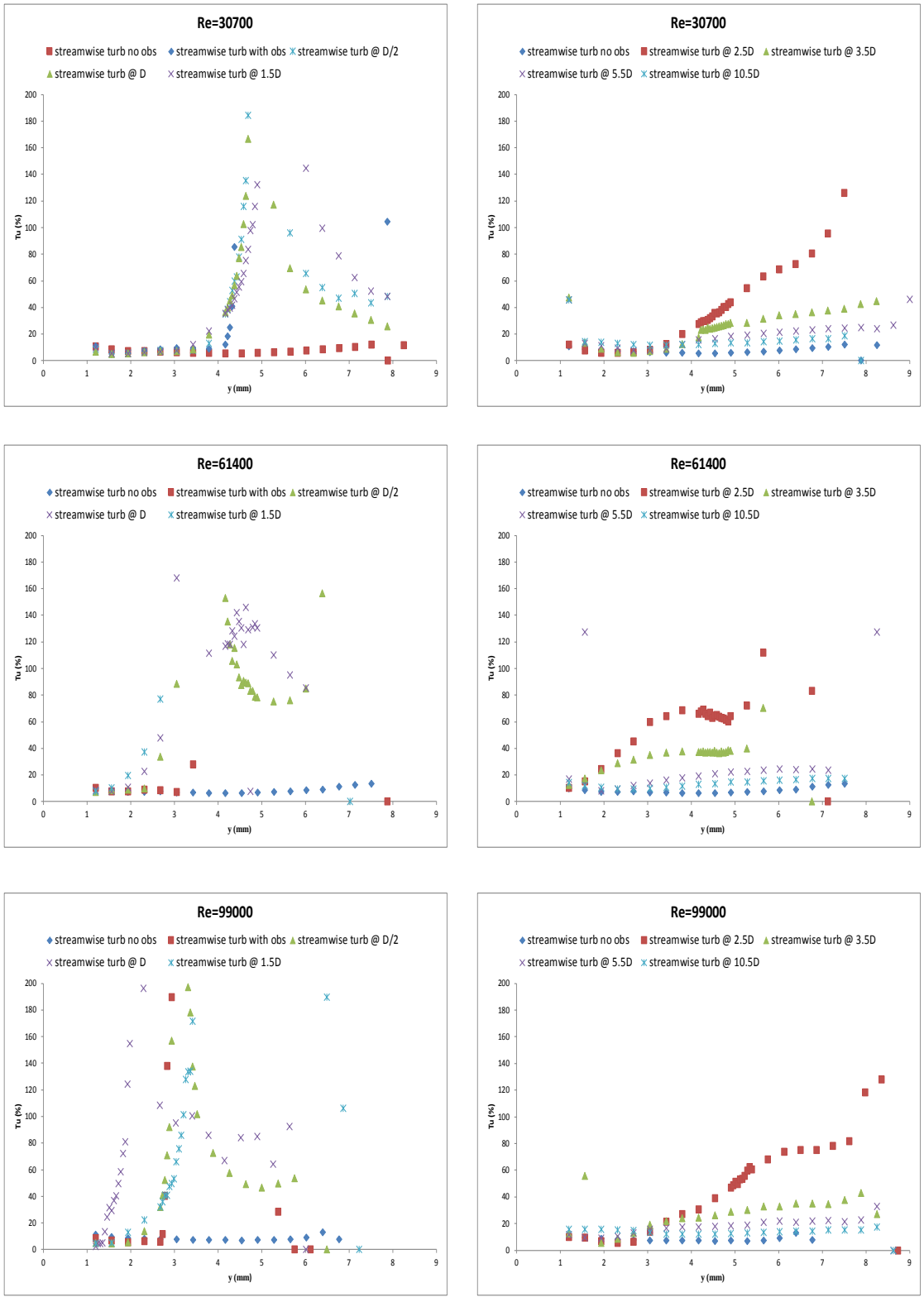

Figure 4.34 - Streamwise turbulence intensity profiles 3rd obstruction

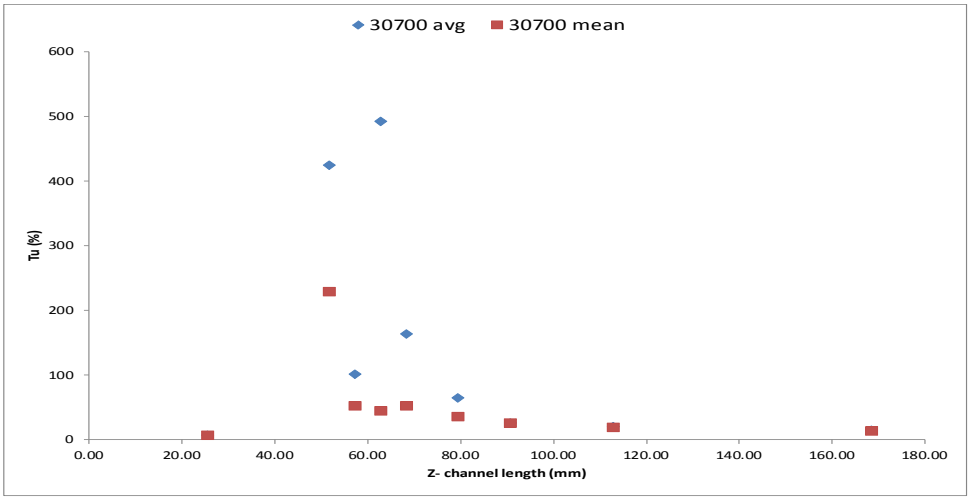

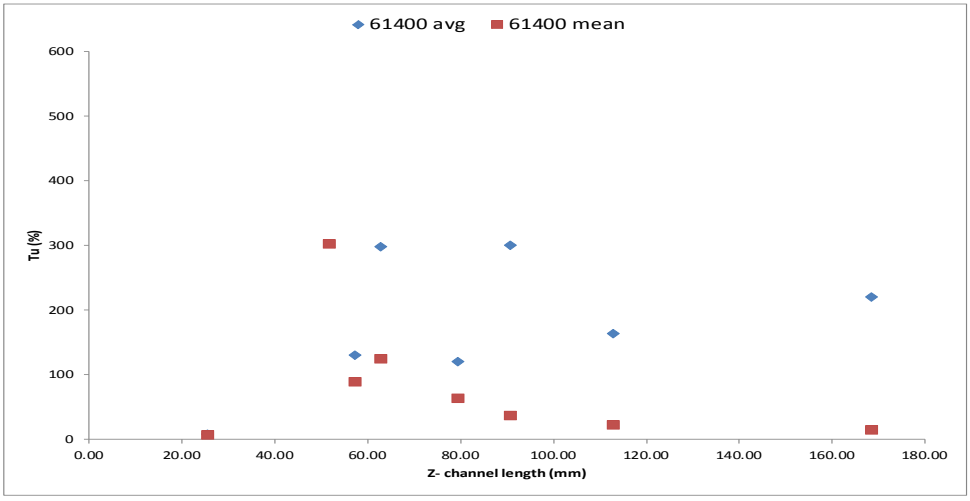

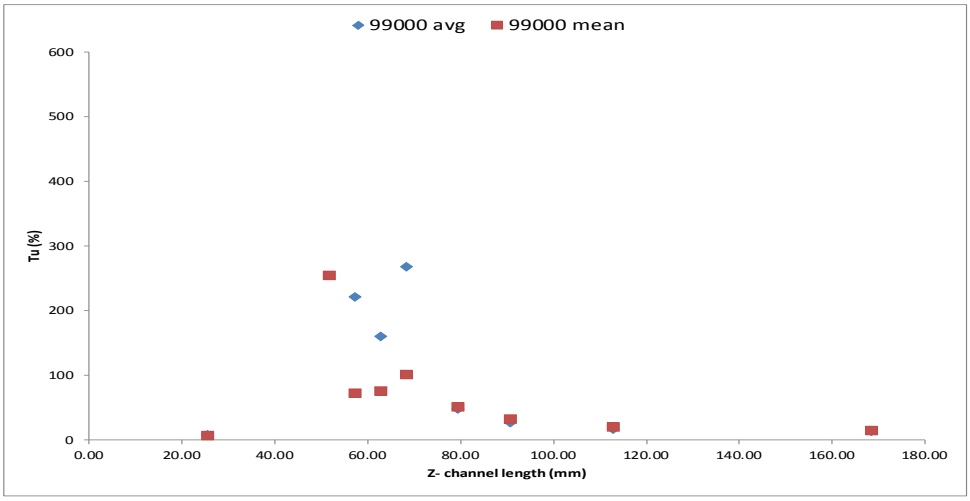

Figure 4.35 - Average & mean streamwise turbulence 3rd obstruction

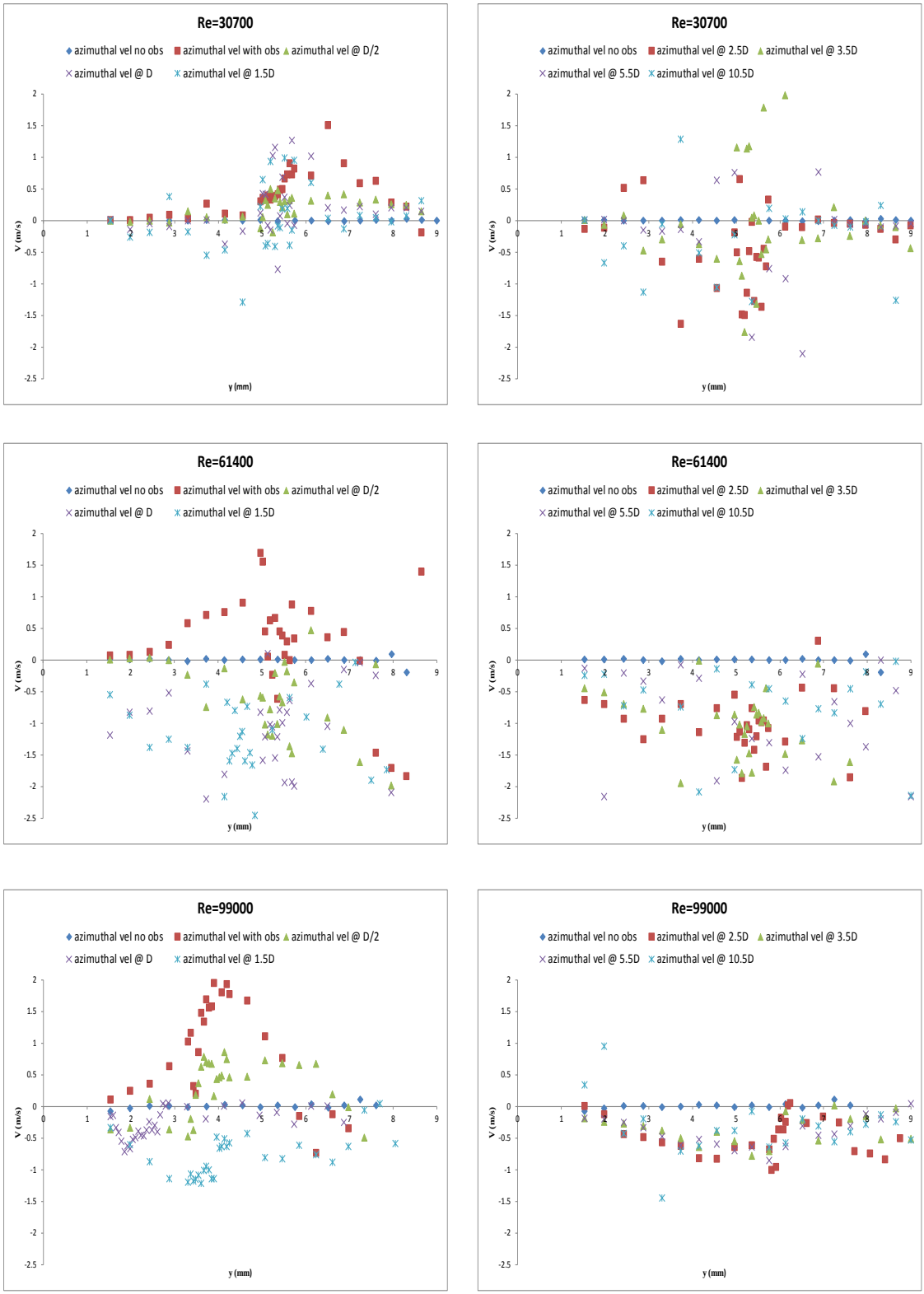

Figure 4.36 - Azimuthal mean velocity profiles 3rd obstruction

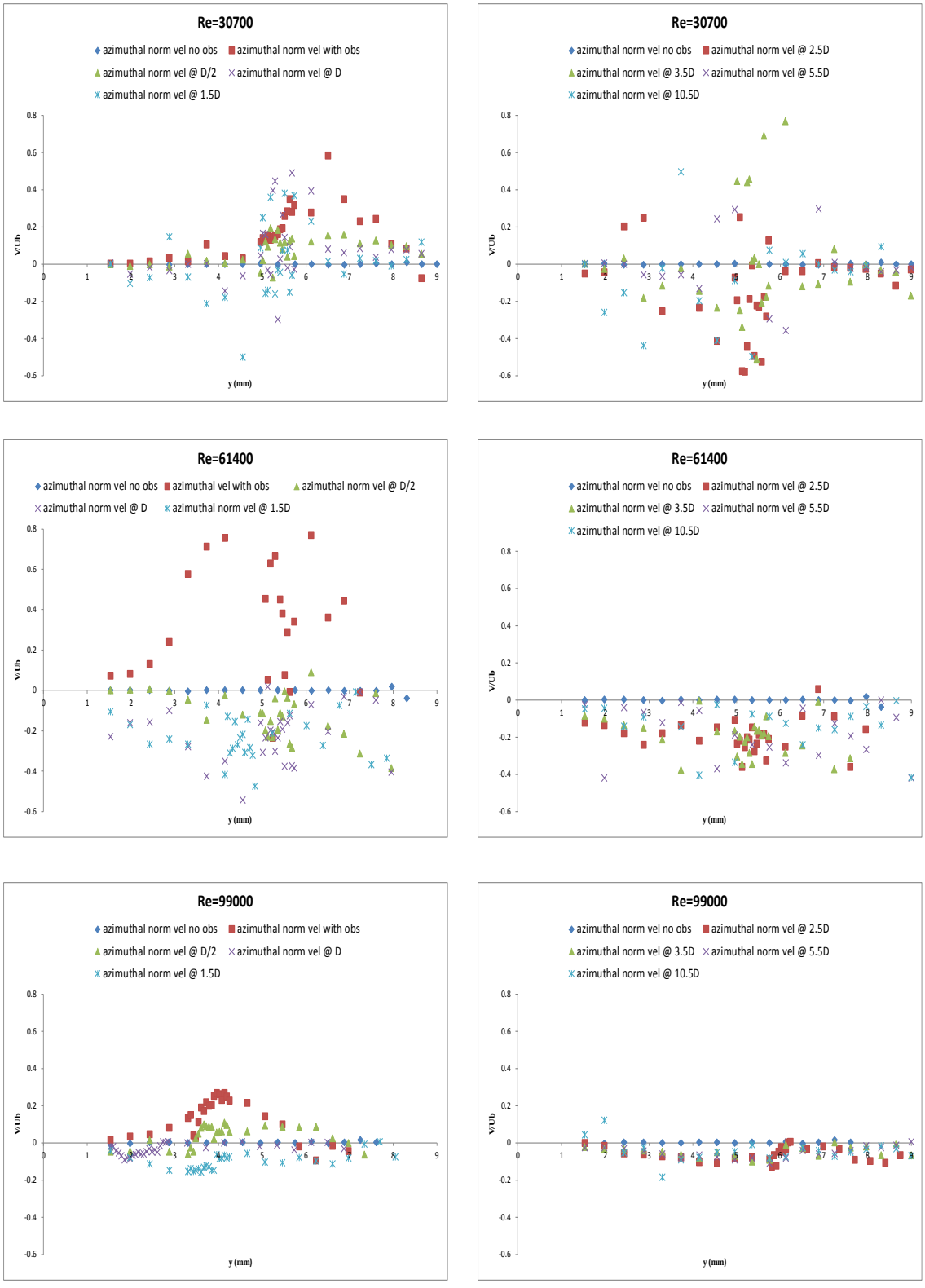

Figure 4.37 - Normalized azimuthal velocity profiles 3rd obstruction

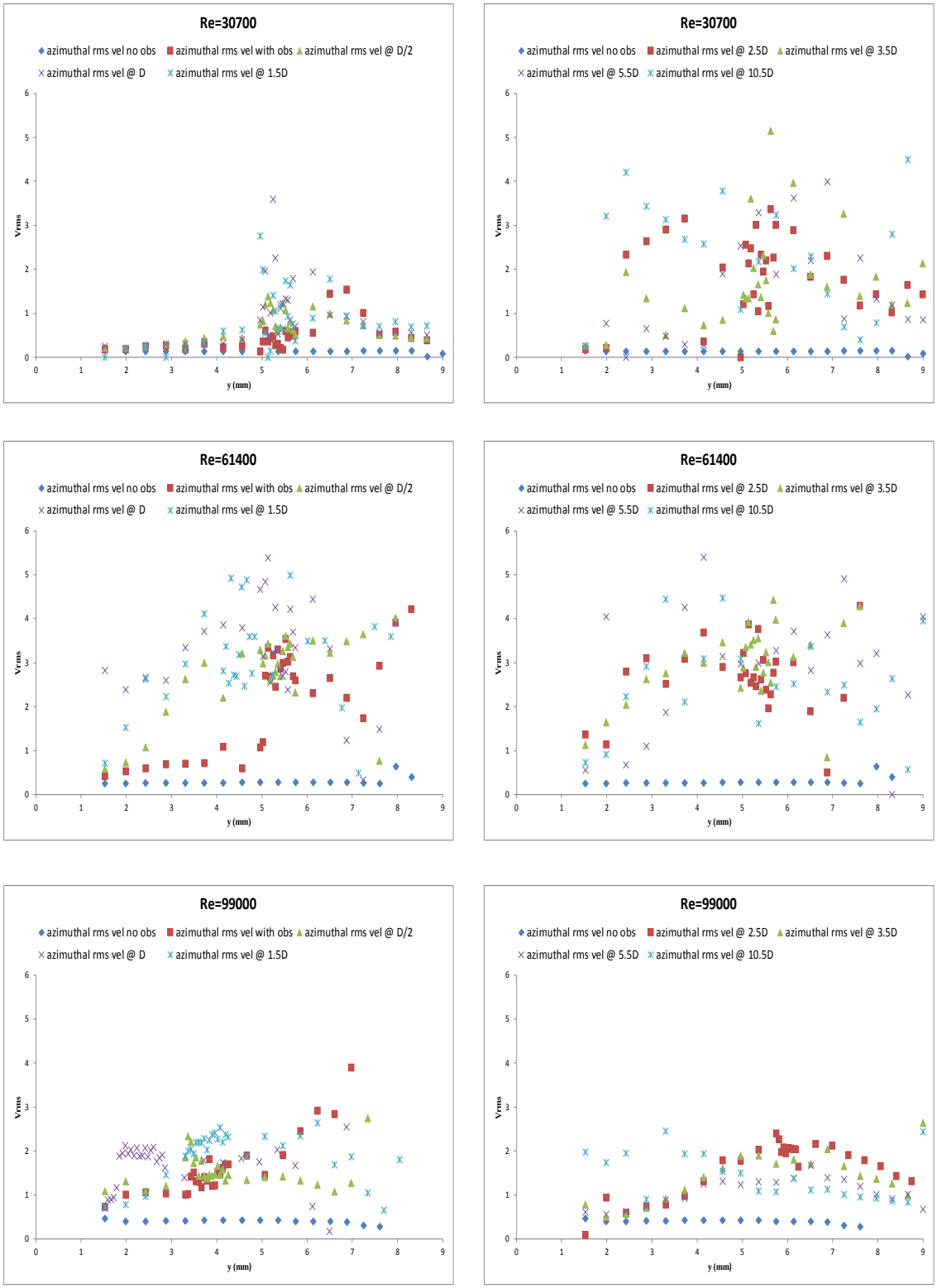

Figure 4.38 - Azimuthal rms velocity profiles 3rd obstruction

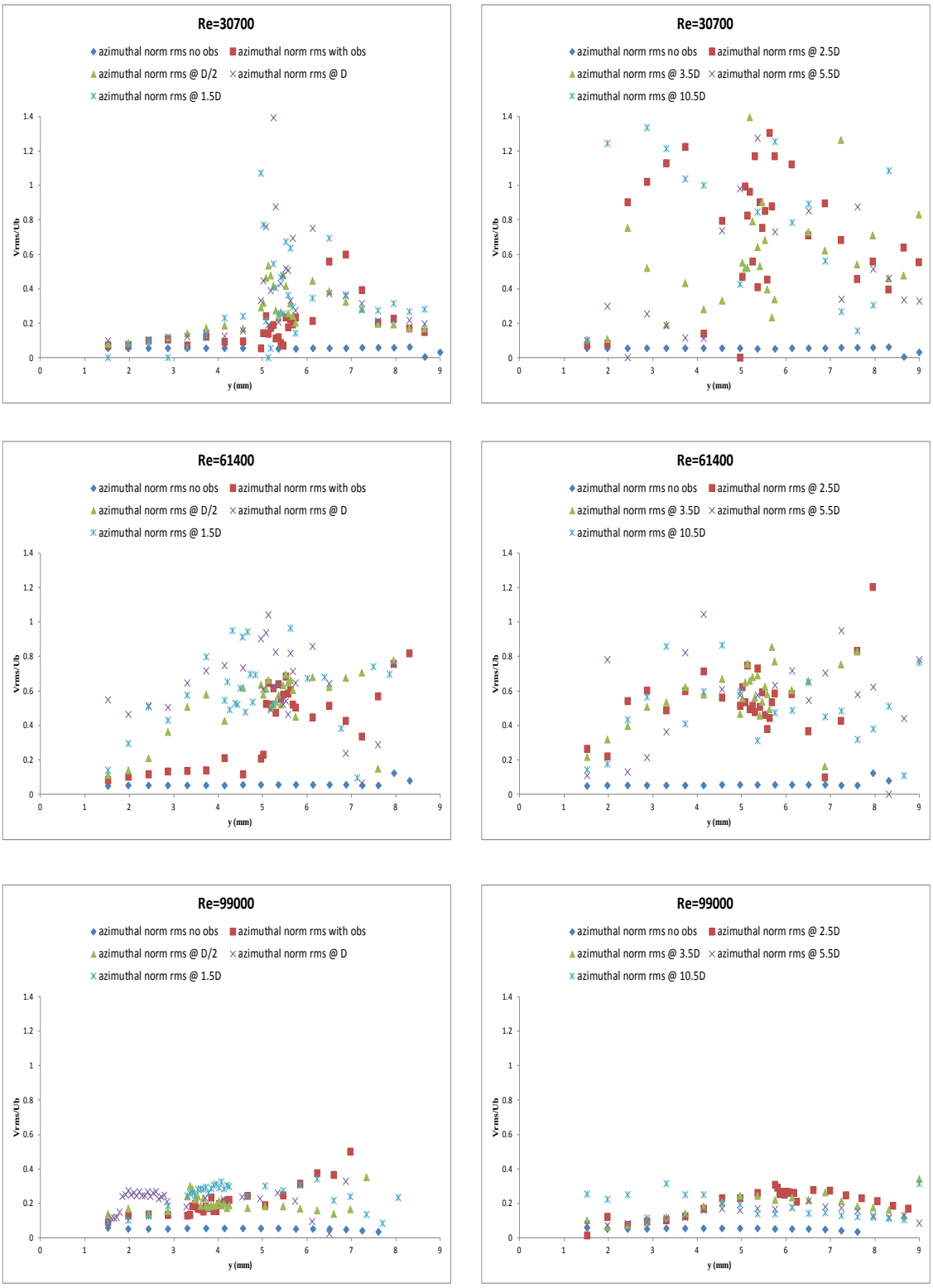

Figure 4.39 - Normalized azimuthal rms velocity profiles 3rd obstruction

5. Closure

This brief chapter describes the essential findings from in this experimental study. The first section describes the most significant phenomena observed downstream of the obstructions and the possible source of these observations. The second section describes what the author feels should be the next steps to take to further study and describe the significant observed phenomena and its possible benefits to CHF.

5.1 - Conclusions

The aim of this thesis is to analyze the velocity and turbulence characteristics of water flow downstream of 3 different obstructions which are representative in size to those in a standard CANDU bundle. This study is motivated by the ongoing and growing investigation on critical heat flux and post dryout phenomenona in nuclear reactors and the influence of obstructions. Radial profiles of mean velocity, RMS of the fluctuations and the turbulence intensity were simultaneously measured using a LDV system in the streamwise and azimuthal directions at Reynolds numbers of 30700, 61400, and 99000. Data was acquired at eight different axial locations downstream of each obstruction, and the uncertainties in the mean velocity and rms fluctuation values estimated from experimental calibrations were ±5%. Uncertainties in process measurements were estimated to be less than 2% based on manufacturing calibration.

The most significant phenomenon observed was the generation of large scale structures for the larger obstructions and higher Reynolds number cases. For the smallest obstruction no coherent structures were measured at the flow rates examined and measured turbulence seemed approximately isotropic (within reasonable bounds). The turbulent behavior decayed with

distance and levels returned to nominal values by 10.5D. this was also true for the intermediate obstruction at the lowest flow rate, however for this obstruction at higher flow rates and for the largest obstruction at all flow rates coherent structures were measured in the azimuthal direction. These structures are believed to be swirl in nature, although no swirling devices were present and none was observed in the unobstructed flow. These observations are based on measurements which indicate that the azimuthal mean velocity components had systematic direction and large magnitude downstream of the obstructions. For conditions where coherent structures were observed, the increased turbulence generated by the blockages persisted beyond the test section (beyond 10.5D). The cause of the swirl under the high Reynolds number and obstructions is not evident. However, the following should be noted:

1. The results were repeatable on different days and with spacer removed and the reinserted;
2. The spacer dimensionality checks show no differences in geometry beyond design tolerances of the spacer and the spacer is symmetrical about its streamwise length;
3. Swirl was observed for different spacers, hence any manufacturing defect in the spacer geometry, or in the positioning of the spacer in the channel would likely have shown inconsistent behavior between spacer tests;
4. On the same spacer (intermediate size) swirl was observed only at higher Reynolds numbers (beyond 30700)

Irrespective of the source of the swirl measured in the experiments, once swirling structures were generated, they caused a significant change in the observed turbulence behavior. In particular the impacts of the obstruction persisted much further downstream when the swirls structures were present (well beyond 10.5D available measurement window in this work). When swirling structures were not present, in general the impact of the obstruction behaved as expected and the

velocity and turbulence levels approached their unobstructed values within 3 to 10D, depending on the conditions and blockage analyzed.

5.2 - Future work

Given the observed generation of large scale structures downstream of the larger obstructions, their specific conditions of origin and lasting effects downstream of the obstruction need to be further investigated, the author recommends the following steps:

1. Repeat the experiments in a longer test section, with a wider range of post obstruction measurement positions.
2. Repeat the experiments using visual measurement techniques like Particle Image Velocimetry
3. There is no defined correlation between the geometry and size of the test section channel and obstructions blockage area, so the experiments should be repeated in difference channel geometries and dimensions as well as a larger variety in size of obstructions (their placement within the test section cross wise, measurements against the flow should also be considered).
4. Repeat the experiments with smaller intervals in Reynolds number (between 30700 and 61400), to determine the approximate Reynolds number and flow velocity that facilitate the formation of swirl-like structures.
5. A computational fluid dynamics simulation of the test section with the obstructions and flow characteristics would be useful as well, to verify if these results can be achieved to some degree with CFD.

6. Determine the effects of the swirl-like structures on the higher order statistics of the velocity and turbulence, as well as power spectrum in a temperature and pressure controlled loop, to further analyze their benefits/drawbacks on CHF mitigation.

Bibliography

[1] Y. Guo, D. Groeneveld, and S. Cheng, "Prediction of CHF enhancement due to flow obstacles," *Int. J. heat mass …*, vol. 44, pp. 4557–4561, 2001.

[2] S. W. Peng, R. Revellin, D. C. Groeneveld, a. Z. Vasic, D. Shang, and S. C. Cheng, "Effects of flow obstacles on film boiling heat transfer," *Nucl. Eng. Des.*, vol. 222, no. 1, pp. 89–95, May 2003.

[3] S. Jayanti and K. Rajesh Reddy, "Effect of spacer grids on CHF in nuclear rod bundles," *Nucl. Eng. Des.*, vol. 261, pp. 66–75, Aug. 2013.

[4] J. Kim, P. Moin, and R. Moser, "Turbulence statistics in fully developed channel flow at low Reynolds number," *J. Fluid Mech.*, vol. 177, 1987.

[5] G. El Khoury and B. Pettersen, "Asymmetries in an obstructed turbulent channel flow," *Phys. Fluids (1994- …*, vol. 22, no. 9, p. 095103, 2010.

[6] S. Makino, K. Iwamoto, and H. Kawamura, "Turbulent structures and statistics in turbulent channel flow with two-dimensional slits," *Int. J. Heat Fluid Flow*, vol. 29, no. 3, pp. 602–611, Jun. 2008.

[7] E. a. Fadlun, R. Verzicco, P. Orlandi, and J. Mohd-Yusof, "Combined Immersed-Boundary Finite-Difference Methods for Three-Dimensional Complex Flow Simulations," *J. Comput. Phys.*, vol. 161, no. 1, pp. 35–60, Jun. 2000.

[8] F. Nygård and H. Andersson, "Numerical Simulation of Turbulent Pipe Flow Through an Abrupt Axisymmetric Constriction," *Flow, Turbul. Combust.*, vol. 91, no. 1, pp. 1–18, Feb. 2013.

[9] E. Roberts, "A numerical and experimental study of transition processes in an obstructed channel flow," *J. Fluid Mech.*, vol. 260, no. -1, p. 185, Apr. 1994.

[10] K. Nakatani, M.; Yao, M.; Suzuki, "flow visualization and heat transfer experiments in a turbulent channel flow obstructed with an inserted square rod.pdf," *Int. Jorbal Heat Fluid FFlow*, vol. 16, pp. 389–397, 1995.

[11] S. Chang, S. Moon, W. Baek, and Y. Choi, "Phenomenological investigations on the turbulent flow structures in a rod bundle array with mixing devices," *Nucl. Eng. Des.*, vol. 238, no. 3, pp. 600–609, Mar. 2008.

[12] K. H. Seok, S. Chang, and S. Chul-Hwa, "CFD ANANLYSIS OF THE MATIS-H EXPERIMENTS ON THE TURBULENT FLOW STRUCTURES IN A 5x5 ROD BUNDLE WITH MIXING DEVICES," *oecd-nea.org*, pp. 1–10, 2008.

[13] S.-K. Chang, S. Kim, and C.-H. Song, “Turbulent mixing in a rod bundle with vaned spacer grids: OECD/NEA–KAERI CFD benchmark exercise test,” *Nucl. Eng. Des.*, Jun. 2014.

[14] K. Podila, Y. F. Rao, M. Krause, and J. Bailey, “A CFD simulation of 5 × 5 rod bundles with split-type spacers,” *Prog. Nucl. Energy*, vol. 70, pp. 167–175, Jan. 2014.

[15] D. Caraghiaur, H. Anglart, and W. Frid, “Experimental investigation of turbulent flow through spacer grids in fuel rod bundles,” *Nucl. Eng. Des.*, vol. 239, no. 10, pp. 2013–2021, Oct. 2009.

[16] E. E. Dominguez-Ontiveros, Y. a. Hassan, M. E. Conner, and Z. Karoutas, “Experimental benchmark data for PWR rod bundle with spacer-grids,” *Nucl. Eng. Des.*, vol. 253, pp. 396–405, Dec. 2012.

[17] Y. Yeh and H. Z. Cummins, “LOCALIZED FLUID FLOW MEASUREMENTS WITH AN He-Ne LASER SPECTROMETER,” *Appl. Phys. Lett.*, vol. 4, no. 10, p. 176, 1964.

[18] B. Lehmann, “Geschwindigkeitsmessung mit Laser-Doppler-Anemometer Verfahren (LAMM),” *Teubner*, 1968.

[19] H. Vom Stein and H. Pfeifer, “A Doppler difference method for velocity measurements,” *Metrologia*, vol. 59, 1969.

[20] “University of Miskolc.” [Online]. Available: http://www.uni-miskolc.hu/~www_fiz/paripas/322.htm.

[21] TSI Inc., “Phase Doppler Particle Analyzer (PDPA)/ Laser Velocimeter (LDV),” no. November, 2005.

[22] J. M. J. den Toonder and F. T. M. Nieuwstadt, “Reynolds number effects in a turbulent pipe flow for low to moderate Re,” *Phys. Fluids*, vol. 9, no. 11, p. 3398, 1997.

[23] Y. A. Çengel, J. M. Cimbala, “Fluid Mechanics fundamentals and applications,” *Boston: McGraw-Hill*, 2006.

[24] J. J. Duderstadt, L. J. Hamilton, “Nuclear Reactor Analysis,” *Wiley & Sons*, 1942.

[25] E. Hecht, “Optics Fourth Edition,” *Addison Wesley*, fourth edition, 2002.

[26] J. R. Lamarsh, A. J. Baratta, “Introduction to Nuclear Engineering,” *Prentice Hall*, third edition, 2001.

[27] N. E. Todreas, M. S. Kazimi, “Nuclear Systems I - Thermal Hydraulic Fundamentals,” *CRC Press - Taylor & Francis Group*, 2012.

Appendix A: Corrections for LDV Measurements

When a pair of intersecting laser beams travel through different optical mediums with distinct indexes of refraction at a non-normal angle of incidence, they will be bent or refracted. As a result, the point of intersection and the angle between the beams will also change, this phenomenon has to be taken into account for location of the measuring volume. When the refraction occurs at a curved surface between different indexes of refraction, lensing effect is created. The test section used for this experimental work is squared on the outside, but circular inside, therefore it acts as a planar concave lens for the laser beams, where $R_1 = \infty$, $R_2 > 0$.

In 1621, Willebrord Snel van Royen, proposed an equation that predicts the refraction of wavefronts traveling through two different mediums with different indexes of refraction, known as Snell's Law:

$$n_i \sin\theta_i = n_t \sin\theta_t \tag{A.1}$$

Where θ_i is the angle of incidence and θ_t is the angle of transmission, measured from the normal to the interface between the two mediums. The wavelength of the wavefront in a medium of a given index of refraction n_i will also be changed as it travels through another medium with index of refraction n_t:

$$\lambda_i \, n_i = \lambda_t \, n_t \tag{A.2}$$

For the LDV system used in this experimental work, even if the medium for the measurements is not air, the change in the angle of intersection does not change the calibration factor or the fringe

spacing d_f, since the wavelength of the laser beams use$_d$ for measurement also depend on the refractive index of the medium.

A common solution for the problem of refraction through curved surfaces is to immerse the pipe in a tank with flat transparent walls, after which the tank is filled with a fluid that possesses an index of refraction equal to the walls of the pipe, which eliminates the refraction due to the curvature of the outer wall. Then by matching the index of refraction of the working fluid with the index of refraction of the pipe walls, the refraction due to the curvature of the inner wall is eliminated.

For this experimental study, the refraction due to the curvature of the outer wall of the pipe was eliminated by fabrication method of the test section. An 11.1125 mm in diameter channel was drilled in a squared cast acrylic piece; and the position of the measuring volume created by the four beams was determined analytically. Table 10 illustrates the indexes of refraction for the different mediums in this experiment.

Table 9 - Indexes of refraction for the experiments

Medium	**Symbol**	**Index of refraction**
Air	n_a	1.000
Fine polished cast acrylic	n_{acr}	1.491
water	n_{H2O}	1.333

Due to refraction of the laser beams at both the "near" and "far" pipe walls region, data acquisition was viable from 1.405 mm within the test section cross section, to about 9.706 mm, depending on the incremental steps across the test section, and the height along the pipe (probably due to small inconsistencies in the inner channel polishing). Beyond set values, the data rate was very slow and unreliable for some locations along the test section, since the cross position for both beam pars change at different rates within the test section. Therefore all measurements have the same apparent initial position, and their final position varied about ~ 0.6 mm. The 1.405 mm blind spot was inevitable due to the circular nature of the channel. Recall that these are apparent positions or locations, their value changed with the corrections implements.

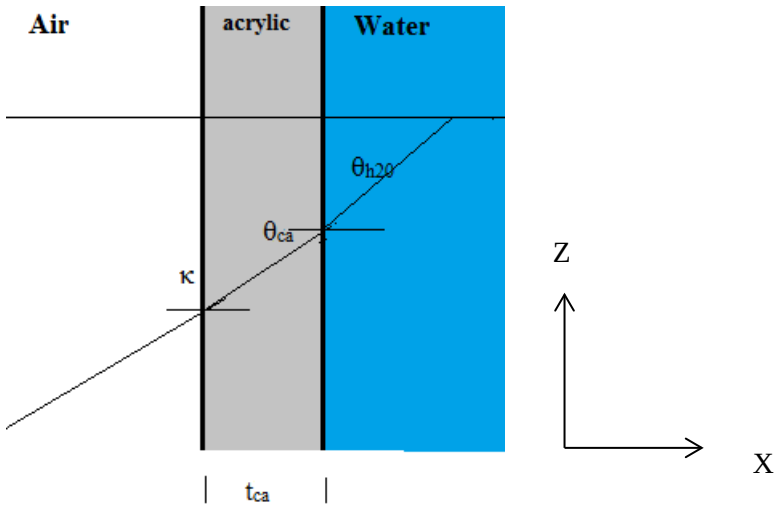

Figure A.1 - Path of laser beam in streamwise measurements

A.1 - Streamwise Measurements Correction

Figure A.1 shows the path of one perpendicular (green) laser beam through the test section, used to measure the streamwise velocity component. The angles of incidence are θ_{ca} through the cast

acrylic test section and θ_{h2o} through water. The actual displacements of both laser beams are calculated in the following steps:

1. The angle of incidence in the test section (θ_{ca}) is calculated using Snell's Law:

$$n_{air}\ \sin\kappa = \ n_{ca}\ \sin\theta_{ca} \tag{A.3}$$

2. The angle of incidence in water (θ_{H2O}) is calculated using Snell's law:

$$n_{ca}\ \sin\theta_{ca} = \ n_{H2O}\ \sin\theta_{H2O} \tag{A.4}$$

3. The displacement of the beams is calculated using the equation bellow (following Durst *et al.* 1981):

$$Displacement = \ -\mathrm{R}\left[\mathrm{X} + t_{ca}\left(1 - \frac{\cos\kappa}{\sqrt{(\frac{n_{ca}}{n_{air}})^2 - \sin^2\kappa}}\right)\right]\frac{1}{\cos\kappa}\sqrt{(\frac{n_{H2O}}{n_{air}})^2 - \sin^2\kappa} \tag{A.5}$$

Where, R is the radius (5.55625), X is the apparent position of the beams (in the y axis of the traverse system), and t_{ca} is the thickness of the test section.

With the corrections implemented, the apparent initial beam cross location or position of the green beams changed from 1.405 mm to 1.19 mm, yielding a 15% adjustment change for all streamwise positions or locations.

A.2 - Azimuthal Measurements correction

The test section acts as a planar concave lens for the laser beams, where $R_1 = \infty$, $R_2 > 0$. One could calculate the angles of incidence and use geometrical relations to calculate the

displacement, but instead the Thin-Lens equation, often referred to as Lensmaker's formula was used:

$$\frac{n_{ca}}{s_o} + \frac{n_{H2O}}{\mathrm{X}} = \frac{n_{H2O} - n_{ca}}{\mathrm{R}} \tag{A.6}$$

Where s_o is the desired displacement, X is the apparent position of the beams and R is the radius of the test section. After some manipulation the final equation becomes:

$$s_o = \frac{-n_{ca} * \mathrm{X} * \mathrm{R}}{n_{ca} * \mathrm{X} - n_{H2O}(\mathrm{X} - \mathrm{R})} \tag{A.7}$$

With the corrections implemented the apparent initial beam cross position or location for the blue beams changed from 1.405 mm to 1.525 mm, which yield an 8.6% adjustment change. However, the radial adjustment steadily decreased to nearly zero, as the beam approached the center of the test section, and steadily increased again as the beams moved further from the center of the channel or test section cross section center; unlike the adjustment change for streamwise measurements which remain a constant 15%.

Appendix B: Sources of Error and Experimental Uncertainty

Various factors can contribute to errors in experimental results, which can be divided into four groups: errors due to uncertainty in instrumentation components; errors in components alignment (includes laser alignment and traverse system precision); errors in test section; errors due to variations in LDV sampling.

The first group of errors is unavoidable, and impossible to improve upon, since each instrumentation component is manufactured and calibrated by independent manufactures; the only dependency on the user is the proper installation and operation for set instruments. In this study the flow meter (±0.25%), temperature indicator (±0.25%), and LDV (±2%) components have a specific measure uncertainty indicated by the manufacturer.

The second group of experimental errors was considered minimal for this study, because the placement of the traverse system on the laboratory remained unaltered, it's step motors operated with 2 decimal places of precision and the traverse arms level was checked daily to ensure precise alignment with the test section; the laser beam remained aligned and unaltered for all the runs, but the receiver head probe was changed between 152.5° and 154.3° to compensate for the curvature of the channel and optimized the sample rate.

Since the test section was manufactured manually in a machine shop, minor discrepancies on the dimensions are unavoidable; although the test sections were fine-polished to achieve an index of refraction n of 1.491 and roughness coefficient ε of 0.008, small cracks due to residual heat while drilling were observed (see Figure B.1). Thus to minimize these effects, the same test section was used for all runs in this study. These errors belong to the third group as well as the differences in

obtained data for repeated experiments with the same conditions (± 5% overall). Figures B.2, B.3 illustrate the difference in 3 sets of data obtain for the 3rd obstruction at Re = 99000 at 2 distances downstream of the obstruction on different dates.

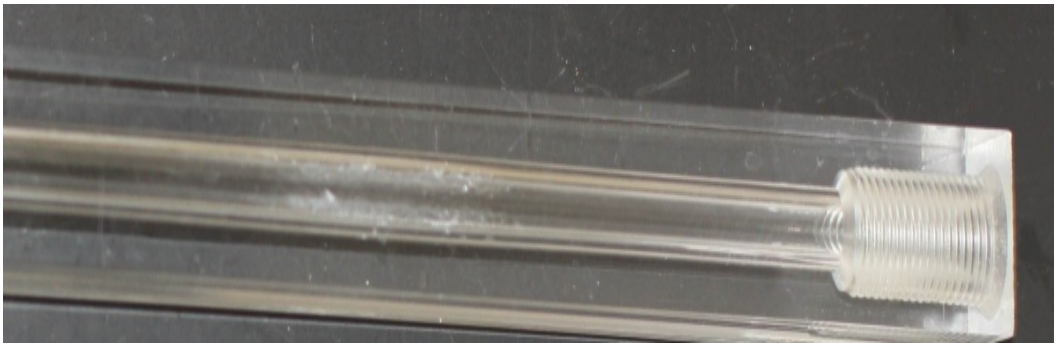

Figure B.1 - Test section with small cracks

The fourth group of errors is sampling errors due to the LDV system and its operation. The main error is due to the dependency on number of samples of instantaneous velocity measurements at each radial location used to calculate the mean streamwise and azimuthal velocity as well as the turbulence intensity. The variation in the results presented in this study is expressed in terms of the standard deviation σ which is given by:

$$\sigma = \sqrt{\frac{1}{N}\sum_{i=1}^{N}(x_i - \mu)^2} \qquad \text{(B.1)}$$

where N is the number of samples, the level of confidence is at least 92%.

The velocity statistics measured at any given point is affected by number of samples or measurements taken. In order to examine the dependence of the number of samples and velocity, measurements tests were performed in the middle of the test section at the same mass flow rate of

0.250 kg/s with 6000, 10000, and 15000 samples taken. The tests were repeated 5 times for each set of samples, Figure B.4 depicts the variation in the streamwise mean velocity with the number of samples

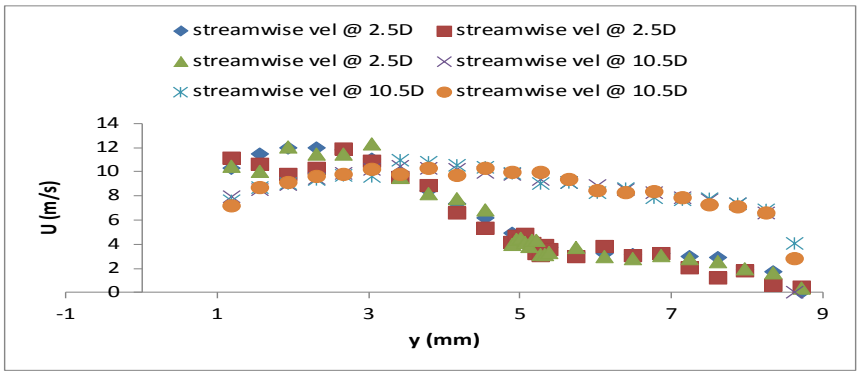

Figure B.2 - Streamwise velocity profiles 3rd obstruction different dates

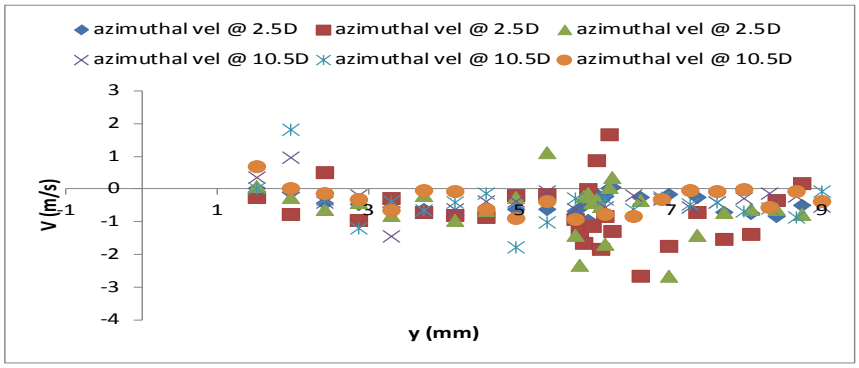

Figure B.3 - Azimuthal velocity profiles 3rd obstruction different dates

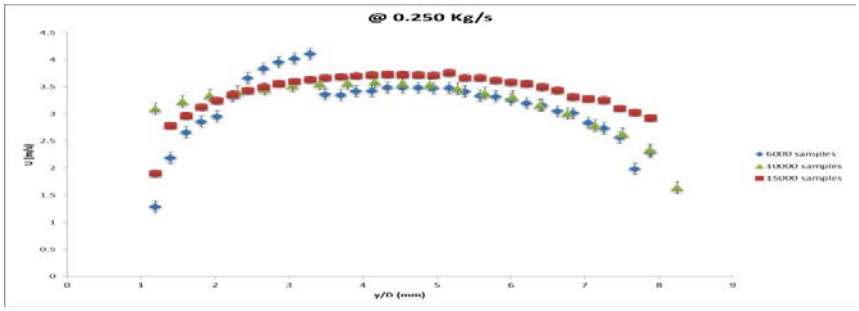

Figure B.4 - Streamwise mean velocity at different number of samples